The Interaction Between Multi-Dimensional Convection and Radial Stellar Pulsation

by

Chris M. Geroux

A Thesis Submitted to Saint Mary's University, Halifax, Nova Scotia in Partial Fulfillment of the Requirements for the Degree of

DOCTOR OF PHILOSOPHY

in

Astronomy

(Department of Physics and Astronomy)

February 7, 2013,Halifax, Nova Scotia

Approved: Dr. R.G. Deupree
Supervisor

Approved: Dr. Robert Stellingwerf
External Examiner

Approved: Dr. Ian Short
Examiner

Approved: Dr. Luigi Gallo
Examiner

Date: February 7, 2013

Contents

Contents ii

List of Figures v

List of Tables ix

Acknowledgements x

Abstract 1

1 Introduction 2

1.1 Observations of RR Lyrae Stars 4

1.2 The Radial Pulsation Mechanism 15

1.3 Modeling Radial Pulsations 17

2 Numerical Methods and Adiabatic Test Cases[1] 22

2.1 Introduction 22

2.2 Horizontal Eulerian Radial Lagrangian Scheme 28

2.2.1 Conservation Equations 29

2.2.2 Finite Volume Mass Conservation 31

2.2.3 Radial Grid Velocity 33

[1]This chapter originally appeared in Geroux, C. M. and Deupree, R. G. 2010, Astrophysical Journal, 731, 18

2.3 Computational Setup 34
2.3.1 Starting Model 34
2.3.2 The Grid and Numerical Details 35
2.3.3 Order of Calculation 37
2.3.4 Parallelism 38
2.4 Test Case Results 39
2.5 Conclusions and Next Steps 52

3 Non-Adiabatic Models 54
3.1 Radiation Diffusion 54
3.2 Changes To Starting Model Generation 56
3.3 Equation of State and Opacities 59
3.4 Implicit Solution 62
3.5 Subgrid Scale Turbulence Model 67

4 1D Models 72

5 2D Models 81
5.1 Interaction of Convection and Pulsation 83
5.2 Full amplitude Solutions 90
5.3 Model Structure with Convection Only 108

6 3D Models 110
6.1 Differences Between 2D and 3D Convective Flow Patterns 111

6.2 Comparison of 2D and 3D Convective Strength and Time Dependence 119

7 Conclusions 126

References 129

List of Figures

1.1 Instability strip in M 3 7

1.2 Pulsation amplitude across the instability strip in M 3 9

1.3 Pulsation amplitude across the instability strip in M 15 10

1.4 Pulsation period across the instability strip in M 3 11

1.5 Pulsation period across the instability strip in M 15 12

1.6 Light curve for v120 in M 3 13

1.7 Light curve for v6 in M 3 14

2.1 Geometry of a cell in spherical coordinates 32

2.2 Two-dimensional slice at constant ϕ (third ϕ zone) 44

2.3 Geometry of toroidal velocity perturbation 46

2.4 Two-dimensional slice at constant ϕ (sixth ϕ zone) 47

2.5 Two-dimensional slice at constant θ (sixth θ zone) 48

2.6 Radial grid velocity for three well separated periods 49

2.7 $\langle\rho\rangle$ for three well separated periods 50

3.1 King Ia and OPAL opacity comparison 61

3.2 Two dimensional conservation equation stencil 63

4.1 Peak kinetic energy and period for KING opacities, a mass of M=0.575$M_\odot$, and with the radial pulsation initiated at 2 km s^{-1}. 73

4.2 Peak kinetic energy and period for OPAL opacities, a mass of M=0.575$M_\odot$, and with the radial pulsation initiated at 2 km s^{-1}. 75

4.3 Peak kinetic energy and period for KING opacities, a mass of M=0.7$M_\odot$, and with the radial pulsation initiated at 2 km s^{-1}. 76

4.4 Peak kinetic energy and period for OPAL opacities, a mass of M=0.7$M_\odot$, and with the radial pulsation initiated at 2 km s^{-1}. 78

4.5 Peak kinetic energy and period for OPAL opacities, a mass of M=0.7$M_\odot$, and with the radial pulsation initiated at 10 km s^{-1}. 79

5.1 Convective time dependence of 6300 K effective temperature model. . 86

5.2 Convective time dependence of 6700 K effective temperature model. . 87

5.3 Maximum convective flux amplitude dependence. 88

5.4 Comparison of 1D and 2D peak kinetic energy curves 93

5.5 6300 K effective temperature model's light curve compared to variable star v120's light curve. 97

5.6 6300 K effective temperature model's light curve compared to variable star v19's light curve. 98

5.7 6400 K effective temperature model's light curve compared to variable star v48's light curve. 99

5.8 6500 K effective temperature model's light curve compared to variable star v93's light curve. 100

5.9 6600 K effective temperature model's light curve compared to variable star v10's light curve. 101

5.10 6700 K effective temperature model's light curve compared to variable star v92's light curve. 102

5.11 6900 K effective temperature model's light curve compared to variable star v125's light curve. 103

5.12 A_V's across the RR Lyrae instability strip 105

5.13 Logarithmic gradient of the horizontally averaged temperature with respect to the horizontally averaged pressure versus the horizontally temperature 109

6.1 Flow patterns of the 6300 K effective temperature 2D simulation. . . 112

6.2 Flow patterns of the 6300 K effective temperature 3D simulation. . . 113

6.3 Velocity vectors and temperature isosurface for 6300 K effective temperature model during compression. 114

6.4 Velocity vectors and temperature isosurface for 6300 K effective temperature model during expansion. 115

6.5 Velocity vectors and temperature isosurface for 6700 K effective temperature model during compression. 116

6.6 Velocity vectors and temperature isosurface for 6700 K effective temperature model during expansion. 117

6.7 Convective strength and time dependence for 6300 K effective temperature 2D and 3D models. 120

6.8 Convective strength and time dependence for 6700 K effective temperature 2D and 3D models. 121

6.9 The dependence of the maximum convective flux on pulsation amplitude. 122

6.10 Comparison of 3D and 2D light curves. 125

List of Tables

4.1 One-dimensional calculation set parameters. 74

5.1 One and two-dimensional peak kinetic energy growth rates. 89

5.2 Parameters of 2D models 91

5.3 Parameters of choice M 3 variables 95

6.1 Two and three-dimensional peak kinetic energy growth rates. 124

Acknowledgements

First and foremost I would like to thank my supervisor, Dr. Bob Deupree, without whom, this project would have never been possible. He has provided direction and encouragement above and beyond expectations. I would also like to thank my wife, Jenifer Parker, for emotional support and for keeping me fed throughout this process. Further thanks go to Jon Ramsey, Dave Williamson and James Wurster for discussions about hydrodynamics and debugging techniques. I would also like to thank Michael Gruberbauer for help with comparison of modeled and observed light curves. I appreciate the rest of the graduate students with whom I have spent the last few years for helping to create a good graduate student community. I would like to thank the ACEnet support staff, specifically Dr. Sergiy Khan who enthusiastically helped with debugging some environment specific problems with my code. Thanks also to Dave Lane who has maintained hardware and 3rd party software on department clusters and to ICA Assistant Florence Woolaver who has handled expenses and organizing appointments. Finally I would like to thank my parents for their support and encouragement with my schooling through the many years.

A large part of this work was performed by the ACEnet computational resources. ACEnet, a part of the Compute Canada, provides academic high-performance computing to Atlantic Canada. I am grateful for financial support from an NSERC Discovery Grant to R.G.D. and an ACEnet fellowship.

Abstract

The Interaction Between Multi-Dimensional Convection and Radial Stellar Pulsation

by Chris M. Geroux

We have developed a three-dimensional radiation hydrodynamics code to simulate the interaction of convection and pulsation in classical variable stars. One key goal is the ability to carry these simulations to full amplitude for comparison with observed light and velocity curves. The only previous multi-dimensional calculations were prevented from reaching full amplitude because of drift in the radial coordinate system, due to the algorithm defining radial movement of the coordinate system during the pulsation cycle. We remove this difficulty by defining our radial coordinate flow algorithm to require that the mass in a spherical shell remains constant for every time-step throughout the pulsation cycle. We present results from various tests and checks of our new numerical code SPHERLS such as comparison of our models pulsation periods with those of a linear adiabatic code and comparison to the analytic solution of a spherical blast wave. We have used our new code to perform 2D and 3D simulations of the interaction of radial pulsation and convection. We have made comparisons between light curves from our 2D convective simulations with observed light curves finding that our 2D simulated light curves are better able to match the observed light curve shape near the red edge of the RR Lyrae instability strip than light curves from previous 1D time dependent convective models. We examine the differences between the 2D and 3D convective flow patterns, finding stronger convective flows in 3D than 2D, but with only a small decrease in the 3D peak radial pulsation kinetic energy growth rates as compared to the 2D growth rates. Finally we make an early comparison between the 2D and 3D light curves near full amplitude.

February 7, 2013

1 Introduction

Variable stars have long played an important role in astronomy. This work focuses on a particular variable class named after the prototype RR Lyrae. This prototype variable star was discovered by W. P. Fleming and the findings were published by Pickering (1901) along with 63 other newly discovered variable stars.

The period of variability of RR Lyrae stars can be used to place constraints on their luminosity. RR Lyrae variable stars specifically played an important role in measuring the scale of our galaxy by determining distances to globular clusters. They provide an independent test of the classical Cepheid distance scales for nearby galaxies (e.g. Magellanic Clouds and M 31, Pritchet & van den Bergh (1987); Storm (2006)), and are also used to calibrate secondary distance indicators such as globular cluster luminosity functions (Di Criscienzo et al., 2006). Combining the location of the main-sequence turnoff in the HR diagrams of globular clusters with evolutionary models provides estimates of ages of globular clusters and puts constraints on stellar ages. The age estimates of globular clusters are impacted by accurate distances, determined by RR Lyrae stars. Globular cluster ages, which are some of the oldest objects in the sky, place constraints on cosmological models.

Thus, understanding variable stars, and in particular RR Lyrae variables, is important for many aspects of astronomy and for constraining some internal characteristics of stars such as the role of convection. Our understanding of variable stars has come

a long way since the beginning of the 20th century. Originally the variability of these stars was thought to be produced when the stars orbited an unseen companion, but work by Shapley (1914, 1916) demonstrated that the properties of the star's variability is much more easily explained with radial pulsation. Shapley explained that, given the size and period of variables, the companion would be well inside the visible star. He also noted that the rate at which the rise to maximum light occurs is inconsistent with that required for a reasonably uniform orbital period. Shapley notes that the periods of radial pulsation should be dependent on the mean density of the stars, and worked out the mean densities of various variable stars given their periods and compared them to other estimates of densities of various types of variable stars and found reasonable agreement. Shapley (1916) also found a 40 day variation of the period of RR Lyrae of $\pm$37 minutes. This was later known as the Blazhko Effect and is observed in other RR Lyrae variables as well. The origin of this effect is still debated today, though recent work suggests it may be related resonances between different modes (see Szabó et al. (2010);Buchler & Kolláth (2011)).

To truly understand variable stars our theories must be compared with observations. To accomplish this, computers are used to combine many aspects of physics into realistic models which can make predictions that are then compared with observations. Much work, nearly all one-dimensional, has been done in this manner with variable stars and considerable progress has been made. In section 1.2 we will outline the basic mechanism responsible for radial pulsation and in section 1.3 mention some

of the successes and describe some of the procedures for modeling radial pulsation. However, there are some issues remaining. In particular the current 1D models for the interaction between time dependent convection and radial pulsation have difficulties reproducing observed properties for cool RR Lyrae variable stars. This failure and others of the present 1D convective models will be discussed in more detail in section 2.1. The current work attempts to explore the interaction of convection and radial pulsation by directly simulating the convection in a manner similar to that used to hydrodynamically study solar convection (e.g. Stein & Nordlund, 1998; Nordlund et al., 2009). In the next section we will introduce some observed phenomena of RR Lyrae to which we can compare our models.

1.1 Observations of RR Lyrae Stars

Since it was discovered that RR Lyrae variables could be used as distance indicators they have been studied and observed extensively. Variable stars generally occupy a location known as the instability strip, a region in temperature and luminosity space in which stars are unstable to radial pulsation. RR Lyrae have been used as standard candles, as they have relatively constant absolute magnitudes, and thus luminosities, across the instability strip; however, there is some range in the luminosities. Sandage (1990) studied RR Lyrae stars in a number of globular clusters and finds that there are spreads in visual magnitude for a given temperature of between 0.2 and 0.6 mag (which corresponds to a spread in luminosity of 10 to $30L_{\odot}$ at a

typical luminosity for an RR Lyrae variable) with larger spreads occurring in clusters with higher metallicity. Sandage attributes the larger spreads to a combination of two effects, the metallicity dependence of the ZAHB (zero age horizontal branch) and evolution away from the ZAHB. He also mentions that this spread will complicate distance determinations especially when RR Lyrae variables are found near the limit of detection as incompleteness would affect the inferred $\langle M_V(RR)\rangle$. Typical values for the luminosity of RR Lyrae stars are from 40 to $70L_\odot$ (e.g. Cacciari et al., 2005, for the RR Lyrae variables in M 3). Cacciari et al. find an average mass for these stars of $0.71\pm 0.03\mathrm{M}_\odot$, based on determining masses from double mode pulsators on the order of $0.74M_\odot$, while determining masses from evolution of about $0.68M_\odot$. On the other hand masses as low as $0.36\mathrm{M}_\odot$ are theorized by Bono et al. (1997a) for solar metallicity field RR Lyrae stars.

There are uncertainties in measuring magnitudes and colors in RR Lyrae, as for all stars, from instrumental limitations, reddening, and atmospheric effects, for example. For variable stars in particular there are additional uncertainties with conversion of colors to effective temperatures of the equivalent static star. Observationally measured color indices are transformed using color-effective temperature relations, which are provided by grids of static atmosphere models. Thus, how the color-effective temperature relations for pulsating stars relate to those of static models is an issue. The RR Lyrae variables are pulsating and their colors change through out the cycle; at which phase should the color be measured or using what sort of average? The usual

procedure is to compute a mean color index. This can be done by either computing the averages with the magnitudes themselves, the intensities, or the differences between magnitudes or intensities. Carney et al. (1992) argue that no matter how the average is done, B-V colors are poor temperature indicators because they are distorted by surface gravity and line blanketing effects during non-negligible fractions of the pulsation cycle around maximum light, producing excess emission in the B band. Sandage (1990) and Bono et al. (1995) have both explored different methods for obtaining mean colors to represent those of the static star. While Sandage approached this empirically, and Bono et al. theoretically, both find similar methods to be best. Intensity averages of B and V separately plus some sort of amplitude-related correction reproduce the equivalent static colors reasonably well. We will be comparing mostly with observations by Cacciari et al. (2005) of M 3 RR Lyrae variables, who use the method developed by Bono et al. (1995).

Knowing the observational location of the RR Lyrae instability strip is important for validation of theoretical models. RR Lyrae stars generally pulsate in either the fundamental (RRab) or first overtone modes (RRc). RRab RR Lyrae have a sawtooth shaped light curve and typical periods between about 0.77-0.45 days, while RRc Lyrae have a more sinusoidal light curve shape with typical periods between about 0.5-0.25 days. The mode of pulsation is associated with the star's location within the instability strip, the region in the HR diagram where stars are unstable to radial pulsation. Thus moving from the cool edge to the hot edge of the instability

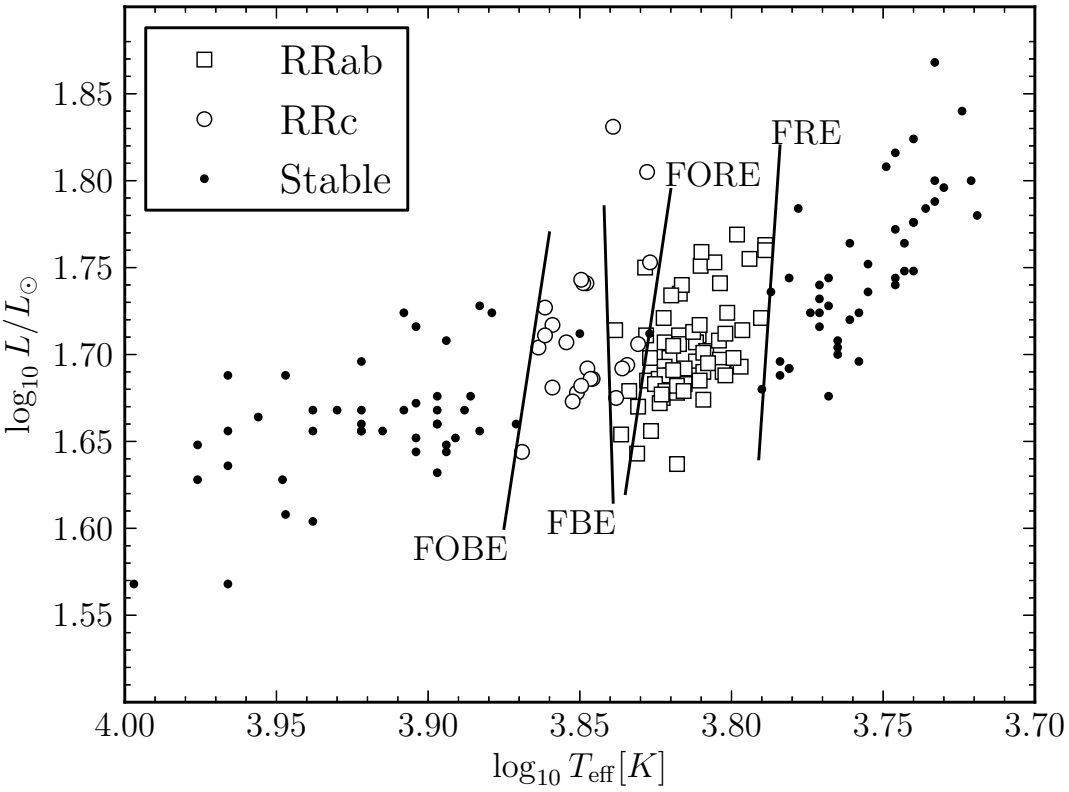

Figure 1.1: The instability strip in M 3, data for RRab variables (pulsate in the radial fundamental mode) and RRc variables (pulsate in the radial first overtone) are from Cacciari et al. (2005), data for stable stars are from Sandage (1990). To compute $\log_{10} L$ from Sandage's data a distance modulus of 15.1 was used. The temperatures from Sandage were shifted by -0.016 in the log to have them better match the data from Cacciari et al.. I have labeled the locations of the fundamental red edge (FRE), first overtone red edge (FORE), fundamental blue edge (FBE), and first overtone blue edge (FOBE) as indicated by the data.

strip we first have the fundamental red edge (FRE), followed by the first overtone red edge (FORE), the fundamental blue edge (FBE), and then finally the first overtone blue edge (FOBE). Figure 1.1 shows the location of the instability strip for the RR Lyrae variables in globular cluster M 3. This figure contains observational data from Sandage (1990) for non pulsating horizontal branch stars, data from Cacciari

et al. (2005) for RRab and RRc stars. The edge locations in this figure were chosen to most clearly separate the different modes of pulsation and stability of the observational data, keeping in mind an expected overlap of the fundamental and first overtone pulsators in an "or" region between the two modes. The edges dipicted in figure 1.1 are based on the observed data and are for illustrative purposes and do not represent theoretical models. Sandage (1990) studied the globular clusters M 3 and M 15, deriving effective temperatures from observed colors for a number of RR Lyrae variables in the fundamental and first overtone modes and for non-variable stars in the horizontal branch. From Sandage's data we deduce the locations of the edges, finding that for M 3 the FRE, FORE, FBE, FOBE have temperatures of 6170 K, 6900 K, 6900 K, 7590 K respectively. For M 15 the temperatures of the edges are 6310 K, 6750 K, 7000 K, and 7500 K respectively. Since the edge effective temperatures can depend on luminosity, these indicative effective temperatures were chosen near the center of the distribution in luminosity of the variable stars at each of the edges. Estimates of the uncertainty in these temperatures are from 90 to 110 K with the larger uncertainty for the higher temperatures. These uncertainty estimates are based on Sandage stating that errors in observed $B-V$ translate into a standard deviation in $\log(T_e)$ of 0.006. These uncertainties could be larger if including those of the color-temperature relation. Bingham et al. (1984) also determined effective temperatures for RR Lyrae variables in M 15 from which one finds similar effective temperatures for the edges of the instability strip. More recently Cacciari et al. (2005) have deter-

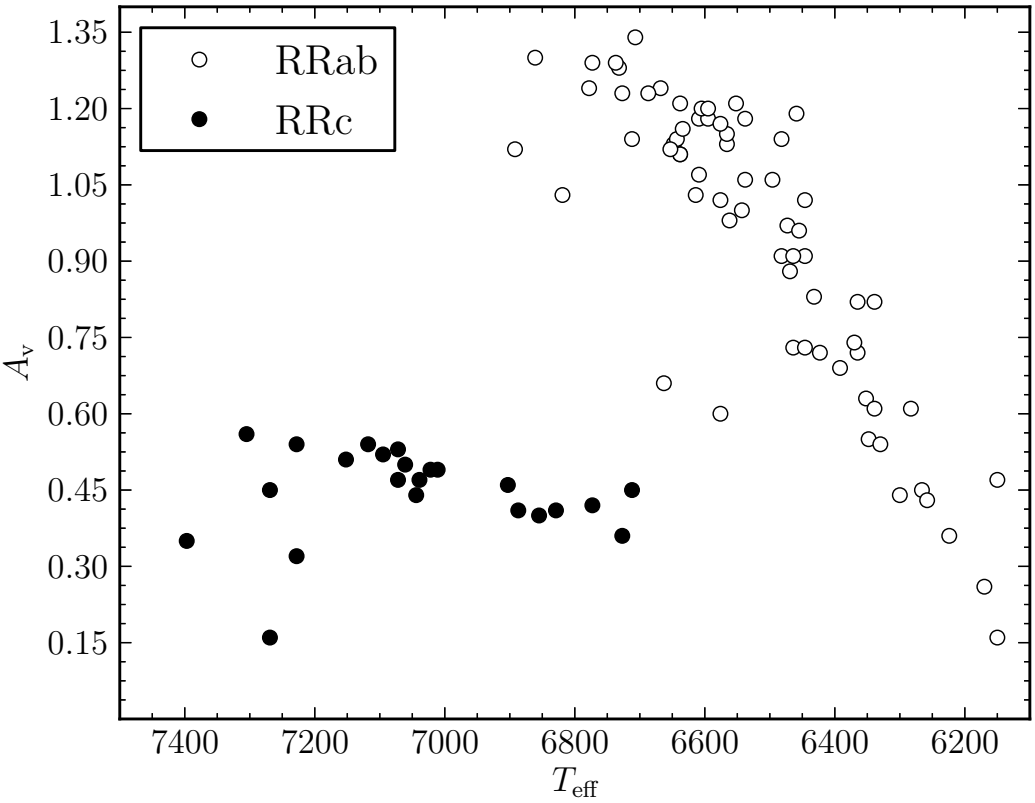

Figure 1.2: Visual pulsation amplitude across the instability strip in M 3, data from Cacciari et al. (2005)

mined effective temperatures for RR Lyrae variables in M 3 from which we find very similar effective temperatures for the instability strip as those from Sandage's data, of 6150 K, 6900 K, 6700 K, and 7400 K respectively for the edges with estimates for the uncertainty in temperature of individual stars of about 100 K. One difference of note between Sandage and Cacciari et al. is that the variables from Cacciari et al. form a region with a width of about 200 K where the first overtone and fundamental modes overlap while Sandage's data does not clearly indicate the presence of such a region.

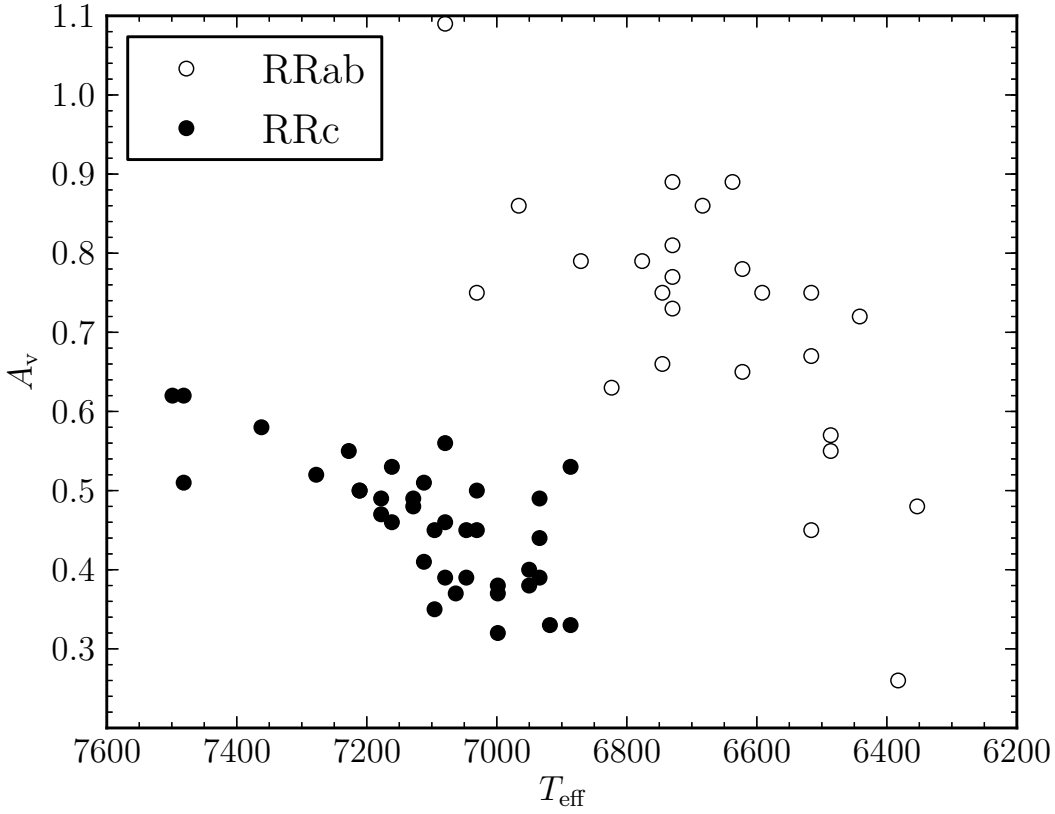

Figure 1.3: Visual pulsation amplitude across the instability strip in M 15, data from Bingham et al. (1984)

Another important observation for validation of theoretical models is that the amplitude of RR Lyrae variables varies across the instability strip. For fundamental mode pulsators cooler stars have lower radial pulsation amplitudes, and hotter stars have higher amplitudes. The visual amplitude variation dependence on effective temperature is shown for two clusters M 3, figure 1.2 and M 15, figure 1.3. The data for these figures are from Cacciari et al. (2005) and Bingham et al. (1984), respectively. The figures show fundamental mode pulsators (RRab) as open circles and first overtone pulsators (RRc) as filled circles. From these figures one can also note the edges

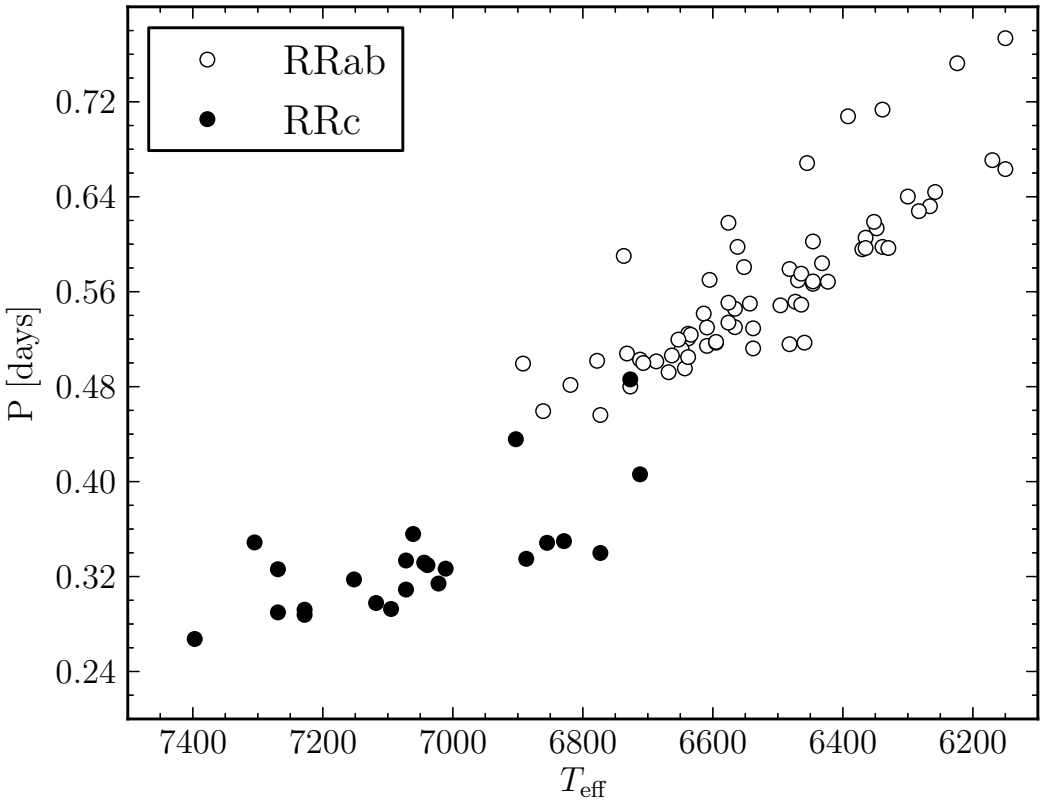

Figure 1.4: Pulsation period across the instability strip in M 3, an Oosterhoff type I cluster, data from Cacciari et al. (2005)

of the instability strip in effective temperature as well as the over lap region between the first overtone pulsators and the fundamental pulsators.

The two globular clusters M 3 and M 15 are members of two possibly distinct groups, the Oosterhoff type I and II clusters respectively. Oosterhoff (1939) studied globular clusters ω Cen, M 15, M 53, M 5, and M 3 and found that there were two distinct groups of clusters. M 5 and M 3 had RRab stars with mean periods of about 0.55 days (Oosterhoff type I), while the other 3 clusters had mean periods of about 0.65 days for their RRab stars (Oosterhoff type II). One can clearly see the differences

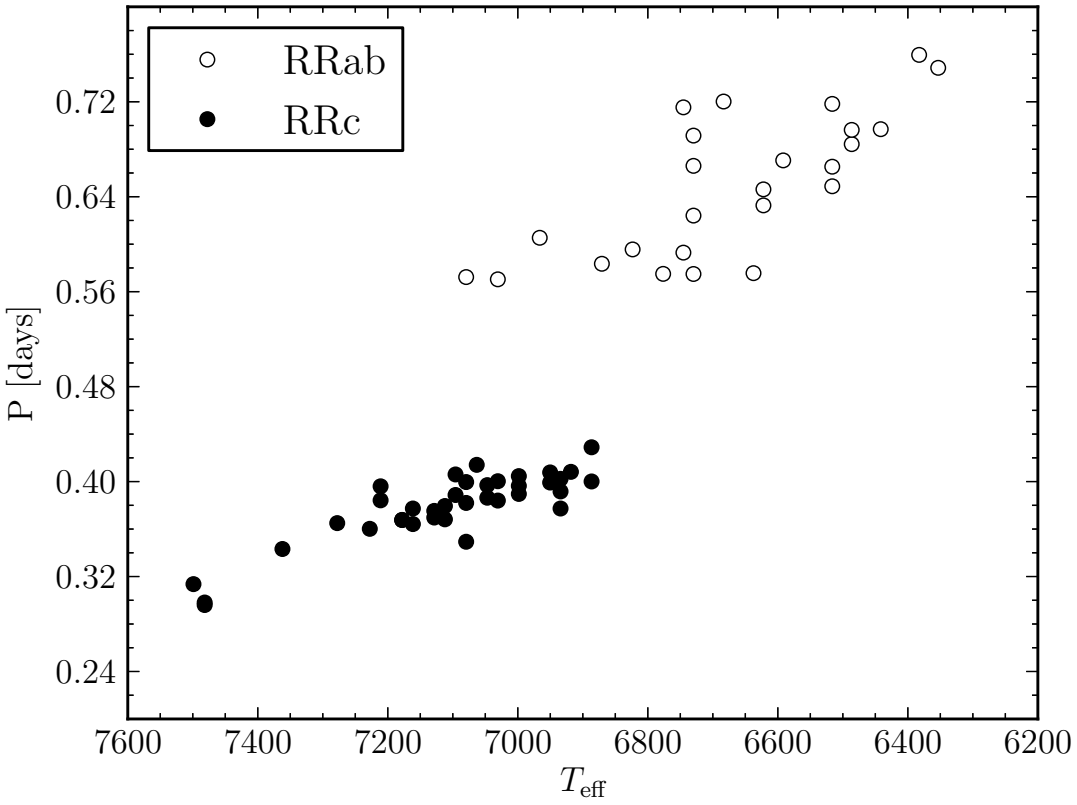

Figure 1.5: Pulsation period across the instability strip in M 15, an Oosterhoff type II cluster, data from Bingham et al. (1984)

between M 3 an Oosterhoff type I cluster and M 15 an Oosterhoff type II cluster from figures 1.4 and 1.5 which show the period as a function of effective temperature. The average of the periods of RRab stars in figure 1.4 for M 3 is much shorter than for the RRab stars in figure 1.5 for M 15. Sandage (1982) studied 30 globular clusters and found that the period shifts found by Oosterhoff form a continuum rather than fit into two nearly distinct period bins. He also found a correlation between the metallicity of the globular clusters and the period shifts with longer periods occurring in clusters with lower metal abundance. However, the differences between mean periods of RRab

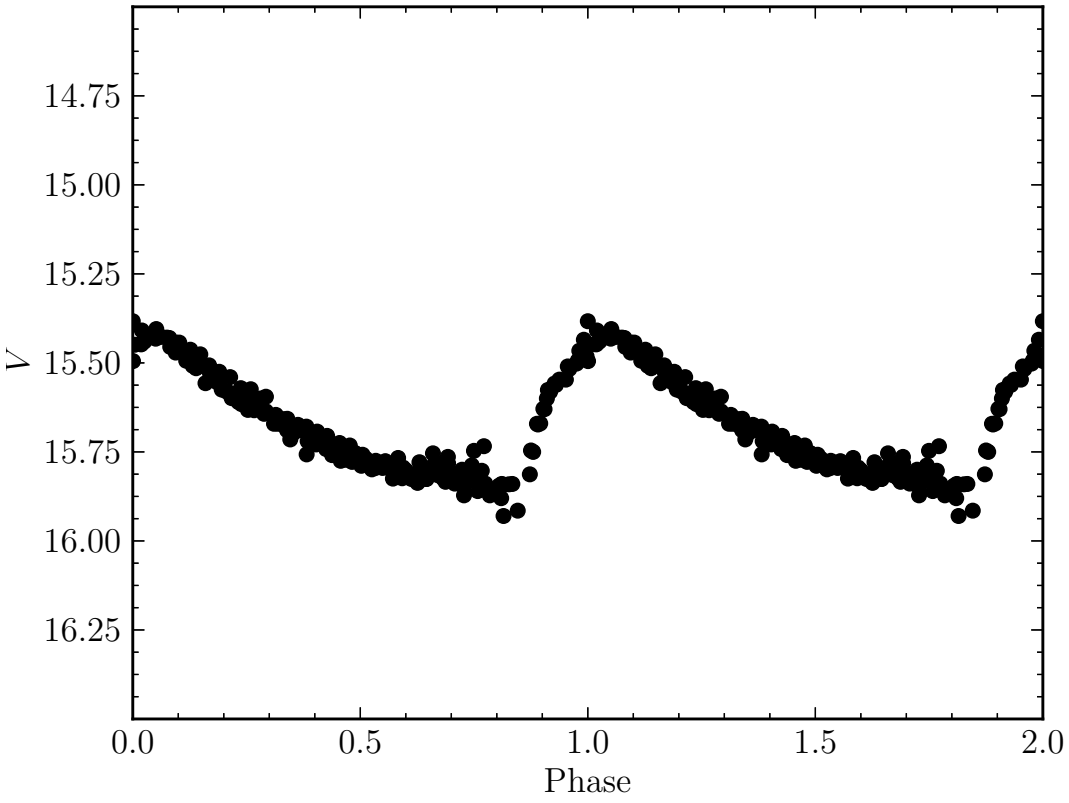

Figure 1.6: Light curve for v120, an RRab variable in M 3. Data from Corwin & Carney (2001)

variables of different globular clusters may be more complicated. Lee & Carney (1999) compared the Oosterhoff type II cluster M 2, and the Oosterhoff type I cluster M 3 noting that they have similar metallicities of [Fe/H]=-1.62 and [Fe/H]=-1.66 respectively, and found that they have very different horizontal branch morphologies indicating that the period differences are due to evolution away from the horizontal branch. They also find that M 2 is about 2 Gyr older than M 3 supporting this suggestion. The origin of the Oosterhoff period shifts is still debated.

Other useful observational data are the observed light curves. Two light curves

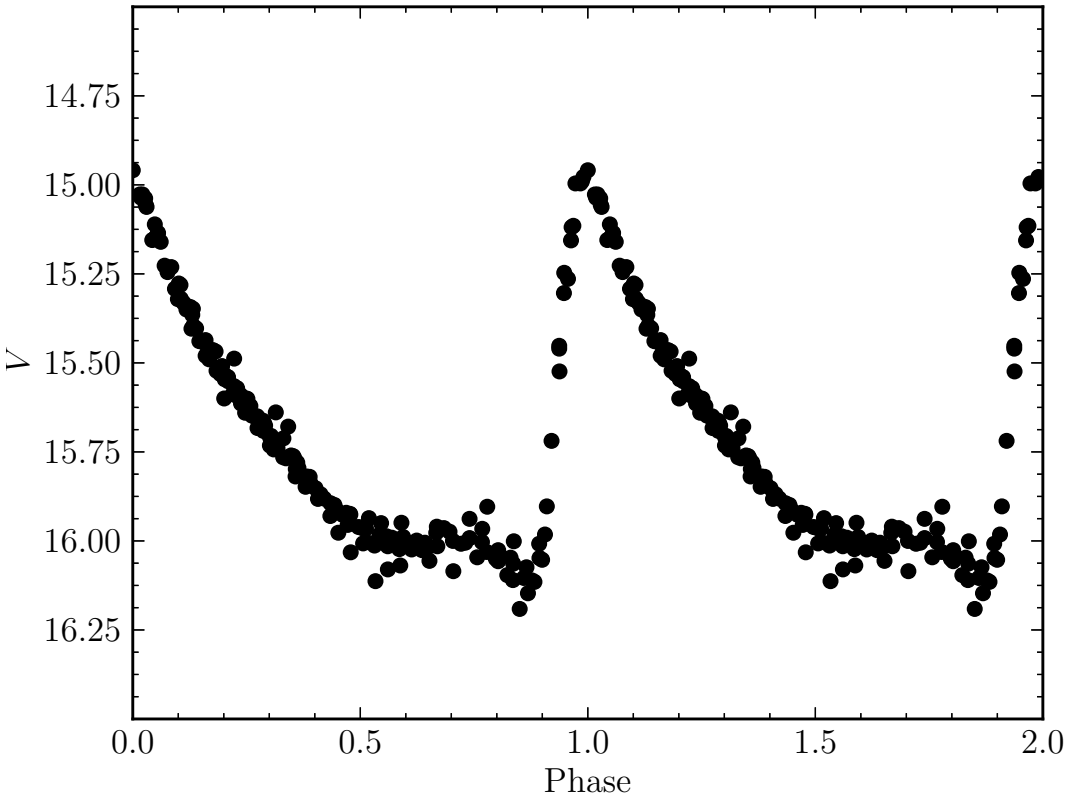

Figure 1.7: Light curve for v6, an RRab variable in M 3. Data from Corwin & Carney (2001)

for variable stars in M 3 are shown in figures 1.6 and 1.7 for fundamental pulsators. The data for these curves is from Corwin & Carney (2001). Work by Marconi & Degl'Innocenti (2007) indicates that these two curves correspond to a cool RR Lyrae (v120 in figure 1.6) close to the red edge of the instability strip and to a reasonably hot RR Lyrae closer to the blue edge of the fundamental instability strip (v6 in figure 1.7). We will compare our models to the light curves observed by Corwin & Carney

Convection plays a larger role near the red edge of the instability strip than at the hotter blue edge as was suggested by Christy (1964). It is believed to lead to

pulsational stability at the red edge for hotter effective temperatures than would be predicted from full radiative models which do not include any convection. In section 2.1 we discuss past work toward understanding the role of convection near the red edge. Comparison of our models with the cooler RR Lyrae light curve near the red edge of the instability strip will, therefore help to verify our approach to modeling time dependent convection. In the next section we will describe what causes stars to pulsate radially, followed by a discussion of how radially pulsating stars have been modeled in the past.

1.2 The Radial Pulsation Mechanism

A static star's structure is determined by a balance between the pressure (gas and radiation) and gravity. If this structure is perturbed from equilibrium it will normally oscillate about the equilibrium configuration until the pulsation is damped out by non-adiabatic losses. In order for radial pulsation to be maintained there must be a driving mechanism. The need for this driving mechanism was first noted by Eddington (1917). One of the driving mechanisms Eddington suggested was the sensitivity of nuclear reaction rates to temperature. As the central region of the star was compressed the temperature would increase and so too would the reaction rates, producing more energy to drive the pulsation. Eddington (1941a,b) later suggested another driving mechanism, the hydrogen ionization region. It was shown by Cox (1955) that the nuclear driving mechanism was not strong enough to over come the

damping in the rest star and thus was not effective at driving pulsation. Any pulsation would be damped out in a matter of days. Zhevakin (1953, 1954a,b) proposed that the helium ionization zone could also drive the pulsation. Independently Cox & Whitney (1958) also suggested that the second helium ionization zone is an important driving mechanism. Then Baker & Kippenhahn (1962) used linear non-adiabatic calculations (which will be described in section 1.3) and showed that the ionization regions were sufficient to drive pulsation.

To understand how the ionization zones drive the pulsation consider Kramers' opacity law, $\bar{\kappa} \propto \rho T^{-3.5}$. In normal regions of a star, as it contracts during pulsation both the density, ρ, and the temperature, T, increase and since the temperature dominates in Kramers' law the opacity, κ, goes down. During expansion the opposite happens and the opacity increases. However, in the partial ionization regions instead of the work done by compression raising the temperature of the gas, it instead is used to ionize the gas and the temperature remains relatively constant. In this case the opacity is dictated by the density, and the opacity will increase as the star contracts, and decrease when the star expands. The physical reason for the increase in opacity as the star contracts is due to more energy levels of the gas being populated in the cooler part of the ionization region. In these ionization regions, the increase in opacity during contraction will dam up energy, and the decrease in opacity during expansion will release it. This provides the mechanism required to drive radial pulsation in variables stars by producing a phase lag between the radial pulsation and the time

when energy is released, with the net result that the star gets a "push" outward when expanding and less resistance when contracting. In opposition to these driving regions are regions which damp the pulsation, and it is the imbalance between these two regions which will either cause a pulsation to grow (stronger driving than damping) or decay (stronger damping than driving). In the case of pulsation growth, as the amplitude of pulsation increases the ratio of driving to damping will decrease until they are equal resulting in full amplitude pulsation or limit cycle, the state in which most variable stars are observed.

1.3 Modeling Radial Pulsations

The first approach to numerical modeling of variable stars is to describe radial pulsation as perturbations of an otherwise static stellar model. One does this by assuming a periodic form for the variation of quantities with time in the conservation equations, and expanding the equations keeping only the first order linear terms. This allows one to solve the resulting eigenvalue problem for the perturbations of all variables in a 1D static model. These solutions provide the period, and in the non-adiabatic case also the growth rate. The resulting eigenfunctions provide information on the variations of quantities with depth in the model relative to surface values. A particularly good early code developed by Castor (1971) employed this method. The advantages of this method are primarily those of computational speed. Castor compared his results to that of Christy (1966b) and found good agreement between

computed periods. Castor also compared his linear growth rates to the non-linear growth rates of Christy and found reasonable agreement, with growth rates slightly larger by 0.8% for the fundamental and 1.7% for the first overtone.

Christy (1964) was the first to lay out the equations governing radial stellar pulsation in a way to be used to numerically compute the time dependent non-linear radial pulsations of a star from an initial state to large amplitude. He formulated the problem in a Lagrangian frame, with the mass (M_r) interior to the radius (r) from the center of the star as the independent variable. If considering the forces acting on a small shell of mass one can write down an equation relating the acceleration of the mass shell to the force of gravity and the force resulting from the gas pressure, P, as

$$\frac{\partial^2 r}{\partial t^2} = -\frac{GM_r}{r^2} - 4\pi r^2 \frac{\partial P}{\partial M_r}. \tag{1.1}$$

Equation 1.1 is simply Newton's second law. The heat-flow equation can be written as

$$\frac{\partial E}{\partial t} + P\frac{\partial V}{\partial t} + \frac{dL_r}{dM_r} = 0 \tag{1.2}$$

where

$$L_r = -(4\pi r^2)^2 \frac{4\sigma}{3\kappa} \frac{d(T^4)}{dM_r}. \tag{1.3}$$

The term κ is the Rosseland mean opacity, $V = 1/\rho$ is the specific volume, σ is the Stefan-Boltzmann constant, t is the time, and E is the specific internal energy. Equation 1.2 dictates that the sum of the rate of work done by the gas, the rate

at which energy is deposited or removed by radiation, and the rate at which the specific internal energy changes is conserved. This formulation assumes that heat flow is entirely by radiation diffusion. To complete this description, equations of state relating both the pressure and internal energy to the temperature and density are required. In addition the opacity must also be specified in a similar way, which was provided to Christy from then unpublished calculatoins perfomed at Los Alamos Scientific Laboratory.

The procedure used by Christy (1964) was to calculate an initial static condition with an imposed radial velocity profile from a polynomial function that varies with the fractional radius. Starting from a non-zero radial velocity reduces the time for the mode to grow to full amplitude as opposed to allowing it to grow up from machine round off error. Starting from this initial model, equations 1.1 and 1.2 together with other supporting equations were written with the derivatives approximated by finite differences and then used to calculate a new state at time, $t = 0 + dt$ in the future and to proceed in this manner until the desired end time was reached, each time step using the state most recently calculated to calculate the next state. In order to do this some boundary conditions needed to be chosen. Christy approximates the inner $\approx$10% of the star as static, or more specifically that the velocity at the inner boundary of the computational region was set to zero. He also assumed that all the nuclear energy generation occurred within this 10% of the star and set the luminosity at the inner boundary to a constant, L_0. At the outer boundary the pressure was set to

zero, consistent with a free surface. Moreover he used the solution for the equation of transfer of a static gray atmosphere to relate the surface temperature to the effective temperature, namely that $T^4 = \frac{3}{4}T_{\rm eff}^4(\tau + \frac{3}{2})$. At the surface the optical depth, τ, is zero and $T_{\rm surf.} = 2^{-1/4}T_{\rm eff}$. The relation for $T_{\rm surf.}$ together with the Stefan-Boltzmann equation, $L = 4\pi R^2 \sigma T_{\rm eff}^4$ provides the final boundary condition at the surface.

With this prescription for modeling radial pulsation one can investigate many properties of variable stars such as the pulsation period, growth rates, pulsation stability or instability, and light and velocity curves of full amplitude solutions. Christy was able to match reasonably well the observed phase lag between the luminosity and radial velocity curves observed. Later Christy (1966a) conducted a more extensive exploration of RR Lyrae stars, and most notably was able to map out the RR Lyrae instability strip with reasonable success except near the cool boundary, and suggested that this was due to the omission of convection in his models, stating that this omission should not otherwise effect his conclusions of stability. In section 2.1 I will discuss how some have approached the difficult problem of including convection in radial pulsation calculations.

The current work uses a method similar to that used by Christy to model radial pulsation, but including the full three dimensional (3D) conservation equations to directly model the convective flow patterns. For this purpose we have developed a radiation hydrodynamics code named, SPHERLS (Stellar Pulsation with a Horizontal Eulerian, Radial Lagrangian Scheme). This code is capable of modeling 1D fully

radiative or 2D and 3D convective models of radial stellar pulsation. We have developed the code in a step by step process, one of the first steps was to determine a way to move the radial grid so that it followed the pulsation of the star and allowed us to use M_r as the radial independent variable as Christy did, while still allowing flow in an Eulerian way in the horizontal directions. We discuss this method in section 2.2. We then applied this new method to adiabatic test cases and describe these tests and their results in section 2.4. The next step was to add the non-adiabatic terms to the energy equation which we address in chapter 3. We explore parameter space quickly with one dimensional (1D) fully radiative models as a means to decide on initial models for higher dimension models which are much more computational intensive in chapter 4. With the initial models decided upon we then calculated 2D convective models. These models allowed us to explore the time dependence of convection on pulsation phase as well as the growth rates of radial pulsation. The results of which are presented in section 5.1. Once these 2D convective RR Lyrae models reached the full amplitude of their pulsation it was possible to compare the light curves from these models to observed light curves. We present this comparison in section 5.2. We have also begun 3D calculations which are far enough along that we may assess the differences between 2D and 3D convective flow patterns, the results of which are presented in chapter 6.

2 Numerical Methods and Adiabatic Test Cases

2.1 Introduction

Early nonlinear calculations of stellar pulsation, as outlined by Christy (1964), used a 1D Lagrangian framework and had considerable success producing full amplitude RR Lyrae models that resembled the basic observations. However, these calculations used purely radiative envelopes and failed to identify a red edge to the RR Lyrae instability strip. This lead to the hypothesis that convection in the ionization zones quenched pulsation (Baker & Kippenhahn, 1965; Christy, 1966a). To explore this, Tuggle & Iben (1973) used a 1D, linear, non-adiabatic code with a time-independent mixing length theory for the convective flux. They found that time-independent convection only reduced the growth rate of pulsation but did not produce pulsational stability.

Several formalisms and 1D codes were developed that included time-dependent convection by introducing an additional differential equation to calculate the evolution of the convective flux with time based on the standard mixing length theory (Cox et al., 1966a,b; Unno, 1967; Gough, 1977). Stellingwerf (1982a,b, 1984a,b,c) developed a time-dependent treatment of convection for 1D Lagrangian models which follows the time evolution of averaged convective velocities and includes a treatment

of overshooting and eddy viscosity to account for small length scale kinetic energy dissipation.

There are several numerical difficulties associated with modeling radial pulsation. First there are very steep gradients in the ionization zones and adequately resolving these gradients is important for accurate modeling. Gehmeyr (1992a,b, 1993) and Dorfi & Feuchtinger (1991) have both included adaptive grids to better resolve the steep gradients in the ionization zones as they sweep through the envelope during pulsation. Using a version of Stellingwerf's time-dependent convective model with his adaptive scheme, Gehmeyr was able to produce a red edge at roughly the observed effective temperature. He notes that the effective temperature of the red edge is dependent on the parameters used for the convective model, and that the predicted temperature of the red edge could vary by a few hundred degrees Kelvin depending on the values used for the convective model parameters. Also, there are differences between Gehmeyr's light amplitude-rise time relationship and the observed relationship in both slope and zero point. Feuchtinger & Dorfi (1996) used their adaptive code to calculate light and radial velocity curves which exhibit shapes typical of RR Lyrae stars. A second potential difficulty is an accurate representation of the surface boundary, which Feuchtinger & Dorfi tested by including a model atmosphere and found that its inclusion did not impact the pulsational characteristics of the model.

Marconi et al. (2003) used the 1D, Lagrangian, hydrodynamics code described by Bono & Stellingwerf (1994) and Bono et al. (1997a,b) to compute RR Lyrae models

to compare with the RR Lyrae stars observed in M 3. In order to fully specify the problem Marconi et al. needed to choose a mixing-length parameter, and adopted both $l/H_p = 1.5$ and 2.0, where l is the mixing-length and H_p is the pressure scale height. They found that in order to match the boundaries of the RR Lyrae gap in M 3, they required two different mixing-length parameters, one to obtain the observed blue edge location ($l/H_p \approx 1.5$) and the other to obtain the observed red edge location ($l/H_p \approx 2.0$). In addition the observed visual amplitude as a function of B-V displays nonlinear characteristics, while theoretical relations predict linear relationships. Marconi et al. also mention that a mixing-length parameter of 2.0 produces luminosities for horizontal-branch models that are brighter than is observed by $\approx 0.08 \pm 0.05$ mag.

Other models for time-dependent convection in one dimension have been proposed by Kuhfuss (1986) and Xiong (1989). Kuhfuss argued that the convective model by Stellingwerf (1982a) does not use the diffusion approximation consistently throughout the model. Smolec & Moskalik (2008) developed their application of the Kuhfuss convective model, which requires eight free parameters, and used it to study convection in β Cephei stars (Smolec & Moskalik, 2007). They found that convection is not important for calculating pulsation amplitudes for their models. However, they caution that their convective model, while working well for classical pulsators, is at the limits of its applicability in the β-Cephei models they are studying. More recently, Olivier & Wood (2005) have also developed a code including the Kuhfuss convective model

and present some test calculations of their program, mentioning that the turbulent viscosity parameter shows potential as an important determinant of the pulsation amplitudes.

The distillation of multi-dimensional convective phenomenon to one dimension is always accompanied by extra equations and/or parameters to approximate the effects of convective motions of material in more than one spatial dimension. Deupree (1977a) approached the interaction of convection and stellar pulsation in a fundamentally different way using a two-dimensional hydrodynamic code directly to follow the convective flow patterns. While Deupree (1977b,c, 1980, 1985) was able to successfully determine the observed edges of the RR Lyrae instability strip, he was unable to compute full amplitude solutions because his algorithm for moving the radial coordinate allowed the radial zoning to drift over time. Consequently at later times, the radial zoning did not cover the hydrogen ionization zone adequately and the calculations were eventually numerically unreliable. The algorithm Deupree used for the moving radial coordinate used the horizontal average of the radial velocities at a particular radius as the grid velocity. Recently Bruenn et al. (2010) have used a similar average radial velocity as the grid velocity to follow the core in-fall phase in supernovae simulations. Another form of a radial moving grid was by Mundprecht (2009), where the radial grid velocity at the surface was set as the average of the radial velocities, and the inner grid velocity was held constant. The intermediate radial grid velocities were then set using a dilatation factor.

Recently Stökl (2008) developed an approach for modeling pulsation somewhere between the 2D model of Deupree and the 1D convective models. Stökl used two radial columns to model convection. One column represented the sum of all upward convective flows, and the other column represented the sum of all downward flows. While not including any mixing length parameter, it does contain free parameters related to the physical size of the convective cells, and the fraction of the surface area of a spherical surface which contains downdrafts. These parameters do have a physical basis, but in practice it would be difficult to determine them as they are probably functions of depth and likely depend on a particular star's properties. Also, because the model only has two radial columns it may miss some of the more subtle features of convection. More recently others have begun working on directly simulating the interaction of convection and pulsation in 2D (Muthsam et al., 2011; Gastine & Dintrans, 2011).

Both Buchler (2009) and Marconi (2009) have stressed the importance of improving the convective models used in variable stars. Buchler highlights some of the well known difficulties facing time-dependent mixing length noting that it is an empirical description, rather than a consistent physical description. Also, the up to eight or more free parameters used in time-dependent mixing length approach can not be chosen based on physics, but instead must be calibrated by comparison with observations. Marconi mentions some remaining problems for RR Lyrae models, particularly the unsatisfactory match between theoretical light curve morphology and observed

light curve morphology near the red edge of the RR Lyrae instability strip, supporting the suggestion that an improved treatment of turbulent convection is needed.

3D convective simulations have had significant success in other areas of stellar astrophysics. For example Nordlund et al. (2009) note many of the recent successes in 3D modeling of solar surface convection, in particular that 3D models with numerical resolutions around 200^3 reproduce widths, shifts, and shapes of observed photospheric spectral lines with high accuracy. 3D convective simulations by Meakin & Arnett (2007) simulated core convection in a massive star finding differences in 2D and 3D convective velocities in both morphology and magnitude. 3D models remove the need for many free parameters and the lack of a physically consistent description of convection, with convection resulting naturally from the conservation laws; however, an algorithm to include the effects of sub-grid scale turbulence on the larger eddies is still required. Here we build on the ideas of Deupree (1977a), with the goal of developing a fully 3D calculation in which the radial coordinate moves in such a manner to allow us to perform full amplitude solutions of RR Lyrae models with Large Eddy Simulations (LES) of convective energy transport. As a first step we apply our approach to purely adiabatic models to verify that the method can compute accurate and stable large amplitude periodic solutions over many periods.

2.2 Horizontal Eulerian Radial Lagrangian Scheme

Calculation of full amplitude solutions requires following the pulsation for many periods. 1D codes have been able to calculate full amplitude solutions, while Deupree's 2D code had difficulty after many periods because of his particular moving radial coordinate. This led us to try using the internal mass, M_r, as the radial independent variable instead of radius, r, and allow r to change such that the mass within a shell remains constant. This requires introducing a grid velocity, v_{0r}, in the radial direction that dictates how the coordinate system radius changes. The intent is that our radial grid acts like that of a 1D Lagrangian code while allowing the usual Eulerian approach in the horizontal directions. Note that this approach still allows fluid flow across radial zone boundaries. It just moves the radial gridding so that it maintains the mass in a spherical shell. It does not put any constraints on the horizontal flow and does not alter the physics of the conservation equations in any way.

The calculations are performed in a limited range of the spherical polar coordinates θ and ϕ, a 3D version of a "pie slice". Periodic boundary conditions are placed in the horizontal directions. The interior boundary is placed at a location deeper than 0.15 of the stellar radius and is regarded as rigid. This is a common assumption in most 1D simulations. Because the horizontal zoning would get very narrow (leading, through the Courant condition, to undesirably short time steps) and because the 3D flow of

interest is expected to be only in the surface ionization regions, we impose a purely radial region for an arbitrary number of radial zones above the interior boundary. In conjunction with the assumption that non-radial motion occurs only near the very low mass surface, we assume the gravitational force has its spherically symmetric form.

2.2.1 Conservation Equations

We first define a horizontally averaged density which allows us to replace an infinitesimal radial change, dr, with an infinitesimal internal mass change, dM_r. The mass of a spherical shell of thickness dr is given by d$M_r = 4\pi r^2 \langle\rho\rangle$d$r$ where $\langle\rho\rangle$ is the volume averaged density within a spherical shell,

$$\langle\rho\rangle_i = \frac{1}{V_i}\sum_{j,k}\rho_{i,j,k}V_{i,j,k}. \tag{2.1}$$

Here i, j, and k are the $\hat{r}$, $\hat{\theta}$ and $\hat{\phi}$ zone indices defined at zone centers and increase with each of their respective spherical coordinates (e.g., i increases from the center of the star towards the surface). V_i is the volume of a spherical shell at a particular radial shell, i, that spans all the j and k at that i. $V_{i,j,k}$ is the volume of the (i,j,k) grid cell. In order to develop and test this approach, we have assumed that the system is adiabatic. Introducing both dM_r and the grid velocity, v_{0r}, into the 3D conservation

equations for mass, three components of momentum, and energy produces:

$$\begin{aligned}\frac{\partial \rho}{\partial t} &+ 4\pi r^2 \langle\rho\rangle \left(v_r - v_{0r}\right) \frac{\partial \rho}{\partial M_r} + \frac{v_\theta}{r}\frac{\partial \rho}{\partial \theta} + \frac{v_\phi}{r\sin\theta}\frac{\partial \rho}{\partial \phi} \\ &+ 4\pi\langle\rho\rangle\rho \frac{\partial\left(r^2 v_r\right)}{\partial M_r} + \frac{\rho}{r\sin\theta}\frac{\partial\left(v_\theta \sin\theta\right)}{\partial\theta} + \frac{\rho}{r\sin\theta}\frac{\partial v_\phi}{\partial\phi} = 0, \end{aligned} \tag{2.2}$$

$$\begin{aligned}\frac{\partial v_r}{\partial t} &+ 4\pi r^2 \langle\rho\rangle \left(v_r - v_{0r}\right) \frac{\partial v_r}{\partial M_r} + \frac{v_\theta}{r}\frac{\partial v_r}{\partial \theta} + \frac{v_\phi}{r\sin\theta}\frac{\partial v_r}{\partial \phi} \\ &= \frac{-4\pi r^2\langle\rho\rangle}{\rho}\frac{\partial P}{\partial M_r} + \frac{v_\theta^2}{r} + \frac{v_\phi^2}{r} - \frac{GM_r}{r^2}, \end{aligned} \tag{2.3}$$

$$\begin{aligned}\frac{\partial v_\theta}{\partial t} &+ 4\pi r^2 \langle\rho\rangle \left(v_r - v_{0r}\right) \frac{\partial v_\theta}{\partial M_r} + \frac{v_\theta}{r}\frac{\partial v_\theta}{\partial \theta} + \frac{v_\phi}{r\sin\theta}\frac{\partial v_\theta}{\partial \phi} \\ &= \frac{-1}{r\rho}\frac{\partial P}{\partial\theta} + \frac{v_\phi^2\cot\theta}{r} - \frac{v_r v_\theta}{r}, \end{aligned} \tag{2.4}$$

$$\begin{aligned}\frac{\partial v_\phi}{\partial t} &+ 4\pi r^2 \langle\rho\rangle \left(v_r - v_{0r}\right) \frac{\partial v_\phi}{\partial M_r} + \frac{v_\theta}{r}\frac{\partial v_\phi}{\partial \theta} + \frac{v_\phi}{r\sin\theta}\frac{\partial v_\phi}{\partial \phi} \\ &= \frac{-1}{\rho r\sin\theta}\frac{\partial P}{\partial\phi} - \frac{v_r v_\phi}{r} - \frac{v_\theta v_\phi\cot\theta}{r}, \end{aligned} \tag{2.5}$$

$$\begin{aligned}\frac{\partial E}{\partial t} &+ 4\pi r^2 \langle\rho\rangle \left(v_r - v_{0r}\right) \frac{\partial E}{\partial M_r} + \frac{v_\theta}{r}\frac{\partial E}{\partial \theta} + \frac{v_\phi}{r\sin\theta}\frac{\partial E}{\partial \phi} \\ &+ \frac{4\pi\langle\rho\rangle P}{\rho}\frac{\partial\left(r^2 v_r\right)}{\partial M_r} + \frac{P}{\rho r\sin\theta}\frac{\partial\left(v_\theta\sin\theta\right)}{\partial\theta} + \frac{P}{\rho r\sin\theta}\frac{\partial v_\phi}{\partial\phi} = 0. \end{aligned} \tag{2.6}$$

The above symbols have their usual meaning (E is the specific internal energy). Finally the system is closed with three further equations:

$$\frac{\partial r}{\partial t} = v_{0r}, \tag{2.7}$$

which is used to update the radius,

$$P = (\gamma - 1)\rho E, \tag{2.8}$$

a simple gamma-law gas for the equation of state, and an equation for solving for the grid velocity (see equation 2.15). Before we present the equation for the grid velocity, we present an equivalent equation to equation (2.2) by which we solve mass conservation.

2.2.2 Finite Volume Mass Conservation

The definition of volume we will use in the equation for determining the grid velocity (eq. (2.15)) and the average density (eq. (2.1)) must be consistent with the mass conservation equation. The definition of volume we use in equations (2.15) and (2.1) is

$$V_{i,j,k} = \int_{r_{i-1/2}}^{r_{i+1/2}} \int_{\theta_{j-1/2}}^{\theta_{j+1/2}} \int_{\phi_{i-1/2}}^{\phi_{j+1/2}} r^2 \sin\theta \, d\phi \, d\theta \, dr. \tag{2.9}$$

To make the mass equation consistent with this definition of the volume, one integrates equation (2.2) over the volume, then uses Gauss's theorem to convert the

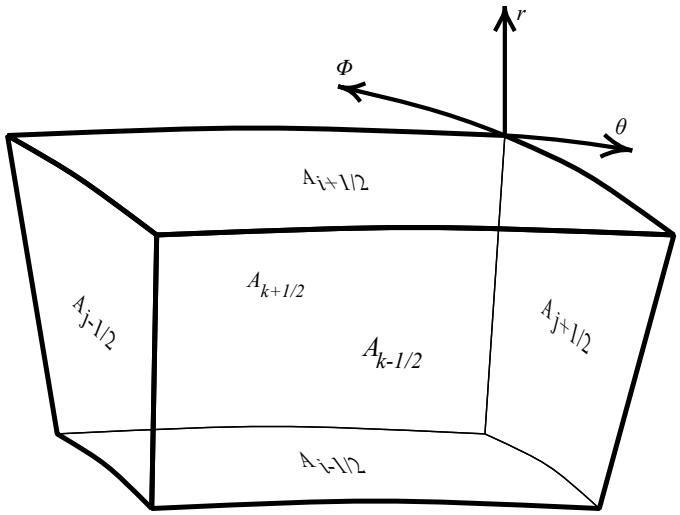

Figure 2.1: Geometry of a cell in spherical coordinates. The areas of the six surfaces of the "cube" are shown.

volume integral into a surface integral, producing the finite volume form of the mass conservation equation.

The mass in a cell changes only from mass flowing into and out of that cell. This change from one time step (n) to the next $(n+1)$ can be written as

$$V_{i,j,k}^{n+1}\rho_{i,j,k}^{n+1} - V_{i,j,k}^{n}\rho_{i,j,k}^{n} = \Delta t^{n+1/2}\cdot\left[\left(F_{i-1/2}^{n+1/2}A_{i-1/2}^{n+1/2} - F_{i+1/2}^{n+1/2}A_{i+1/2}^{n+1/2}\right)\right.$$
$$\left. + \left(F_{j-1/2}^{n+1/2}A_{j-1/2}^{n+1/2} - F_{j+1/2}^{n+1/2}A_{j+1/2}^{n+1/2}\right) + \left(F_{k-1/2}^{n+1/2}A_{k-1/2}^{n+1/2} - F_{k+1/2}^{n+1/2}A_{k+1/2}^{n+1/2}\right)\right], \quad (2.10)$$

where A is the area of a cell face (see figure 2.1) and the Fs are fluxes defined as

$$F_{i\pm1/2}^{n+1/2} = \left(v_{r,i\pm1/2,j,k}^{n+1/2} - v_{0r,i\pm1/2}^{n+1/2}\right)\rho_{i\pm1/2,j,k}^{n}, \quad (2.11)$$

$$F_{j\pm1/2}^{n} = v_{\theta,i,j\pm1/2,k}^{n+1/2}\rho_{i,j\pm1/2,k}^{n}, \quad (2.12)$$

$$F_{k\pm1/2}^{n+1/2} = v_{\phi,i,j,k\pm1/2}^{n+1/2}\rho_{i,j,k\pm1/2}^{n}. \quad (2.13)$$

To obtain the densities at the interfaces ($\rho^n_{i\pm1/2}$) straight averages are computed of centered densities adjacent to the interface. The two centered subscripts have intentionally been omitted in the expressions for the fluxes and areas to reduce equation length (e.g. i was left off but $i+1/2$ was kept). Note that the densities in the fluxes are at time n and not $n+1/2$, so our solution algorithm is straightforwardly explicit, as is true for many 1D calculations. It is not possible to properly time center all terms without introducing a more complex implicit or multi-step explicit algorithm. With this expression for the fluxes, we can directly solve equation (2.10) for the density at the new time step.

2.2.3 Radial Grid Velocity

The final piece needed to complete the description is the calculation of the grid velocity. For a spherical shell to have constant mass, the net flow of mass into and out of that spherical shell must be zero. Summing up all the fluxes into and out of the individual horizontal cells in a spherical shell, substituting equation (2.11) in for the outer radial flux (at $i+1/2$) and setting the result equal to zero we arrive at the equation,

$$\begin{aligned} 0 &= \sum_{jk} \Big[\Big(F^{n+1/2}_{i-1/2} A^{n+1/2}_{i-1/2} \\ &- \left(v^{n+1/2}_{r,i+1/2} - v^{n+1/2}_{0r,i+1/2} \right) \rho^n_{i+1/2} A^{n+1/2}_{i+1/2} \Big) \\ &+ \left(F^{n+1/2}_{j-1/2} A^{n+1/2}_{j-1/2} - F^{n+1/2}_{j+1/2} A^{n+1/2}_{j+1/2} \right) \end{aligned}$$

$$+ \quad \left(F^{n+1/2}_{k-1/2} A^{n+1/2}_{k-1/2} - F^{n+1/2}_{k+1/2} A^{n+1/2}_{k+1/2}\right)\Big] . \tag{2.14}$$

Solving for the outer grid velocity, $v^{n+1/2}_{0r,i+1/2}$, produces an equation for calculating the new grid velocity,

$$\begin{aligned} v^{n+1/2}_{0r,i+1/2} &= \frac{-1}{\sum_{j,k} A^{n+1/2}_{i+1/2}\, \rho^{n}_{i+1/2,j,k}} \\ &\cdot \quad \sum_{jk} \Big[\left(F^{n+1/2}_{i-1/2} A^{n+1/2}_{i-1/2} - v^{n+1/2}_{r,i+1/2} \rho^{n}_{i+1/2} A^{n+1/2}_{i+1/2}\right) \\ &+ \quad \left(F^{n+1/2}_{j-1/2} A^{n+1/2}_{j-1/2} - F^{n+1/2}_{j+1/2} A^{n+1/2}_{j+1/2}\right) \\ &+ \quad \left(F^{n+1/2}_{k-1/2} A^{n+1/2}_{k-1/2} - F^{n+1/2}_{k+1/2} A^{n+1/2}_{k+1/2}\right)\Big] . \end{aligned} \tag{2.15}$$

The inner radial flux, $F^{n+1/2}_{i-1/2}$, is dependent on the grid velocity at the inner interface. At the first radial zone boundary next to the rigid core we impose both a zero radial velocity and grid velocity. Thus, equation (2.15) can be solved recursively from the model interior boundary to the surface to determine the grid velocity at all interfaces.

2.3 Computational Setup

2.3.1 Starting Model

The initial model for our adiabatic simulations is generated by requiring that it be in hydrostatic equilibrium. When this constraint is applied to the conservation equations the only terms that remain are the pressure and gravity terms in the radial

momentum conservation equation. In particular, there are no terms left in the internal energy conservation equation, and thus no equation to solve for the energy structure. To provide this information, an energy profile was generated from another stellar modeling code ROTORC (Deupree, 1990) and energies were interpolated in $\log(M_r)$ to cell centers. Once we impose the energy distribution, we can simultaneously solve the radial hydrostatic equilibrium finite difference equation and the equation of state for the pressure and density structure of the model given the spacing of the independent variable M_r. The radius is determined from the volume required to produce the calculated density from the mass of the shell. No convective model is included in the starting model because RR Lyrae do not have extensive convective regions to affect the structure. To induce pulsation a radial velocity profile from the linear, non-adiabatic, radial pulsation code, LNA, (Castor, 1971), modified to allow a gamma law gas, is imposed so that the model pulsates around the equilibrium point in either the fundamental or the first overtone modes.

2.3.2 The Grid and Numerical Details

The simulation volume is separated into cells bounded by intersecting surfaces. These surfaces are defined at constant values of the three independent variables M_r, θ, and ϕ. Dependent quantities ρ, E, and P are defined at cell centers and dependent quantities r, v_r, v_{0r}, v_θ, and v_ϕ are defined at appropriate cell interfaces. The models used for testing have 107 radial, 10 theta, and 10 phi zones. The number of radial and

angular zones was chosen as a compromise between the need for computational speed and the need to generate the motion we wished to follow. The inner 10 radial zones are handled in 1D as discussed in §2.2. The zone number at which the switch between 1D and 3D is made is chosen by the user. For the test cases used in this paper the total mass of the star was 0.575 $M_\odot$, with an initial mass spacing of 4.5×10^{-9} $M_\odot$ at the surface, and increasing by 10% each shell into the star. Both the θ and ϕ zones have a spacing of 1°, so that the total simulation volume covers 100 square degrees.

The equations outlined in §2.2.1 are in differential form and are approximated by appropriate finite difference expressions. Spatial differentials are approximated by differences between quantities at either cell centers or cell interfaces depending on whether the quantity being updated in time is interface centered or cell centered, respectively. Temporal differentials are approximated by differences between the current grid state and the updated grid state divided by the time step, Δt, computed as a fraction of the minimum time step allowed by the Courant condition for the model as a whole. This then allows us to explicitly solve for the updated grid state given the current grid state and the time step.

Equation (2.10) is written in finite volume form with fluxes defined at cell faces. The velocities required for these fluxes are already interface centered; however, the densities are not. In general, quantities that are needed at interfaces but defined at cell centers, and quantities that are needed at cell centers but defined at interfaces are approximated by averages of adjacent quantities. We have used artificial viscosity

given by (von Neumann & Richtmyer, 1950; Richtmyer & Morton, 1967) to smooth out numerical noise associated with steep gradients produced by shocks, together with a threshold velocity of one-hundredth of the local sound speed for turning on the artificial viscosity and have used weighted donor cell to control the well known numerical instability associated with centered advection terms (terms 2,3,4 on the left hand side of equations 2.2 to 2.6), with a weight of 0.1 on the upwind terms and 0.9 for centered terms.

2.3.3 Order of Calculation

The order of calculation follows that of Deupree (1977a) with a few minor modifications. We start by updating the three velocities using equations (2.3, 2.4, and 2.5) from time $n-1/2$ to $n+1/2$ using quantities at n (ρ, $\langle\rho\rangle$, r, and P) and quantities at $n-1/2$ (v_r, v_{r0},v_θ, and v_ϕ). Next the grid velocity is calculated at time $n+1/2$ using equation (2.15) working from inner boundary of the model to the surface in a recursive manner. The updated radius is computed with equation (2.7). The density is updated from n to $n+1$ using the equation for mass conservation (eq. (2.10)), with quantities at n (ρ and r), and quantities at $n+1/2$ (v_r, v_{r0}, v_θ, and v_ϕ). The energy is updated in a similar manner. The equation of state then allows us to compute the pressure at the new time step from the updated density and specific internal energy.

2.3.4 Parallelism

The code we have developed to perform these calculations has been named SPHERLS (Stellar Pulsation with a Horizontal Eulerian Radial Lagrangian Scheme). SPHERLS has been designed from the beginning to allow for parallel calculations using MPI protocols. The parallel design allows for domain decomposition in all three directions with the ability to vary the number of ghost cells (used to express the boundary conditions of the local domain) copied from other processors. Domain decomposition splits the problem up so that each processor only needs to solve it's local portion of the grid. This will be more complicated when the implicit solution is required but is still manageable. Note that boundary conditions in this sense are not the global boundary conditions of the calculation but only the information required from other processors to be able to perform the calculations on the processor in question. Equations (2.3), (2.4), (2.5), (2.6), (2.10) depend on only local quantities and are easily applied to the local grids on each processor. The equation to calculate the grid velocity (eq. (2.15)) requires information across all j and k space. Using this equation with domain decomposition in the j and k directions would require additional message passing which has not yet been implemented, and thus currently limits domain decomposition to the radial direction only. This could change in the future and may become helpful for optimizing calculations for larger horizontal grids.

During program initialization, each processor can be assigned different equations to solve on their local grid, which allows one to divide the computational domain up

into a 3D and a 1D region. The 1D region is composed of only a single zone at each i spanning all of j and k space. Quantities are volume averaged from the 3D region to the 1D region to be used as boundary conditions for the 1D region; while values in the 1D region are copied across j and k space to the 3D region to be used as boundary conditions there.

To date, only exploratory time trials have been performed because future additions to the code (including both an implicit solution to the energy equation with radiation diffusion and an eddy viscosity sub-grid-scale model) will impact the timing results significantly. At present, a calculation with $97 \times 10 \times 10$ 3D zones and 10 1D zones for 1 million time steps (10 million seconds, or approximately 178 fundamental mode periods) takes 2 processors 12^h22^m; 4 processors 5^h25^m; 8 processors 3^h28^m; and 16 processors 2^h29^m. At larger numbers of processors with the current gridding, the overhead from MPI begins to negate any additional benefits. Thus, for this gridding 16 processors represents the "sweet spot". At larger horizontal grid sizes the "sweet spot" will likely be pushed to larger numbers of processors.

2.4 Test Case Results

Five adiabatic test calculations have been performed using the method outlined above. The first calculation (CalI) was of a static stellar model with all velocities set to zero, which was used to test that the starting model was indeed generated in equilibrium consistently with respect to the hydrodynamic finite difference equa-

tions, and that SPHERLS's finite difference and finite volume representations of the hydrodynamic equations are hydodynamically stable. The second calculation (CalII) was a spherical blast wave (e.g. Sedov, 1959), used to test that the code could handle strong shocks and check it against an analytical solution. The third calculation (CalIII) was of a low amplitude radial pulsation (1 km s^{-1} initial surface velocity) in the fundamental mode with a horizontal velocity perturbation to break spherical symmetry. Spherical symmetry is broken to test our grid velocity algorithm under a case closer to convection, that simple spherically symmetric radial pulsation. The fourth calculation (CalIV) was of an even lower amplitude radial pulsation (0.1 km s^{-1} initial surface velocity) in the first overtone mode again with a horizontal velocity perturbation. These two low amplitude calculations were used to compare the calculated periods to the linear adiabatic periods, and to insure that the scheme worked as expected at low velocities. The lower velocity is needed for comparison with the linear LNA code which assumes small perturbations from the static model to calculate periods. The fifth calculation (CalV) started with the same stellar model as CalIII, but with a higher amplitude pulsation (10 km s^{-1} initial surface velocity) and a toroidal velocity perturbation instead of the horizontal velocity perturbation. This calculation was used to show that SPHERLS reproduced quantities well from one period to the next over many periods in the presence of weak shocks and large scale structured motions, more similar to convective motions.

The static calculation (CalI) started with all velocities (r, θ, and ϕ) set to zero

and was computed for over 20 million seconds (356 fundamental periods). The radial velocities in the surface zone reached the largest amplitudes. In this zone the radial velocity amplitude initially grew from zero to a temporal mean of about 3.7×10^{-5} cm s^{-1} within the first 80 periods. This mean was maintained for the rest of the calculation with a standard deviation of 2.7×10^{-5} cm s^{-1}. The horizontal velocities remain zero throughout the calculation. This is understandable because all terms in the horizontal momentum equations are zero and remain that way; while the radial momentum equation is the balance between two nonzero terms and thus subject to round off error.

To assure that the method is behaving as designed we checked the mass calculated from the averaged density, $\langle\rho\rangle$, and the shell volume (which is dependent on the radial grid velocity) with the mass set as the independent variable. The largest relative difference between the calculated mass and the independent mass variable for all calculations is 4×10^{-13}. This is only two significant digits above machine round off, and there are no signs of a trend with time.

To test how well SPHERLS handles strong shocks and to compare the computed results with an analytic calculation we performed a Sedov blast wave calculation (CalII). This calculation had 400 radial zones with an initial spacing of 10 cm and 10 θ and ϕ zones with spacings of 1°. The 400 radial zones produces a 40 m radius spherical volume for the shock to expand into, and was chosen to allow enough volume for the shock to expand into over 10 ms, at which time the analytic solution has

reached a shock radius of 32.7 m. The inner 10 radial zones were (as in the adiabatic stellar models) treated in 1D. The blast was accomplished by setting the initial energy in the inner 30 zones (i.e., a 3 m radius sphere) to 4.18×10^{21} ergs with all other zones having an energy of 1×10^6 ergs. The density was set to 2 g cm^{-3} through out the starting model. A gamma-law gas was used for the equation of state, with a γ of 1.6. All the initial velocities were set to zero and the blast was followed for 10 ms. The calculation was compared to an analytical solution with a point-source energy producing the blast, evaluated at times from 0.5 ms to 10 ms in 0.5 ms intervals. When comparing the extended-source to the point-source solution one would expect that at early times (when the shock is closer to the source), and at later times closer to the initial location of the source, the discrepancies between the computed and analytical solutions should be larger. This is because the differences between a non-point source calculation and the point source analytic solution will diminish as the disturbance moves outward. The blast radii computed by SPHERLS matched those form the analytic solution to within 7.5 cm at all times. The best match of shock radii (within 1.7 cm) occurred later in the calculation at a time of 10 ms, while the worst match (7.3 cm) occurred much earlier in the calculation at 3.5 ms. The computed velocity, density, and pressure profiles were also compared to the analytic solution, but because of the extended source, only the zones outside the initial explosion source were compared. The root mean square of the fractional error in velocity, density, and pressure was less than 3%, 8%, and 5% respectively in the last half of the calculation

(5 ms to 10 ms). In the first half of the calculation (0.5 ms to 5 ms) the root mean square of the fractional errors are a bit larger, mostly due to the difference between using an extended source in the calculation versus a point source in the analytic solution and are within 8%, 15%, and 11% for the velocity, density, and pressure respectively. The radial profiles of the velocity, density, and pressure fit quite well without any outlying points.

Because the calculations are adiabatic, we expect the pulsation to neither grow nor decay and to be reproducible from one period to the next. This should provide a good test to verify that our numerical algorithm functions as desired over many periods. Both the low amplitude fundamental and first overtone pulsation (CalIII and CalIV respectively) had a horizontal velocity perturbation imposed on them to test the grid velocity algorithm for nonspherically symmetric cases, by setting specific values of v_θ and v_ϕ at a central horizontal zone located at 90% of the total radius (18 zones in from the surface of the 107 radial zone models). The velocities were directed horizontally out of the zone through sides $A_{j\pm1/2}$ and $A_{k\pm1/2}$ (see figure 2.1). The magnitude of these horizontal velocities was taken to be half of the initial radial velocity at this radial location (0.3 km s^{-1} and 0.03 km s^{-1} for CalIII and CalIV respectively). Figure 2.2 shows a two-dimensional slice at constant ϕ of CalIII slightly after the initial conditions. The slice is at 7225 s into the calculation (relatively early in the 1×10^7 s calculation) and shows the disturbance resulting from the horizontal velocity perturbation as well as it's location and geometry with respect to the rest of

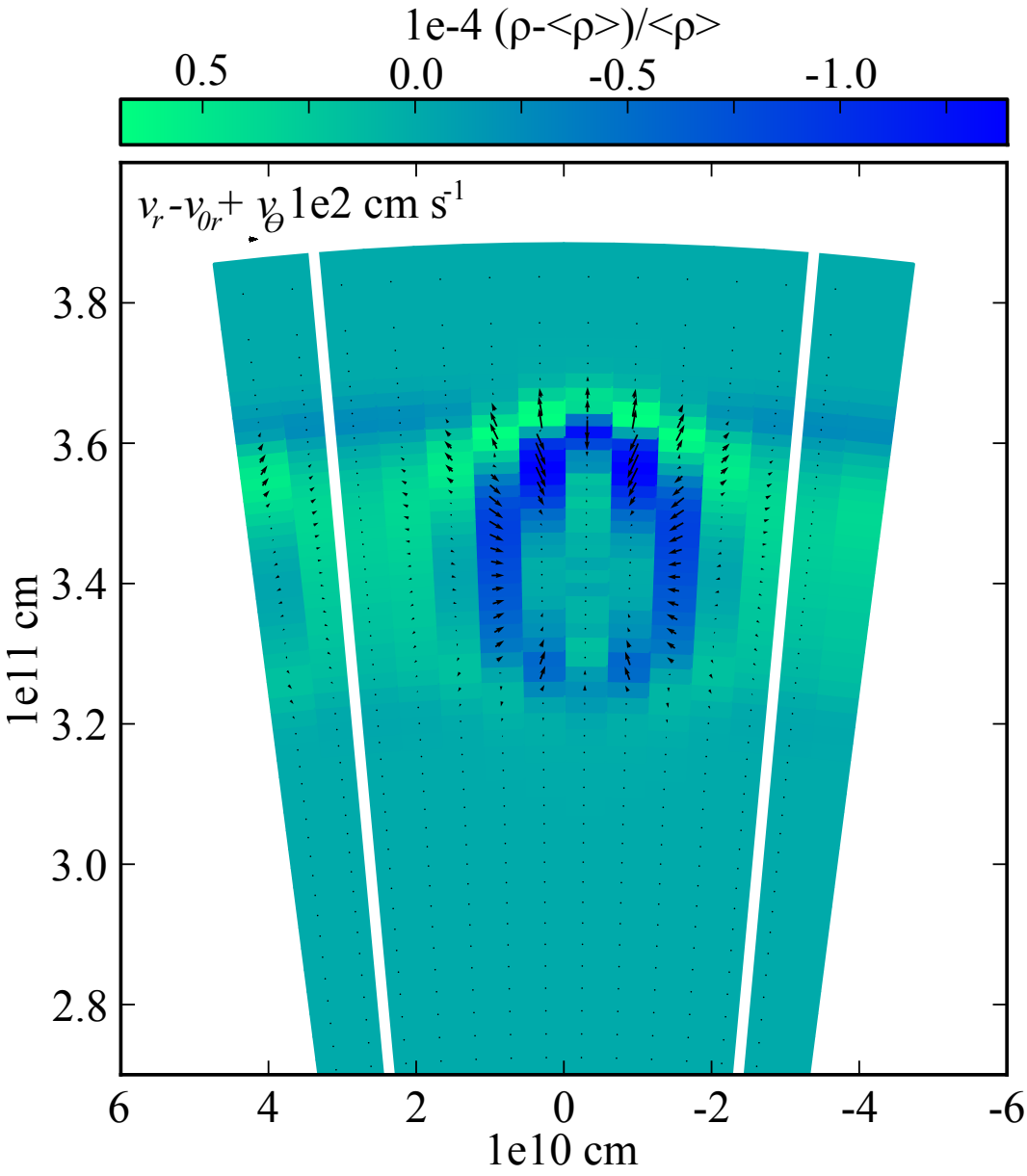

Figure 2.2: This figure shows a two-dimensional slice at constant ϕ (third ϕ zone) for CalIII. The color scale is $(\rho_{i,j,k} - \langle\rho\rangle_i)/\langle\rho\rangle_i)$ and vectors show the difference between the radial velocity and the grid velocity added vectorially with the θ velocity. The slice is at 7225 s into the calculation. Cells exterior to the white lines on the left and right sides are used to express the horizontal periodic boundary conditions. This figure shows only the outer 30% of the stellar radius, while the total simulation is of more than 85%.

the model.

The period of the fundamental mode is 56178 s for the low amplitude calculation (CalIII), and compares well with the period calculated from LNA of 56114 s. There is less than 0.12% difference between the periods of the two codes. The first overtone model (CalIV) was found to have a period of 38911 s and compares with the LNA period of 39522 s, producing less than a 1.6% difference.

In addition to the horizontal velocity perturbation we explored in CalIII and CalIV we also explored a velocity perturbation that is more structured over a larger scale (CalV). To create this model we started with the same structural model and radial velocity profile as Cal III, this time however, using a surface amplitude of 10 km s^{-1}. On top of the radial velocity profile we added a velocity perturbation in the shape of a torus (see figure 2.3 for torus geometry). The velocity perturbations were taken to be constant on the surface of the torus (the two circles in the lower half of figure 2.3) and parallel to the surface of the torus. By locating the closest point (defined by angles α and β) on the surface of the torus to the point P, the distance d in figure 2.3 can be calculated. Then a Gaussian centered on the surface of the torus with a maximum amplitude of 5 km s^{-1} is evaluated at d providing the velocity magnitude. The FWHM of the Gaussian is chosen so that the velocity perturbations do not overlap the other parts of the torus, and so that the velocity perturbations are still reasonably strong a zone or two away from the surface of the torus. The direction of the velocity is taken to be parallel to the surface of the torus at the location closest

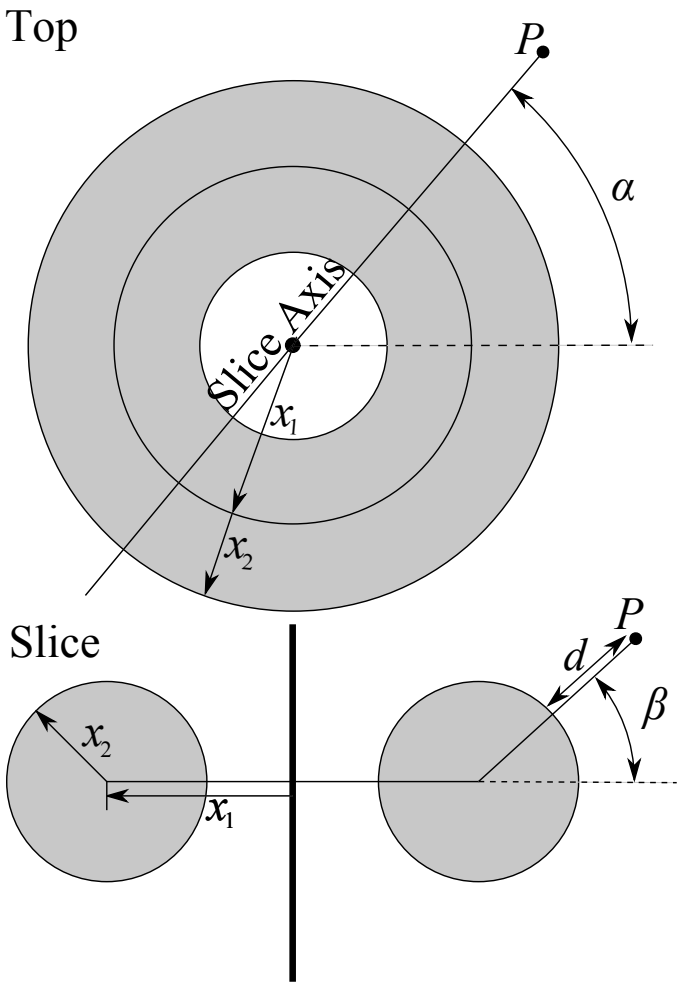

Figure 2.3: This figure shows the geometry of the torus used to define the toroidal velocity perturbations. x_1 and x_2 are two radii used to define the equation of torus. α and β are two angles used to define a point on the surface of the torus. The upper panel shows a top down view of the torus, while the lower panel shows the side view along the slice axis indicated in the top panel. The distance from an arbitrary point P to the surface of the torus is given by d.

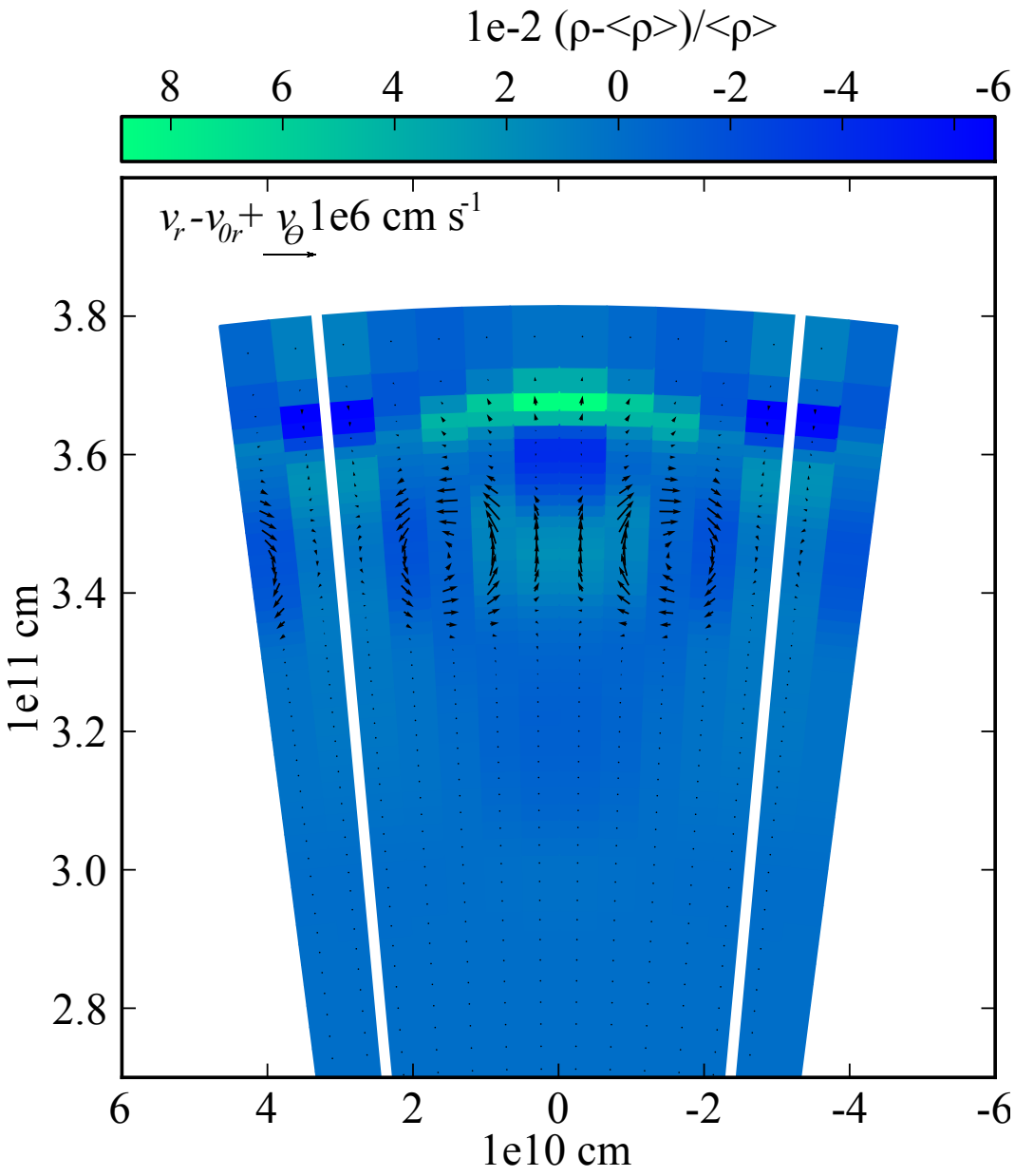

Figure 2.4: This figure shows a two-dimensional slice at constant ϕ (sixth ϕ zone) with vectors showing the difference between the radial velocity and the grid velocity added vectorially with the θ velocity. This plot is from CalV at 9031 s into the calculation. At later times the initial toroidal velocity perturbation has spread through out the model, making its initial form indiscernible.

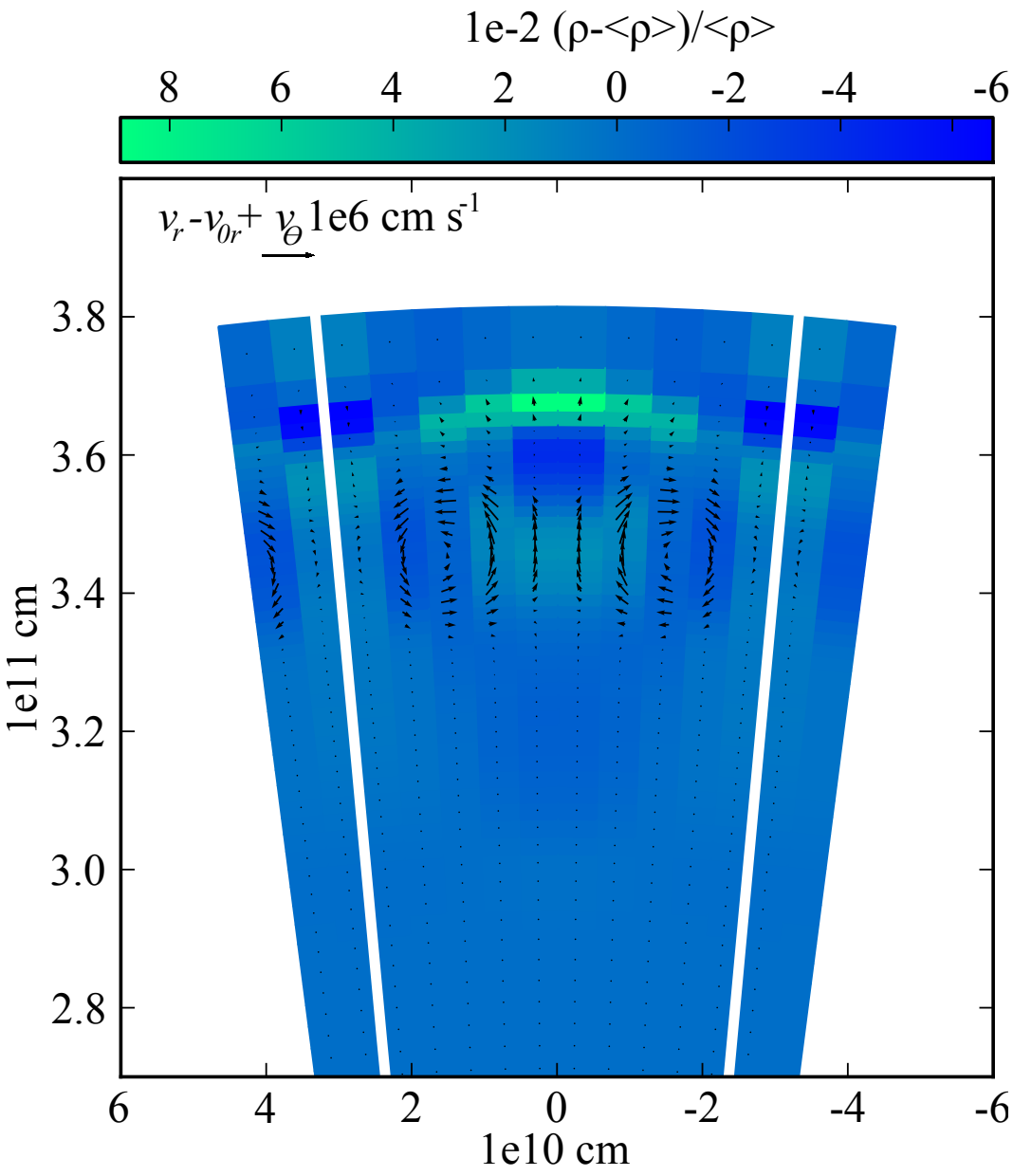

Figure 2.5: This figure shows a two-dimensional slice at constant θ (sixth θ zone) with vectors showing the difference between the radial velocity and the grid velocity added vectorially with the ϕ velocity. For the same calculation and time as figure 2.4.

to P. The velocity magnitude is then broken into r, θ, and ϕ components. The result of applying this perturbation is shown in figures 2.4 and 2.5. These figures show slices through the center of the model at constant θ and ϕ respectively, 9031 s into the calculation and indicate that θ and ϕ directions behave identically.

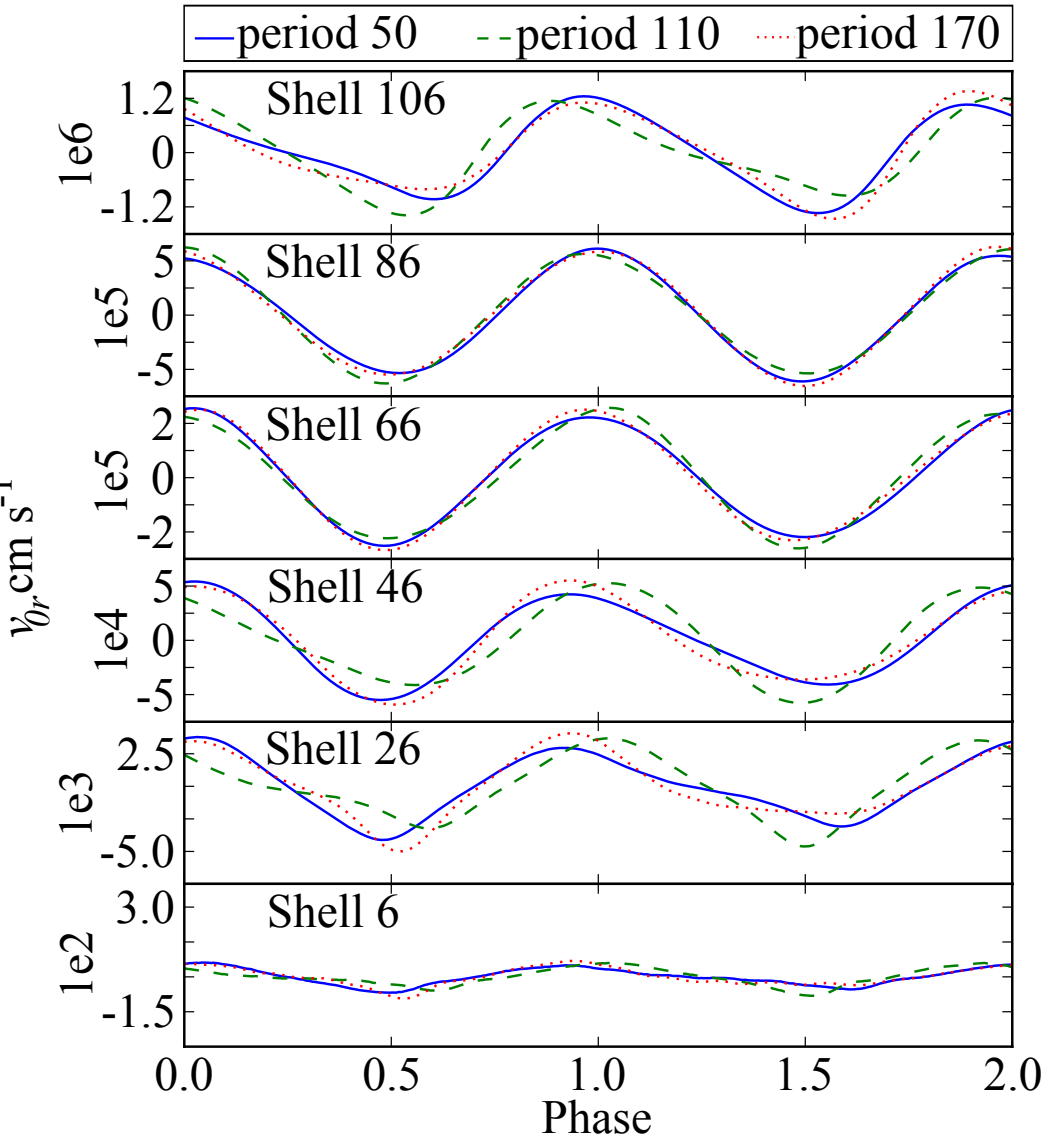

Figure 2.6: Radial grid velocity for three well separated periods, at six radial shells of the model for CalIV.

The high surface velocity model (CalV) results are presented in figures 2.6 and 2.7.

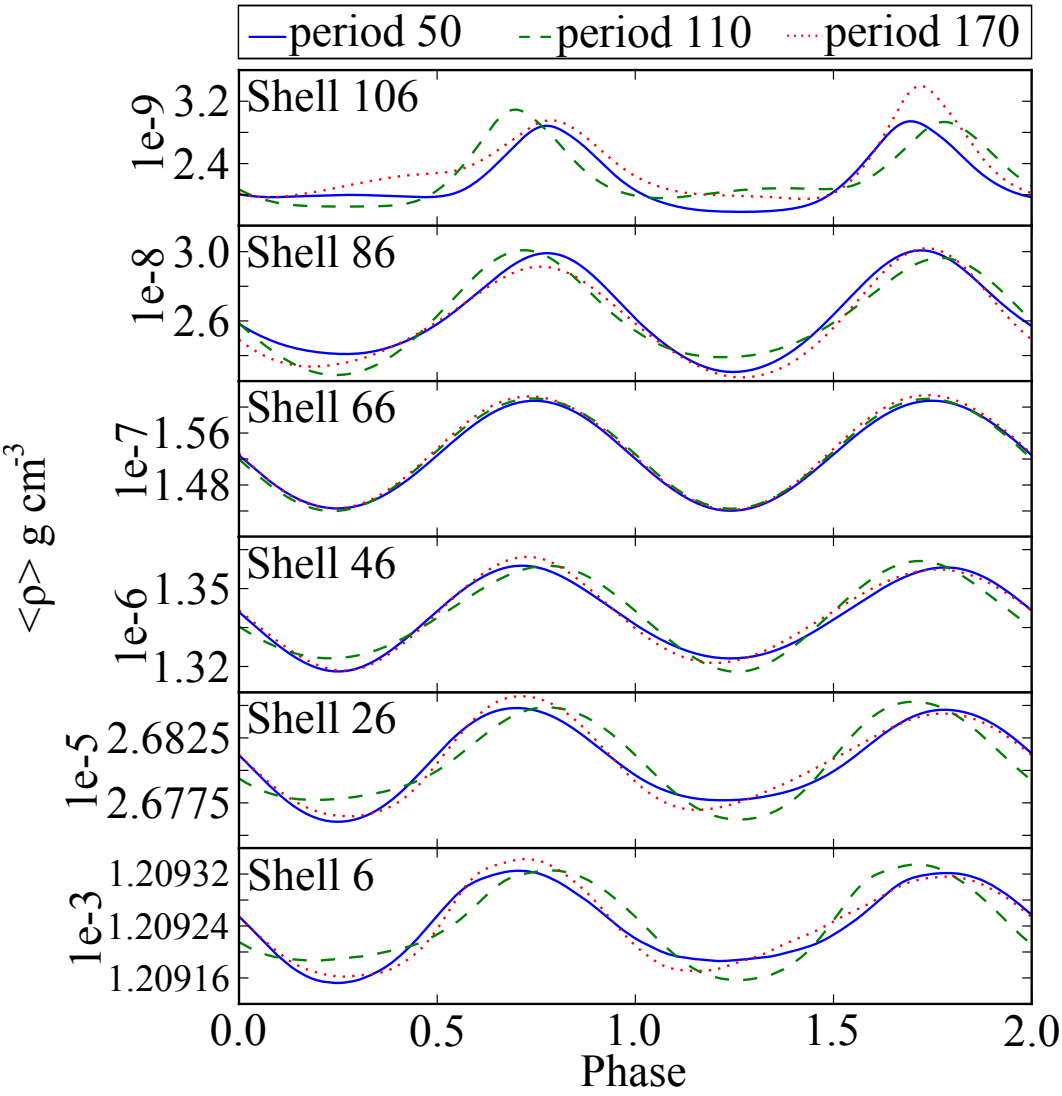

Figure 2.7: This figure is similar to figure 2.6 but for $\langle\rho\rangle$. The density is well reproduced across a large span of periods through the model, indicating that there is no drift of the radial coordinate system.

Figure 2.6 shows that the radial grid velocity throughout the model is well reproduced at periods 50, 110, and 170. Figure 2.7 shows that $\langle\rho\rangle$ is well reproduced over a large number of periods and does not show the drifting apparent in (Deupree, 1977a). The fact that the calculations of dependent quantities are reproduced over many periods shows that the scheme is working as desired and we expect to calculate full amplitude solutions of pulsating variable stars in the future.

A low radial surface velocity model(1 km s^{-1} surface velocity) that was spherically symmetric and did not use artificial viscosity has a very constant peak kinetic energies per period, with out any long term detectable growth or decay rates larger than $1 \times 10^{-11}\%$ per fundamental period. While CalIII, that had a horizontal velocity perturbation, had a growth rate of $4.3 \times 10^{-4}\%$ per fundamental period. In the high radial surface velocity calculation (CalV) artificial viscosity is required in the momentum equations (eq. 2.3, 2.4, and 2.5) to reduce the very steep pressure gradients at shocks. If it is omitted when pulsation amplitudes exceed the local sound speed it ultimately leads to negative densities and energies. One might argue that including the artificial viscosity in the energy equation would produce a non-adiabatic calculation, since the inclusion of the artificial viscosity raises the internal energy more than otherwise when the volume is decreasing. In CalV if the artificial viscosity is included in the energy equation we find that the peak kinetic energy decays at a rate 0.36% per fundamental period. If it is not included the peak kinetic energy decays at a rate of 0.13%. Ideally in the adiabatic case the peak kinetic energy should be constant.

These decay rates are dependent on the inclusion or omission of artificial viscosity in the energy equation, and may affect the amplitude of full amplitude solutions to some degree. This is not merely a concern for the present code, but for all non-linear hydrodynamics codes that use artificial viscosity.

2.5 Conclusions and Next Steps

We have developed a numerical algorithm and the computer code, SPHERLS, which is able to follow 3D adiabatic radial pulsations for many periods when spherical symmetry is broken. This is a necessary step for following the convective motions and radial pulsations of stars. We have shown that SPHERLS maintains hydrostatic equilibrium to a high degree over 356 fundamental periods. The radial Lagrangian algorithm for maintaining constant mass in the radial shells is effective over 178 periods to within one or two digits of machine round off, with no signs of any particular trend either decreasing or increasing.

We have found that SPHERLS reproduces both the fundamental and first overtone modes of the linear adiabatic code LNA reasonably well ($<0.12\%$ for fundamental and $< 1.6\%$ for first over tone). The velocities as well as other dependent quantities (e.g. the horizontally averaged density) are reproducible over many periods when spherical symmetry is broken, again indicating that our radial Lagrangian scheme is performing as designed.

Adiabaticity is maintained extremely well at low radial velocities when artificial

viscosity is not included. However at higher radial velocities some kinetic energy is converted into internal energy via the artificial viscosity required to smooth out shocks. This should be kept in mind while using any non-linear hydrodynamics code employing artificial viscosity to compare full amplitude solutions with observations.

In order to calculate full amplitude pulsating models to compare with observations a few additions must be made to SPHERLS. A more realistic equation of state and radiative Rosseland mean opacities must be included and radiation diffusion must be added to the energy equation. The latter is expected to require an implicit integration of the energy equation, at least near the surface, because optically thin zones would require a very small time step based on the speed of light and not the speed of sound. We expect to use the current explicit solution to the energy equation deeper in the envelope where the mean free path of photons is much less than a computational zone, keeping the calculation time down. Finally, we will add the subgrid scale terms required in a large eddy simulation for treating turbulent convection in the ionization zone.

3 Non-Adiabatic Models

To compare simulations with observations, as was mentioned in the previous chapter, the addition of radiative transport (using the diffusion approximation), a more realistic equation of state, Rosseland mean opacities, and a sub-grid scale turbulence model must be added to SPHERLS. In this chapter we will describe how these, as well as a few other minor changes and additions were made to SPHERLS.

3.1 Radiation Diffusion

Like most one dimensional codes, we include heating and cooling from radiation using the radiation diffusion approximation. This approximation is used in linear and non-linear codes alike. The radiation diffusion approximation is valid when the changes in density and temperature are small over the mean free path of a photon. Near the surface this assumption is no longer true and the validity of the diffusion approximation is questionable. However, Bendt & Davis (1971) found a basic similarity between multi-frequency transport and the transport from the diffusion approximation. More recently Feuchtinger et al. (2000) compared a calculation which used the diffusion approximation against a calculation which used time dependent radiative transfer and found only small differences in the pulsation amplitude. In addition Kolláth et al. (2000) explored the use of the radiation diffusion approximation near the surface and concluded that differences between observations and models are not

a result of this inadequate treatment of the radiation transport. Because we are performing calculations that have large computational requirements, including anything more sophisticated than radiation diffusion would likely appreciably increase the computational requirements of an already highly computationally intensive simulation.

The terms describing radiative heating using the diffusion approximation in three dimensions with spherical geometry are

$$\frac{4\sigma}{3\rho}\left[4\pi\langle\rho\rangle\frac{\partial}{\partial M_r}\left(\frac{4\pi\langle\rho\rangle r^4}{\kappa\rho}\frac{\partial T^4}{\partial M_r}\right)+\frac{1}{r\sin\theta}\frac{\partial}{\partial\theta}\left(\frac{\sin\theta}{\kappa\rho r}\frac{\partial T^4}{\partial\theta}\right)+\frac{1}{r\sin\theta}\frac{\partial}{\partial\phi}\left(\frac{1}{\kappa\rho r\sin\theta}\frac{\partial T^4}{\partial\phi}\right)\right]. \tag{3.1}$$

These terms are added to the right hand side of equation 2.6. Here T is the temperature, κ is the Rosseland mean opacity, both defined at cell centers, and σ is the Stefan-Boltzmann constant. These terms are converted to finite difference expressions in the manner discussed in section 2.3.2, and, except for the opacity, use straight averages to compute interface quantities from zone center quantities and visa versa. To obtain the opacities at interfaces an average between adjacent, zone centered, opacities weighted by the inverse of the flux (Christy, 1964) as

$$\frac{1}{\kappa_{i+1/2}}=\frac{\frac{T_{i+1}^4}{\kappa_{i+1}}+\frac{T_i^4}{\kappa_i}}{T_{i+1}^4+T_i^4} \tag{3.2}$$

is used. Another exception to the method described in section 2.3.2 is that various quantities are properly time centered. In particular $T^{n+1/2}=\frac{1}{2}\left(T^{n+1}+T^n\right)$ is used

instead of T^n , and the pressure, opacity, and energy, which depend on the temperature through the equation of state (described in section 3.3), are treated in the same way. The use of T^{n+1}, as it is initially unknown, is made possible by an implicit solution described in section 3.4. Finally these terms also affect how the initial model is generated, as presented in the next section.

3.2 Changes To Starting Model Generation

In section 2.3.1 we described the procedure for generating the starting model considering hydrostatic equilibrium for the adiabatic case. With the addition of the radiation diffusion terms to the energy equation an additional constraint can be applied to the starting model, by requiring that it also be in thermal equilibrium so that the luminosity is constant. This additional constraint removes the requirement for an energy profile from an outside source and greatly changes the procedure for generating the spherical starting model. To create a starting model including this new constraint first the hydrostatic and thermal equilibrium constraints are applied to the conservations laws, resulting in

$$f(T,\rho) = \frac{GM_r}{4\pi r^4} + \frac{\partial P}{\partial M_r} = 0 \tag{3.3}$$

and

$$g(T,\rho) = \frac{-64\pi^2\sigma r^4}{3\kappa}\frac{\partial T^4}{\partial M_r} - L = 0, \tag{3.4}$$

where L is the static model luminosity. These two equations are used to define the structure of the static, fully radiative initial model by starting at the surface with boundary conditions and integrating inward in a way that is consistent with the conservation equations. The temperature in the surface zone is determined using the relation $T^4 = \frac{3}{4} T_{\rm eff}^4 \, (\tau + 2/3)$ at an optical depth $\tau = 0$ so that

$$T_N = 2^{-1/4} T_{\rm eff} \tag{3.5}$$

where the subscript N indicates the surface zone. The mass zoning is specified by choosing an initial ΔM_r. The ΔM_r for the next zone is then the initial ΔM_r increased by a chosen percentage. This percentage can be changed at various temperatures within the model to achieve a zoning tailored to capture the steep gradients in the hydrogen ionization zone while keeping the total number of radial zones low. One might be tempted to set the mass outside the model to zero, $(\Delta M_r)_{N+1} = 0$, in practice the starting models have densities of about $10^{-10} - 10^{-11}$ gm cm^{-3} in the surface zone, while real stars have atmospheres with densities profiles that fall off with exponential tails toward zero, so that there is some additional mass outside the model at densities lower than the surface zone. To account for this $(\Delta M_r)_{N+1} = \alpha \, (\Delta M_r)_N$ with $\alpha = 0.2$ similar to 1D non-linear calculations by Stellingwerf (1975) and Gehmeyr (1992a).

The surface radius is calculated using the Stefan-Boltzmann law from the temperature and luminosity. The pressure in the surface zone, P_N, is calculated from

equation 3.3. Since r and M_r are known at the outer boundary and

$$\partial M_r = \frac{1}{2}\left[(\Delta M_r)_N + (\Delta M_r)_{N+1}\right] \tag{3.6}$$

is known, the only unknown is ∂P. P_N is determined from ∂P by setting the pressure at the outer interface to zero. With our finite difference scheme, at the outer interface of the surface zone, $P_{N+1/2} = \frac{1}{2}(P_N + P_{N+1}) = 0$ so that $P_N = -P_{N+1}$ and $\partial P = P_N - P_{N+1} = 2P_N$. Now the density must be determined, this is done by first picking an initial guess for the density; we use the average between the lowest two densities in the equation of state table. Then from the gradient of the pressure with respect to density and the pressure from the equation of state one can find the density that satisfies the hydrostatic condition by iteratively applying linear corrections to the density. We require that the density converges to within a relative error of 5×10^{-14}, near machine precision. Finally the equation of state is used to calculate the remaining quantities, E and κ.

After the quantities in the surface zone have been calculated initial guesses for the temperature and density for the next zone into the model are chosen from the values in the surface zone. The initial guess of the temperature and density are used to numerically calculate partial derivatives of the functions f and g which can be used to determine corrections to the initial guesses of the temperature and density of the

current zone using the set of linear equations

$$f + \frac{\partial f}{\partial T}\delta T + \frac{\partial f}{\partial \rho}\delta\rho = 0 \tag{3.7}$$

and

$$g + \frac{\partial g}{\partial T}\delta T + \frac{\partial g}{\partial \rho}\delta\rho = 0. \tag{3.8}$$

These two linear equations can be solved simultaneously for corrections to the temperature and density, δT and $\delta\rho$ respectively. Only a fraction of the corrections are applied to the density and temperature to help ensure convergence. Once the density and temperature have been corrected the process is repeated using the corrected density and temperature as the starting point until the corrections become small near machine precision.

After the temperature and density are determined the rest of the required quantities can be determined from the equation of state. ΔM_r for the next zone is calculated and the process repeated in this manner working into the star until the desired depth is reached, determined by reaching a chosen temperature (usually 3 million K, about $r = 0.1R_{N+1/2}$).

3.3 Equation of State and Opacities

This work primarily uses the OPAL opacities (Iglesias & Rogers, 1996) in combination with low temperature opacities from Alexander & Ferguson (1994). For

comparison purposes the King Ia table, (Cox & Tabor, 1976) opacities are also used. The equation of state in all cases is from Rogers et al. (1996). Figure 3.1 shows a comparison of the King Ia table with the OPAL tables for two different densities $\log_{10}\rho = -7$ and $\log_{10}\rho = -8$. The densities were chosen to cover both the hydrogen and helium ionization zones.

To facilitate fast linear interpolation of the equation of state and opacities in SPHERLS a rectangular table of $\log_{10} E$, $\log_{10} P$, and $\log_{10}\kappa$ as functions of $\log_{10}\rho$ and $\log_{10} T$ is used at fine enough resolution to maintain accuracy, especially in the ionization regions. The table must also be continuous in the second derivative to provide smooth first derivatives with respect to temperature and density for convergence purposes.

The first step is to combine the high and low temperature opacity tables for all the original tables to be used in the interpolation. To do so the opacities are averaged together in the region of temperature where the two tables overlap at each density. This average is weighted so that it smoothly approaches the OPAL opacities at the high temperature edge of the overlap region, and the Alexander & Ferguson opacities at the low temperature edge of the overlap region.

Then the equation of state and opacity tables are interpolated to the desired composition. The equation of state tables are available only at 3 values of Z, and thus a quadratic fit to the three compositions is used for interpolation in Z. As the equation of state tables are available at more than 3 values of X a one dimensional

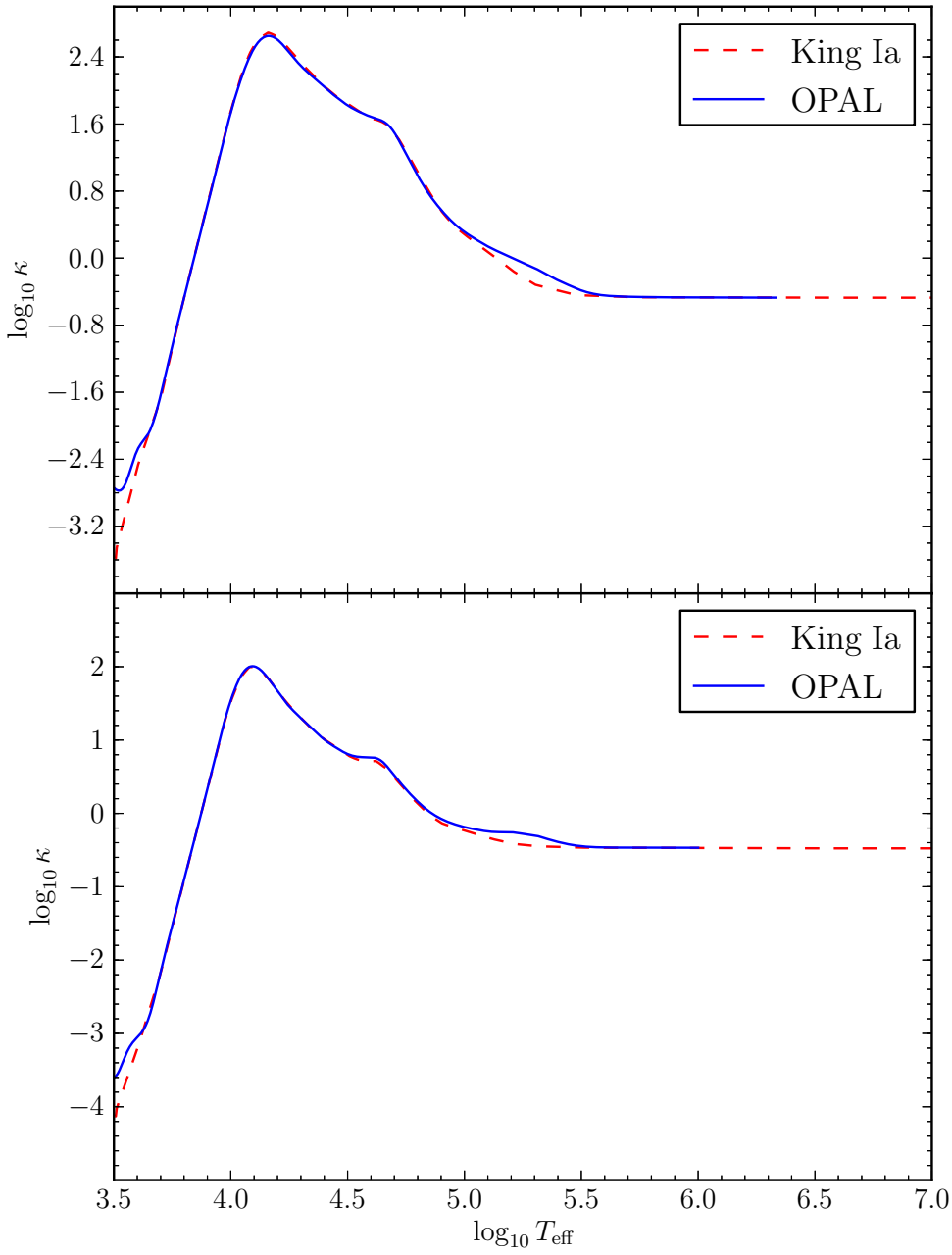

Figure 3.1: Comparison of King Ia and OPAL opacities. The top panel is for $\log_{10}\rho = -7$ and the bottom panel is for $\log_{10}\rho = -8$.

cubic spline interpolation is used. The opacity tables are available at more than 3 values of both Z and X and thus two dimensional cubic spline interpolation is used to obtain an opacity table at the desired composition.

Once the equation of state and opacity tables are created at the desired composition, two dimensional cubic spline interpolation is performed in $\log_{10} T$ and $\log_{10} \rho$ to create a finer rectangular equation of state table. Two dimensional cubic spline interpolation was performed in $\log_{10} T$ and $\log_{10} R$, where $R = \rho/(T/1e6)^3$, to create a finer rectangular opacity table. The final interpolated equation of state and opacity tables are then combined into a single table as functions of $\log_{10} T$ and $\log_{10} \rho$ to be used for linear interpolation (in the log) in SPHERLS.

3.4 Implicit Solution

The first nonlinear calculation of an initial value problem for a radially pulsating RR Lyrae star was performed by Christy (1964), who solved the energy equation implicitly. Christy realized that the implicit solution of the energy equation is necessary for stability as well as to make physical sense. Consider first the case of explicit calculation, the change in energy or temperature is calculated from only adjacent grid points, and therefore temperature information is able to propagate at most one zone in a time step. However, near the surface in optically thin regions radiation could easily transport energy through many zones within a very short time, and in this case the time step would not be governed by the sound speed as is the case in very

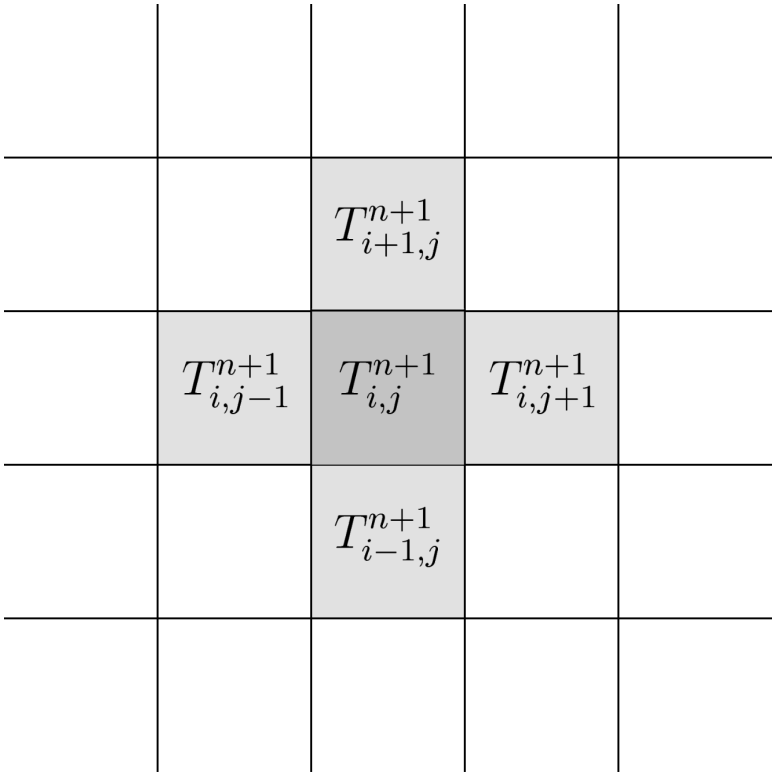

Figure 3.2: Two dimensional conservation equation stencil. Gray areas indicate the location of the stencil, and subscripts indicate the r and θ positions of the stencil zones relative to the stencil center i, j.

optically thick regions, but instead by the speed of light. The way around this serious restriction is to use an implicit method which couples the changes in a particular zone to the changes in all zones by solving a set of couple equations for these changes.

The energy equation can be regarded as a second order differential equation in all dimensions in temperature, with a seven, five or three point stencil in 3D, 2D, or 1D respectively (see figure 3.2 for a graphical depiction of the 2D stencil). The velocities and densities are integrated from the other equations, so that the implicit solution of the energy equation involves only the temperature (as pressure, specific internal energy and opacity are related to the density and temperature through the equation

of state), and the finite difference expression for the energy conservation equation can be written conceptually as,

$$f_{i,j,k}(T^{n+1}_{i,j,k}, T^{n+1}_{i+1,j,k}, T^{n+1}_{i-1,j,k}, T^{n+1}_{i,j+1,k}, T^{n+1}_{i,j-1,k}, T^{n+1}_{i,j,k+1}, T^{n+1}_{i,j,k-1}) = 0, \tag{3.9}$$

where the superscript $n+1$ indicates the new time step, and subscript indicates the grid location (e.g. i, j, and k indicates the r, θ, and ϕ cells respectively). The task is to solve for the new temperatures, keeping track of their influences on other hydrodynamical quantities through the equation of state, which satisfy equation 3.9. Note that in equation 3.9 we have written the function with subscripts also, to indicate that it is being evaluated in a specific zone.

The procedure to solve for these temperatures is iterative. We can take advantage of how the changes in temperatures affect the function $f_{i,j,k}$ to move linearly towards temperatures which satisfy equation 3.9. If we expand equation 3.9 with a Taylor series keeping only the linear terms we arrive at

$$\begin{aligned} f_{i,j,k} \quad &+ \quad \frac{\partial f_{i,j,k}}{\partial T^{n+1}_{i,j,k}}\delta T^{n+1}_{i,j,k} + \frac{\partial f_{i,j,k}}{\partial T^{n+1}_{i+1,j,k}}\delta T^{n+1}_{i+1,j,k} + \frac{\partial f_{i,j,k}}{\partial T^{n+1}_{i-1,j,k}}\delta T^{n+1}_{i-1,j,k} \\ &+ \quad \frac{\partial f_{i,j,k}}{\partial T^{n+1}_{i,j+1,k}}\delta T^{n+1}_{i,j+1,k} + \frac{\partial f_{i,j,k}}{\partial T^{n+1}_{i,j-1,k}}\delta T^{n+1}_{i,j-1,k} \\ &+ \quad \frac{\partial f_{i,j,k}}{\partial T^{n+1}_{i,j,k+1}}\delta T^{n+1}_{i,j,k+1} + \frac{\partial f_{i,j,k}}{\partial T^{n+1}_{i,j,k-1}}\delta T^{n+1}_{i,j,k-1} = 0. \end{aligned} \tag{3.10}$$

If an initial guess for the temperatures at the new time step is chosen (e.g. we use the temperature at the last time step, T^n), then everything but the δT's can be evaluated

and equation 3.10 represents a linear equation with seven unknowns. If we apply this to the other zones the result is $N_i \times N_j \times N_k$ δT's and the same number of equations, where the N's are the number of zones in each of the three directions of the region in which the implicit solution is applied. The boundary conditions are what allow this system of equations to be closed.

To describe how this works over all zones let

$$J^{i,j,k}_{l,m,n} = \frac{\partial f_{i,j,k}}{\partial T^{n+1}_{l,m,n}} \tag{3.11}$$

be the element in the $(k+j\times N_k+i\times N_k\times N_j)^{\text{th}}$ row and the $(n+m\times N_k+l\times N_k\times N_j)^{\text{th}}$ column of the matrix $\mathbf{J}$. Let $\delta T_{l,m,n}$ be the $(n + m \times N_k + l \times N_k \times N_j)^{\text{th}}$ element of the column vector $\delta\mathbf{T}$. Finally let $-f_{i,j,k}$ be the $(k + j \times N_k + i \times N_k \times N_j)^{\text{th}}$ element of the column vector $\mathbf{f}$. Then the equation 3.10 for all zones can be written in matrix notation as

$$\mathbf{J}\delta\mathbf{T} = \mathbf{f}. \tag{3.12}$$

Solving this matrix equation provides the correction vector $\delta\mathbf{T}$ to be applied to the initial guesses of the new temperatures. The procedure is then applied until the corrections to temperature become small. $\mathbf{J}$ is a band diagonal matrix since zones not within the stencil of another zone will have zero partial derivatives with respect to each other. The width of the band is dependent on the size of the grid and will have a width of $(2 \times N_\theta \times N_\phi + 1)$.

The periodic boundary conditions require that as the stencil reaches the edges, quantities outside the mesh, must come from the opposite side of the mesh. For example in the zone $(i, j, k) = (0, 0, 0)$ equation 3.10 will include a term which will fill in a zero element within the band, namely

$$J^{0,0,0}_{N_\theta-1,0,0} = \frac{\partial f_{0,0,0}}{\partial T_{N_\theta-1,0,0}} \delta T_{N_\theta-1,0,0}. \tag{3.13}$$

When the mesh becomes very small so that the stencil wraps around onto its self, due to the periodic boundary conditions, the **J** terms sum. For example if $N_\theta = N_\phi = 2$ then in zone $(i, j, k) = (0, 0, 0)$

$$J^{0,0,0}_{0,1,0} = \frac{\partial f_{0,0,0}}{\partial T_{0,1,0}} \delta T_{0,1,0} + \frac{\partial f_{0,0,0}}{\partial T_{0,-1,0}} \delta T_{0,-1,0} = 2\frac{\partial f_{0,0,0}}{\partial T_{0,1,0}} \delta T_{0,1,0} \tag{3.14}$$

from the periodic boundary condition. There are many zero elements in this matrix which never change during a calculation since their location only depends on the zoning and boundary conditions. Knowing where all the non-zero elements are in the matrix can be used to increase speed and accuracy of the solution and to reduce the storage space required for the coefficient matrix, **J**.

To solve this system of equations we use the Krylov subspace method, implemented in the PETSc library (Balay et al., 2012). This allows one to solve a large system of linear equations, quickly and accurately utilizing the message passing interface (MPI) to solve a single system using many processors at once.

3.5 Subgrid Scale Turbulence Model

A subgrid scale turbulence model is used to convert kinetic energy at the small scale back into thermal energy. In nature this is done by intermolecular forces or viscosity. In stars this conversion would happen on scales far smaller than those of the computational grid by many orders of magnitude. Subgrid scale turbulence models make the assumption that the large scale flows can be used to model how the subgrid scale feeds back to the large scale. In practice there are many variations on how one can do this. Since our calculations are computationally limited we choose to use a simple model based on work by Cloutman (1991) and described in Deupree (1996) and similar to Scannapieco & Brüggen (2008). Scannapieco & Brüggen used a similar model in a completely different regime to model AGN-driven turbulence in galaxy clusters, with the main difference between his model and that of Cloutman is the addition of a transport equation for the eddy length scale. We have made some modifications to simplify Cloutman's implementation and reduce the computational requirements while still being an improvement on that used by Deupree (1977a).

The basic approach for developing a subgrid scale model is to write the quantities in the conservation equations as the sum of a mean component and a subgrid-scale component. The conservation equations are then expanded so that the original equations are recovered with the original quantities replaced by the mean components and many additional terms involving the subgrid-scale components which must be approximated from the mean components. Some of the terms involving the subgrid-

scale components have physical significance, (e.g. a viscosity) and are kept; others which involve higher powers of the subgrid components are omitted.

Cloutman models the subgrid scale terms in momentum equations as a viscosity,

$$\nabla \cdot \tau \tag{3.15}$$

where τ is the Newtonian stress tensor

$$\tau = \mu \left[\nabla \vec{u} + (\nabla \vec{u})^T \right] + \lambda \left(\nabla \cdot \vec{u} \right) \mathbf{U}, \tag{3.16}$$

where μ and λ are first and second viscosity coefficients respectively, $\vec{u}$ is the velocity vector, $\mathbf{U}$ is the identity matrix, and $(\nabla \vec{u})^T$ refers to the transpose of the two-dimensional tensor composed of the gradient of $\vec{u}$. If we assume zero bulk viscosity then $\lambda = -2/3\mu$. We want to model the effects of the unresolved small scale flow in the momentum equation as an effective viscosity and not the intrinsic viscosity of the gas. We, thus replace μ with μ_t, the turbulent eddy viscosity. The simplest description of this eddy viscosity was given by Smagorinsky (1963) as

$$\mu_t = \frac{C^2 l^2 \rho}{\sqrt{2}} \left(\nabla \vec{u} : \left[\nabla \vec{u} + (\nabla \vec{u})^T \right] \right)^{1/2}. \tag{3.17}$$

where l is the length scale of a grid zone, and C is a constant of approximately 0.17 based on comparison between calculations and experiments by Deardorff (1971). The : indicates to take the dyadic double product. Cloutman (1991) solves a transport

equation for the turbulence kinetic energy, $\mathcal{K}$, and uses the relation

$$\mu_t = A_t \rho L \mathcal{K}^{1/2} \tag{3.18}$$

to calculate the eddy viscosity where $L = 3.75 \times l$ and A_t is a constant equal to 0.117; instead we use this relationship between $\mathcal{K}$ and μ_t to calculate a turbulence kinetic energy from Smagorinsky's algebraic equations for the eddy viscosity (eq. 3.17). We then use this $\mathcal{K}$ in Cloutman's term in the energy equation which mimics the conversion of subgid-scale convergence of kinetic energy into internal energy.

With these assumptions, the final forms of the momentum and energy conservation equations, including the radiation diffusion and the sub-grid-scale model, in spherical coordinates are

$$\begin{aligned}
\frac{\partial v_r}{\partial t} &+ 4\pi r^2 \langle\rho\rangle \left(v_r - v_{0r}\right) \frac{\partial v_r}{\partial M_r} + \frac{v_\theta}{r}\frac{\partial v_r}{\partial \theta} + \frac{v_\phi}{r\sin\theta}\frac{\partial v_r}{\partial \phi} \\
&= \frac{-4\pi r^2 \langle\rho\rangle}{\rho}\frac{\partial P}{\partial M_r} + \frac{v_\theta^2}{r} + \frac{v_\phi^2}{r} - \frac{GM_r}{r^2} + \left(\frac{1}{r^2}\frac{\partial}{\partial r}\left(r^2\tau_{rr}\right)\right. \\
&+ \left.\frac{1}{r\sin\theta}\frac{\partial}{\partial\theta}\left(\sin\theta\tau_{\theta r}\right) + \frac{1}{r\sin\theta}\frac{\partial}{\partial\phi}\left(\tau_{\phi r}\right) - \frac{\tau_{\theta\theta}+\tau_{\phi\phi}}{r}\right),
\end{aligned} \tag{3.19}$$

$$\begin{aligned}
\frac{\partial v_\theta}{\partial t} &+ 4\pi r^2 \langle\rho\rangle \left(v_r - v_{0r}\right) \frac{\partial v_\theta}{\partial M_r} + \frac{v_\theta}{r}\frac{\partial v_\theta}{\partial \theta} + \frac{v_\phi}{r\sin\theta}\frac{\partial v_\theta}{\partial \phi} \\
&= \frac{-1}{r\rho}\frac{\partial P}{\partial \theta} + \frac{v_\phi^2\cot\theta}{r} - \frac{v_r v_\theta}{r} + \left(\frac{1}{r^2}\frac{\partial}{\partial r}\left(r^2\tau_{r\theta}\right)\right. \\
&+ \left.\frac{1}{r\sin\theta}\frac{\partial}{\partial\theta}\left(\sin\theta\tau_{\theta\theta}\right) + \frac{1}{r\sin\theta}\frac{\partial}{\partial\phi}\left(\tau_{\phi\theta}\right) + \frac{\tau_{\theta r}}{r} - \frac{\cot\theta\tau_{\phi\phi}}{r}\right),
\end{aligned} \tag{3.20}$$

$$\begin{aligned}
\frac{\partial v_\phi}{\partial t} &+ 4\pi r^2\langle\rho\rangle\left(v_r - v_{0r}\right)\frac{\partial v_\phi}{\partial M_r} + \frac{v_\theta}{r}\frac{\partial v_\phi}{\partial \theta} + \frac{v_\phi}{r\sin\theta}\frac{\partial v_\phi}{\partial \phi} \\
&= \frac{-1}{\rho r\sin\theta}\frac{\partial P}{\partial \phi} - \frac{v_r v_\phi}{r} - \frac{v_\theta v_\phi\cot\theta}{r} + \left(\frac{1}{r^2}\frac{\partial}{\partial r}\left(r^2\tau_{r\phi}\right)\right. \\
&+ \left.\frac{1}{r\sin\theta}\frac{\partial}{\partial\theta}\left(\sin\theta\tau_{\theta\phi}\right) + \frac{1}{r\sin\theta}\frac{\partial}{\partial\phi}\left(\tau_{\phi\phi}\right) + \frac{\tau_{\phi r}}{r} + \frac{\cot\theta\tau_{\phi\theta}}{r}\right), \qquad (3.21)
\end{aligned}$$

and

$$\begin{aligned}
\frac{\partial E}{\partial t} &+ 4\pi r^2\langle\rho\rangle\left(v_r - v_{0r}\right)\frac{\partial E}{\partial M_r} + \frac{v_\theta}{r}\frac{\partial E}{\partial\theta} + \frac{v_\phi}{r\sin\theta}\frac{\partial E}{\partial\phi} \\
&+ \frac{4\pi\langle\rho\rangle P}{\rho}\frac{\partial\left(r^2 v_r\right)}{\partial M_r} + \frac{P}{\rho r\sin\theta}\frac{\partial\left(v_\theta\sin\theta\right)}{\partial\theta} + \frac{P}{\rho r\sin\theta}\frac{\partial v_\phi}{\partial\phi} \\
&= \frac{4\sigma}{3\rho}\left[4\pi\langle\rho\rangle\frac{\partial}{\partial M_r}\left(\frac{4\pi\langle\rho\rangle r^4}{\kappa\rho}\frac{\partial T^4}{\partial M_r}\right) + \frac{1}{r\sin\theta}\frac{\partial}{\partial\theta}\left(\frac{\sin\theta}{\kappa\rho r}\frac{\partial T^4}{\partial\theta}\right)\right. \\
&+ \left.\frac{1}{r\sin\theta}\frac{\partial}{\partial\phi}\left(\frac{1}{\kappa\rho r\sin\theta}\frac{\partial T^4}{\partial\phi}\right)\right] + \frac{1}{\rho}\left[4\pi\langle\rho\rangle\frac{\partial}{\partial M_r}\left(\frac{4\pi\langle\rho\rangle r^4\mu_t}{\rho Pr_t}\frac{\partial E}{\partial M_r}\right)\right. \\
&+ \frac{1}{r\sin\theta}\frac{\partial}{\partial\theta}\left(\frac{\sin\theta\mu_t}{\rho Pr_t r}\frac{\partial E}{\partial\theta}\right) \\
&+ \left.\frac{1}{r\sin\theta}\frac{\partial}{\partial\phi}\left(\frac{\mu_t}{\rho Pr_t r\sin\theta}\frac{\partial E}{\partial\phi}\right)\right] + \frac{D_t\mathcal{K}^{3/2}}{L} \qquad (3.22)
\end{aligned}$$

where

$$\tau_{rr} = 2\mu_t\left(\frac{\partial u}{\partial r} - \frac{1}{3}\nabla\cdot\vec{u}\right), \qquad (3.23)$$

$$\tau_{\theta\theta} = 2\mu_t\left(\frac{1}{r}\frac{\partial v}{\partial\theta} + \frac{u}{r} - \frac{1}{3}\nabla\cdot\vec{u}\right), \qquad (3.24)$$

$$\tau_{\phi\phi} = 2\mu_t\left(\frac{1}{r\sin\theta}\frac{\partial w}{\partial\phi} + \frac{u}{r} + \frac{v\cot\theta}{r} - \frac{1}{3}\nabla\cdot\vec{u}\right), \qquad (3.25)$$

$$\tau_{r\theta} = \tau_{\theta r} = \mu_t\left(\frac{1}{r}\frac{\partial u}{\partial\theta} + \frac{\partial v}{\partial r} - \frac{v}{r}\right), \qquad (3.26)$$

$$\tau_{r\phi} = \tau_{\phi r} = \mu_t\left(\frac{1}{r\sin\theta}\frac{\partial u}{\partial\phi} + \frac{\partial w}{\partial r} - \frac{w}{r}\right), \qquad (3.27)$$

$$\tau_{\theta\phi} = \tau_{\phi\theta} = \mu_t \left(\frac{1}{r \sin\theta} \frac{\partial v}{\partial \phi} + \frac{1}{r} \frac{\partial w}{\partial \theta} - \frac{w \cot\theta}{r} \right). \tag{3.28}$$

$$\tag{3.29}$$

The values of the constants $D_t = 1.4$, $Pr_t = 0.7$ (the turbulent Prandtl number) are from Cloutman (1991). Equations 3.19 – 3.22 with the mass conservation equation, (eq. 2.10) represent the final form of the conservation equations, and equation 3.17 is used to analytically calculate an eddy viscosity coefficient.

One other difference from the work in chapter 2 is a change to the calculation of the donor cell weight. In section 2.3.2 we used a constant donor cell weight of 0.9 on upwind advection gradients and 0.1 on centered advection gradients. In the final version of the code the upwind donor cell weight, f, is dynamically adjusted between $f = 1$ and 0.2 with the centered term having a weight of $1 - f$. f is calculated at each radial zone at each time-step from the ratio of the maximum convective velocity over the local sound speed for that radial shell. If this ratio is larger than 1 it is set to 1, and if smaller than 0.2 it is to 0.2.

4 1D Models

As a precursor to the multi-dimensional calculations we have calculated a number of one-dimensional (radiation only) models. These models serve two major purposes. They were helpful in examining the parameter space or model properties and they provide a fiducial point to compare with the 2D and 3D convective models. A basic set of 1D calculations used for general information is summarized in table 4.1. Further 1D models were computed to compare with specific two and three-dimensional calculations and will be presented in the next chapter. All entries in table 4.1 were computed at temperatures of 6000, 6100, 6200, 6300, 6500, 6700 and 6900 K. All calculations have the same composition of X=0.7 and Z=0.001, which was chosen to match the composition of the King Ia opacity table (Cox & Tabor, 1976) and the same OPAL equation of state from Rogers et al. (1996). The calculations were computed at two different masses (0.575 and 0.7 $M_{\odot}$), with two different opacity tables (King Ia opacity table and the OPAL opacity table (Iglesias & Rogers, 1996)), and with two different initial surface velocities for the radial pulsation velocity profiles. The relative radial velocity profiles were taken from linear, adiabatic calculations of the radial eigenfunctions made with the LNA code (Castor, 1971).

The peak kinetic energy of the radial pulsation is generally used for measuring the growth or decay of a mode. The cessation of peak kinetic energy growth indicates when the radial pulsation reaches full amplitude. The top panels of figures 4.1 to 4.5

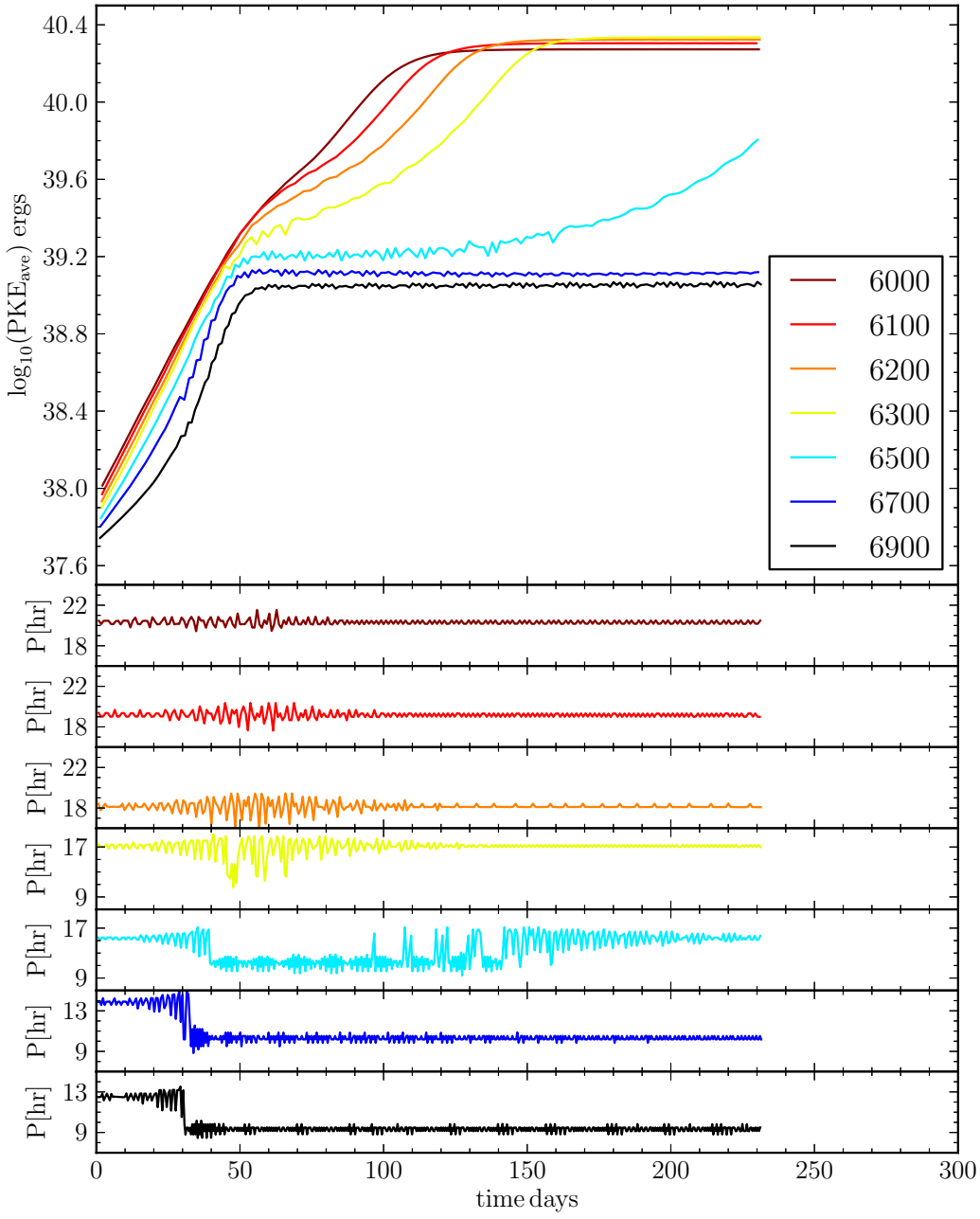

Figure 4.1: Upper panel shows the log of peak kinetic energy while the lower panel shows the periods in hours. This figure is for the calculation set using KING opacities, a mass of M=0.575$M_\odot$, and with the radial pulsation initiated at 2 km s^{-1}.

$(u_0)_{\text{surf.init.}}$ km s^{-1}	Opacity table	Mass M$_\odot$
2	KING Ia	0.575
2	OPAL	0.575
2	KING Ia	0.7
2	OPAL	0.7
10	OPAL	0.7

Table 4.1: One-dimensional calculation set parameters. Each set has models calculated at temperatures of 6000, 6100, 6200, 6300, 6500, 6700 and 6900 K and a composition of X=0.7, and Z=0.001

show the growth of the peak kinetic energy averaged over three fundamental periods for the various sets of calculations. The average is meant to remove variations due to contamination from the first overtone mode as this time interval is approximately four first overtone periods (Christy, 1964). Though these calculations are initiated in the fundamental mode, the initial linear mode is not strictly correct at higher non-linear amplitudes and contamination from the first overtone and probably higher overtones occurs.

The bottom panels of figures 4.1 to 4.5 show the period as a function of time, as determined from the time between every other peak in kinetic energy (there are two peaks in the kinetic energy per period, one for expansion and one for contraction). From the periods it is clear when the mode changes from the fundamental to the first overtone, as there is a large drop in the period to about 0.72 times the fundamental period. The mode can also be discerned from the magnitude of the peak kinetic energy when it levels off, although this is not as direct an indicator as the period.

From examining these figures one notes three main observations. First, at low mass growing from a low amplitude radial pulsation (compare figures 4.2 and 4.1)

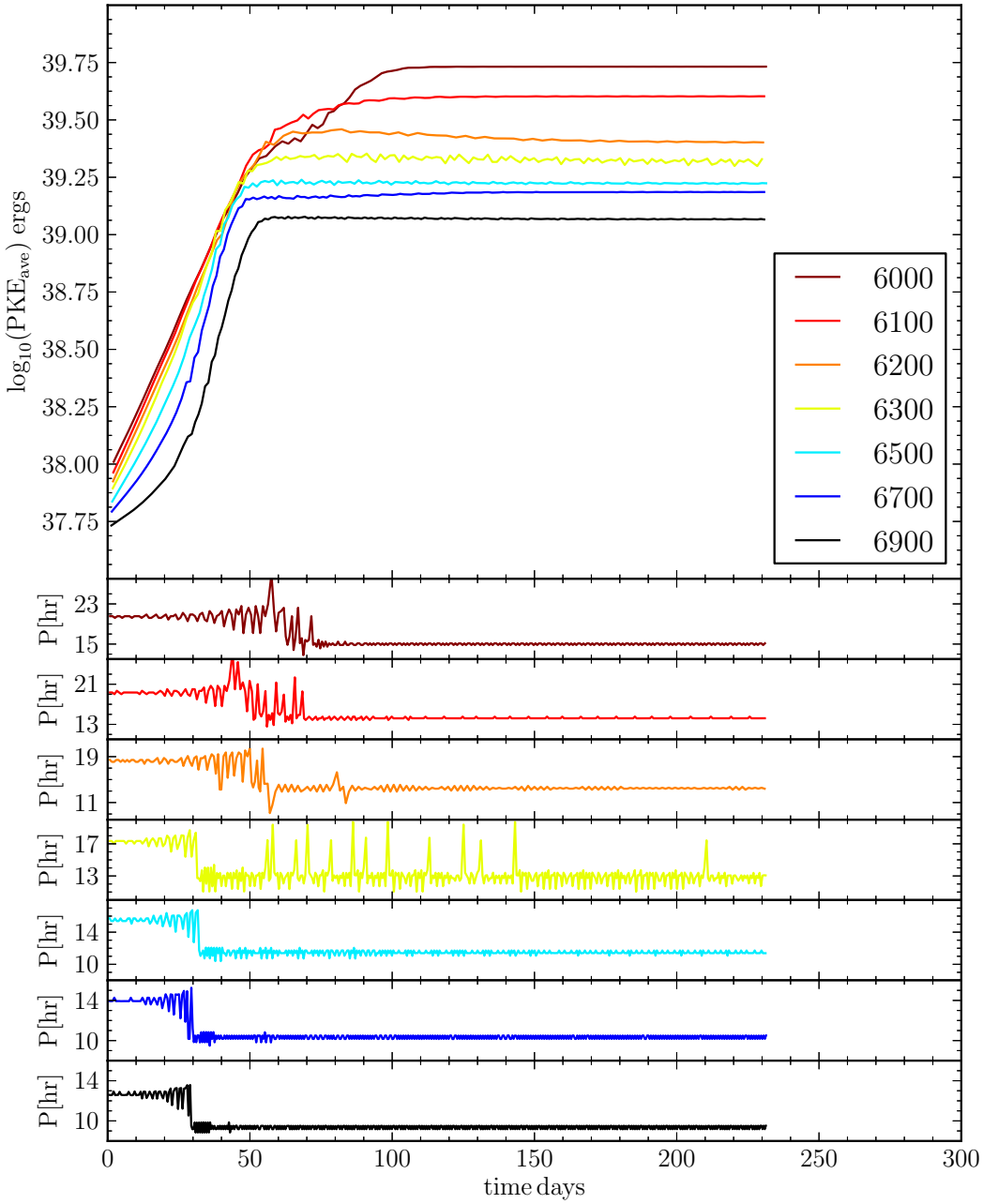

Figure 4.2: Similar to figure 4.1 except for the OPAL opacities.

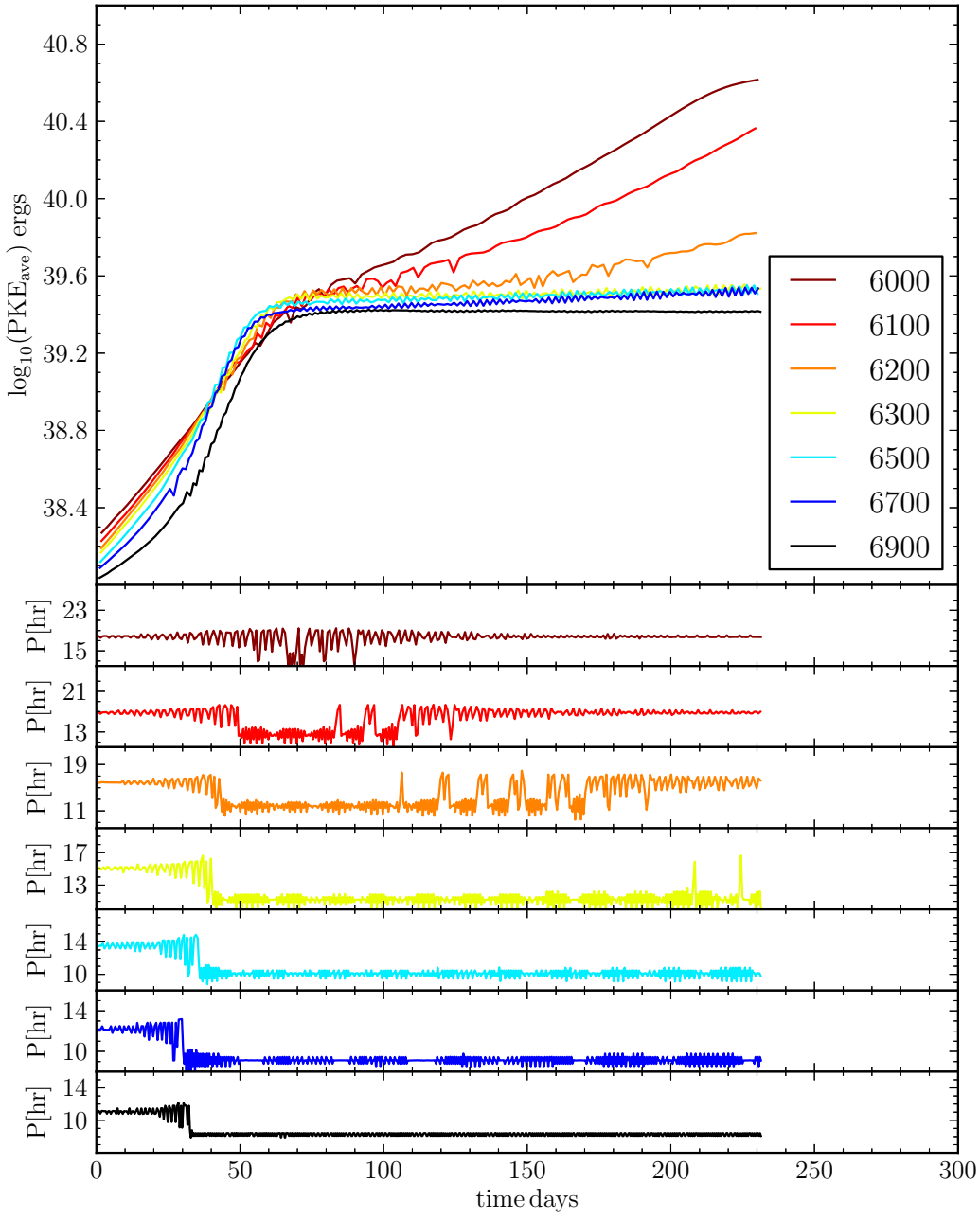

Figure 4.3: Upper panel shows the log of peak kinetic energy while the lower panel shows the periods in hours. This figure is for the calculation set using KING opacities, a mass of M=0.7$M_\odot$, and with the radial pulsation initiated at 2 km s^{-1}.

the King Ia and OPAL tables have very different temperature at which they switch from the fundamental to the first overtone mode. The radial pulsation calculations using the OPAL tables all grew into the first overtone in the range of temperatures explored, while the calculations using the King Ia table grew into either the fundamental or first overtone with the switch between the two modes occurring between 6500 (fundamental) and 6700 (first overtone). Second, at higher mass, for models started at low amplitude, the switch between the first overtone and fundamental modes occurs at about the same temperature between 6200 (fundamental) and 6300 (first overtone) for both the King and OPAL opacity tables (compare figures 4.4 and 4.3). Finally, models starting at a higher amplitude, which encourages the mode to remain the fundamental mode it started in more than the low amplitude calculations, the temperature at which the mode switches is increased (compare figures 4.4 and 4.5). For the OPAL tables with a mass of 0.7 $M_{\odot}$ starting with an initial surface radial velocity of 2 km s^{-1}, the switch between modes occurs between 6100 (fundamental) and 6200 (first overtone). For the calculations initiated at 10 km s^{-1} the switch occurs between 6500 and 6700 K. If calculations are initiated at even higher radial velocities of 20 km s^{-1} the 6700 K model remains in the fundamental mode, while the 6900 K model decays and would likely end up in the first overtone if given enough time.

It should be noted from the figures that many models, particularly those at low temperature, that change from the fundamental to the first overtone also change back

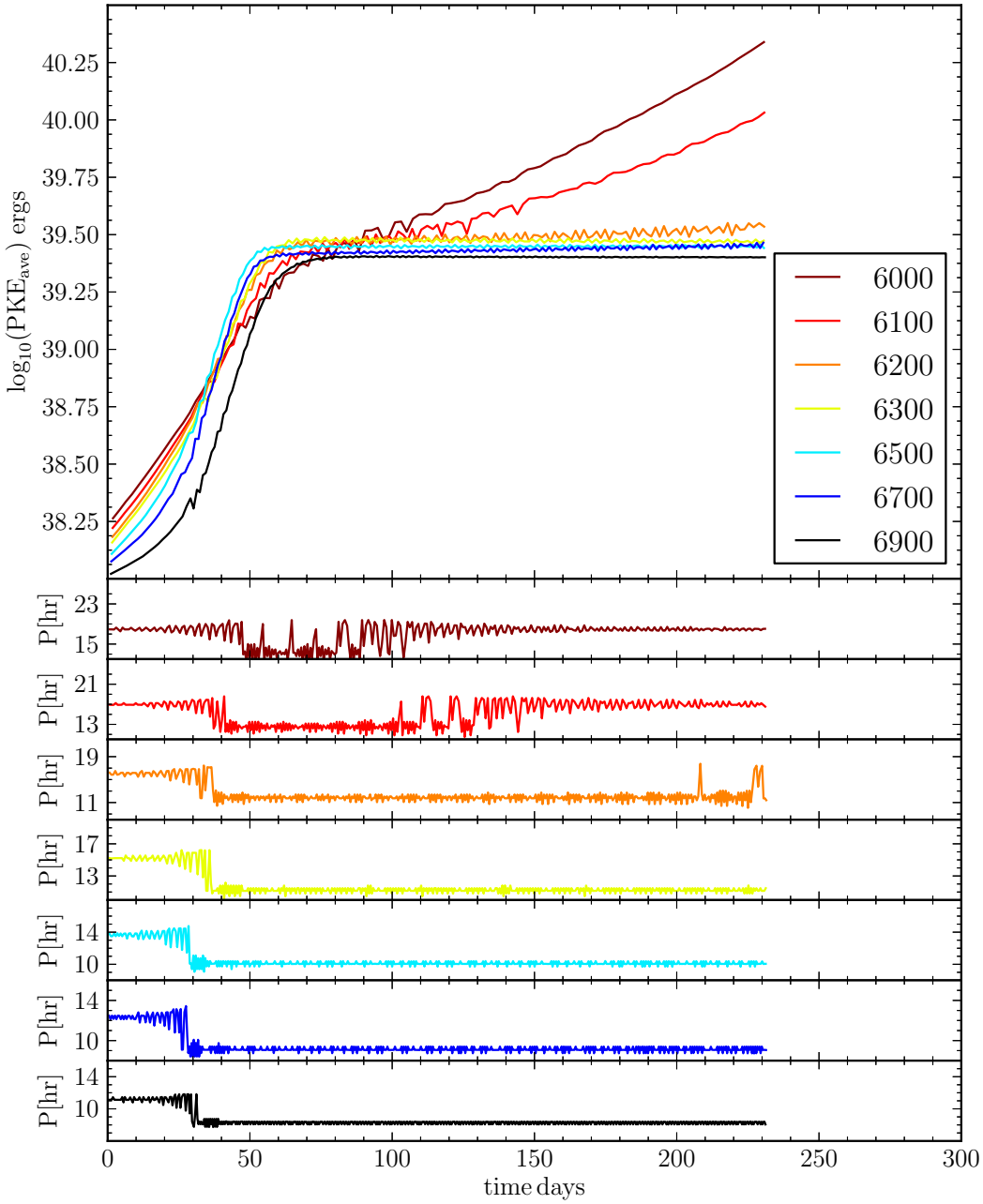

Figure 4.4: Similar to figure 4.3 except for the OPAL opacities.

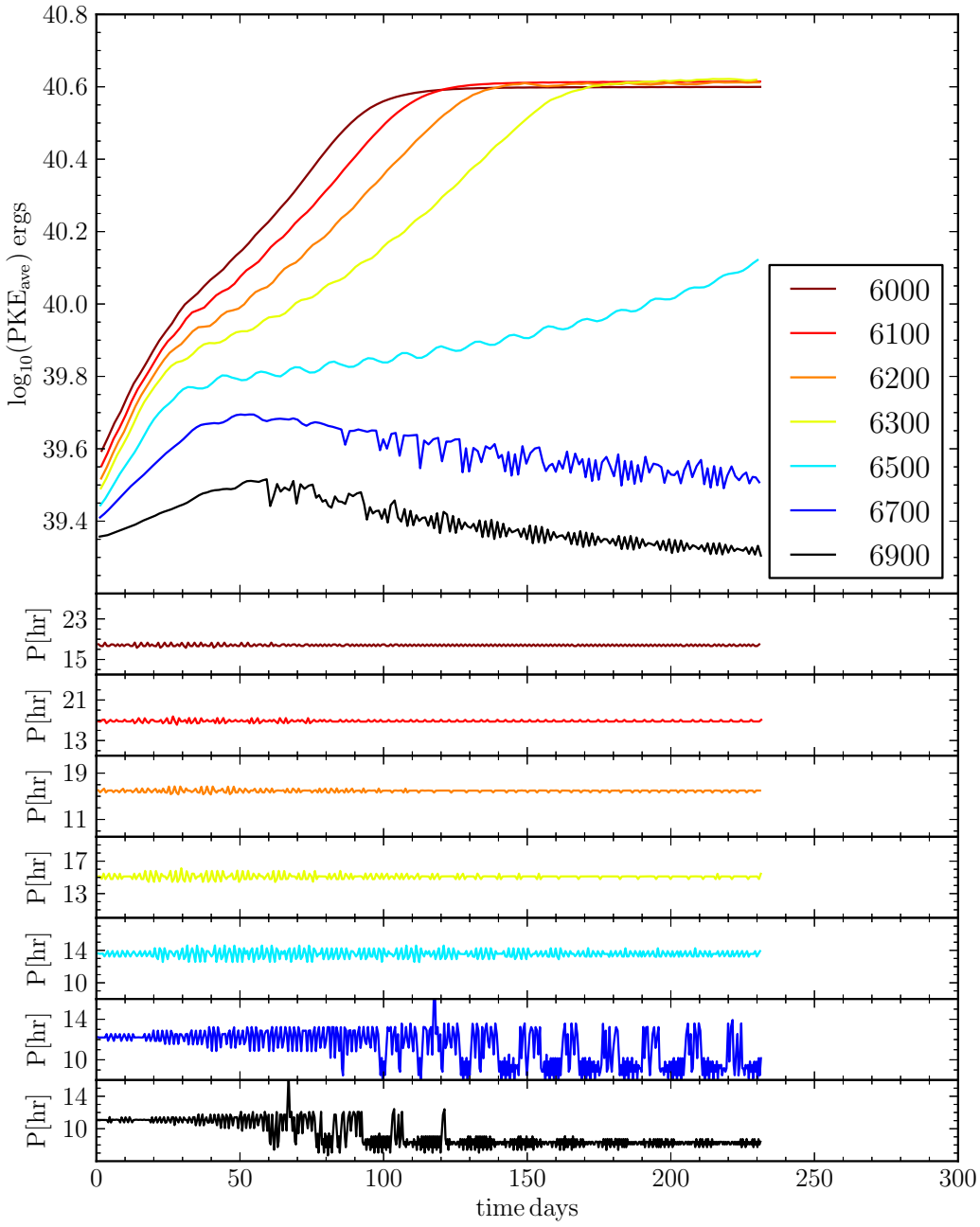

Figure 4.5: Similar to figure 4.4 except the radial pulsation was initiated at 10 km s^{-1} instead of 2 km s^{-1}.

to the fundamental at later time. The time at which this second transition begins is later for higher temperature models.

The causes for these various mode switches depend at least on the model effective temperature, model mass, the model initial velocity amplitude, and the details of the opacity table. There is no reason to believe, while interesting, that these are the only properties which influence this behavior. Further exploration of this phenomenon is beyond the scope of this work.

5 2D Models

In the last chapter we discussed 1D models (radiation only). We extend the work to 2D models. These models include convection using two dimensional versions of the conservation equations together with the constitutive and radial grid flow equations, outlined in chapters 2 and 3. This formulation of convection allows the convective flow to arise naturally from the conservation equations, albeit only in two spatial dimensions. The convective motions grow in regions unstable to convection from small deviations from the spherical model resulting from machine round off errors. In regions stable to convection and which are sufficiently far from convectively unstable regions, the gas motions, other than radial pulsation, remain small, near machine precision. The convective velocities discussed in this and succeeding chapters are measured from the radial, θ, and ϕ velocities with the radial grid velocity subtracted from the radial velocity. The intent of defining the convective velocity in this way is to obtain a measure of the convective motion without including the radial pulsation motion, although this definition of the convective motion may not strictly measure actual convective velocities.

Our computational domain covers a pie slice of 6^o and extends down to more than 90% of the star by radius. The angular size of this region was chosen from an examination of 3D simulations (see chapter 6) of various angular extents in which we found that 6^o is large enough for more than one 3D convective cell to form, ensuring

that the convective cells may grow to their preferred size and are not limited by the extent of the simulation. The radial extent was chosen so that the details of the nuclear reactions could be ignored while still producing the correct observational radial pulsation periods. In chapter 6 we will discuss in more detail the dependence of convection on the zoning of the simulation.

We have computed a number of 2D models at effective temperatures ranging from 6200 to 6900 K in steps of 100 K. These models all have a mass of 0.7 $M_{\odot}$, a static model luminosity of 50 $L_{\odot}$, and use the OPAL opacities and equation of state. The composition of all 2D models was chosen to be X=0.7595, Z=0.0005. The models had radial pulsation initiated in the fundamental mode from the linear eigenfunctions scaled to have a surface radial velocity of either 10 km s^{-1} or 20 km s^{-1}. The mass, luminosity, and composition were chosen to be representative of RR Lyrae variables in M 3 as follows. The mass and luminosity were selected by taking an average of RR Lyrae masses and luminosities in M 3 as determined by Cacciari et al. (2005). The composition's helium mass fraction, Y=0.24, is the same value used by Marconi & Degl'Innocenti (2007) for comparison of 1D models to M 3's observed RR Lyrae light curves. The metal mass fraction selected was slightly larger than that assumed by Bono et al. (1997b) of Z=0.0004 for M 3 while lower than the value used by Marconi & Degl'Innocenti (2007) of 0.001. One goal of the present work is to compare our treatment of convection, especially for cooler models, with the 1D mixing length prescription. For such a comparison modest composition variations such as these play

only a minor role. Ideally one would like to compute a number of models at various compositions, masses, and luminosities for comparison with observations. However, the computational requirements to cover this large parameter space with even modest resolution (e.g. all possible combinations of two values of the four parameters of mass, luminosity, Y, and Z results in sixteen effective temperature sets) with this approach to convection is prohibitive, and beyond the scope of the present work.

5.1 Interaction of Convection and Pulsation

The driving mechanism for pulsation, as described in section 1.2, delays the release of energy in the ionization regions via the kappa mechanism, giving the star a push in the outward direction during expansion to drive pulsation. One hypothesis of early work (e.g. Tuggle & Iben, 1973) was that the presence of even time independent convection allowing energy out through the ionization zone much more efficiently at all phases of pulsation would circumvent the kappa mechanism and quench pulsation at the red edge of the instability strip. As was mentioned in section 2.1 work by Tuggle & Iben attempted a time-independent convective model based on mixing-length theory. The result was that while it reduced the growth rate of pulsation, especially near the red edge, the growth rate never became negative. A negative growth rate would indicate that the initial pulsation mode imposed on the model was stable, and that convection could quench pulsation. While a smaller growth rate towards the red edge was an improvement over fully radiative models, it was not what

was required to quench pulsation.

Later work by Deupree (1977a) showed it was not that convection carried a large portion of the flux always, negating the kappa mechanism, but instead it is the time dependence of convection that is important for damping pulsation. The time dependence is such that convection carries a large amount of flux through the ionization zone during contraction (normally when the kappa mechanism would dam energy up), and a minimal amount of flux during the expansion phase (normally when the kappa mechanism would be releasing energy). This time dependence of convection on pulsation phase does more than simply remove the driving mechanism from the ionization zone, it turns this zone into a damping region if convection carries a sufficient amount of the total flux.

The present work also explores the time dependence by computing the convective flux, the amount of energy carried radially by convection per unit area. The approach to calculating this quantity is to assume that the amount of energy carried by convection is related to the difference between the temperature of given cell and the horizontal average of the temperature, ΔT, multiplied by the specific heat at constant pressure, c_P, and the mass flux across the outer radial interface of the shell. This results in

$$F_{\text{conv.}} = c_P \rho \left(v_r - v_{r0} \right) \Delta T. \tag{5.1}$$

Equation 5.1 may not be entirely correct as it assumes that the energy deposited or removed from the surroundings by the rising or falling material is a result of the ma-

terial reaching thermal equilibrium with the surroundings. This may not be entirely correct if the material rises or falls again before it equilibrates to the horizontal average temperature. It is also assumed that the horizontal pressure variation is negligible, which while not exact, is not a bad approximation. Hydrodynamic convection in a pulsating environment is a complex phenomenon in which material is being entrained or removed from upward or downward flows continuously. This means that the instantaneous convective flux may not be a complete measure of the longer timescale energy transport. While equation 5.1 may not be exact it should provide a good relative measure of the energy carried by convection for comparisons among the various models.

Figures 5.1 and 5.2 show how the maximum convective flux throughout the model varies with time for the 6300, and 6700 K models respectively. As the model contracts to minimum size, the convective flux grows. While the model begins to expand the maximum convective flux drops steeply. This is the same time dependence that Deupree found to quench pulsation at the red edge of the RR Lyrae instability strip. It is also clear when comparing the two figures, that the maximum convective flux is greatly reduced in the hotter model so that the role of convection becomes less important as the model effective temperature becomes higher.

Interestingly, we find the strength of convection increases with increasing pulsation amplitude. We show this in figure 5.3 for the 6500 K model. The flux in figure 5.3 is computed in the following manner: for each time we compute the maximum convective

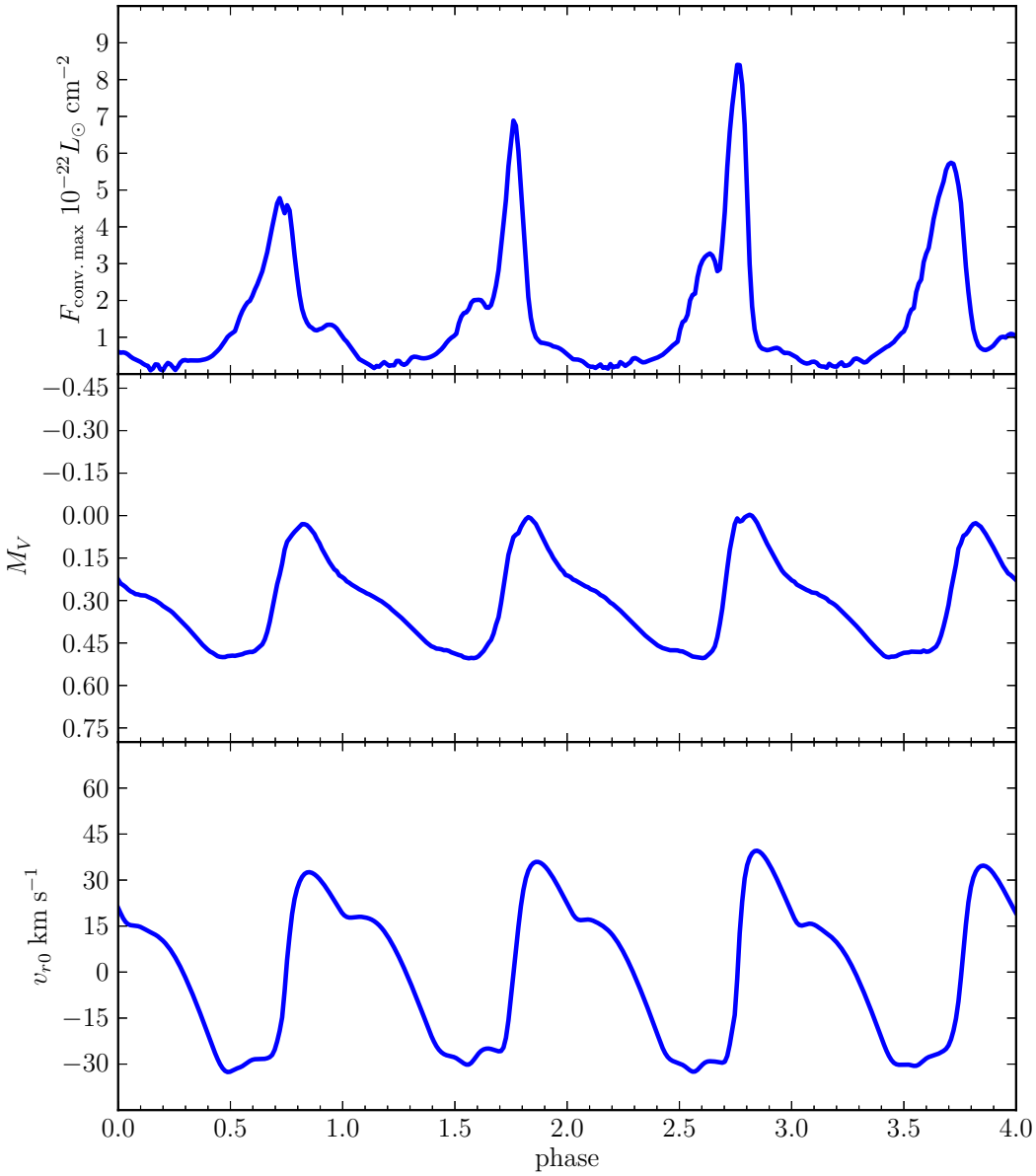

Figure 5.1: Convective time dependence of 6300 K effective temperature model. Top panel shows the maximum of the convective flux through out the model, the middle panel shows the absolute visual magnitude, and the bottom panel shows the surface radial grid velocity.

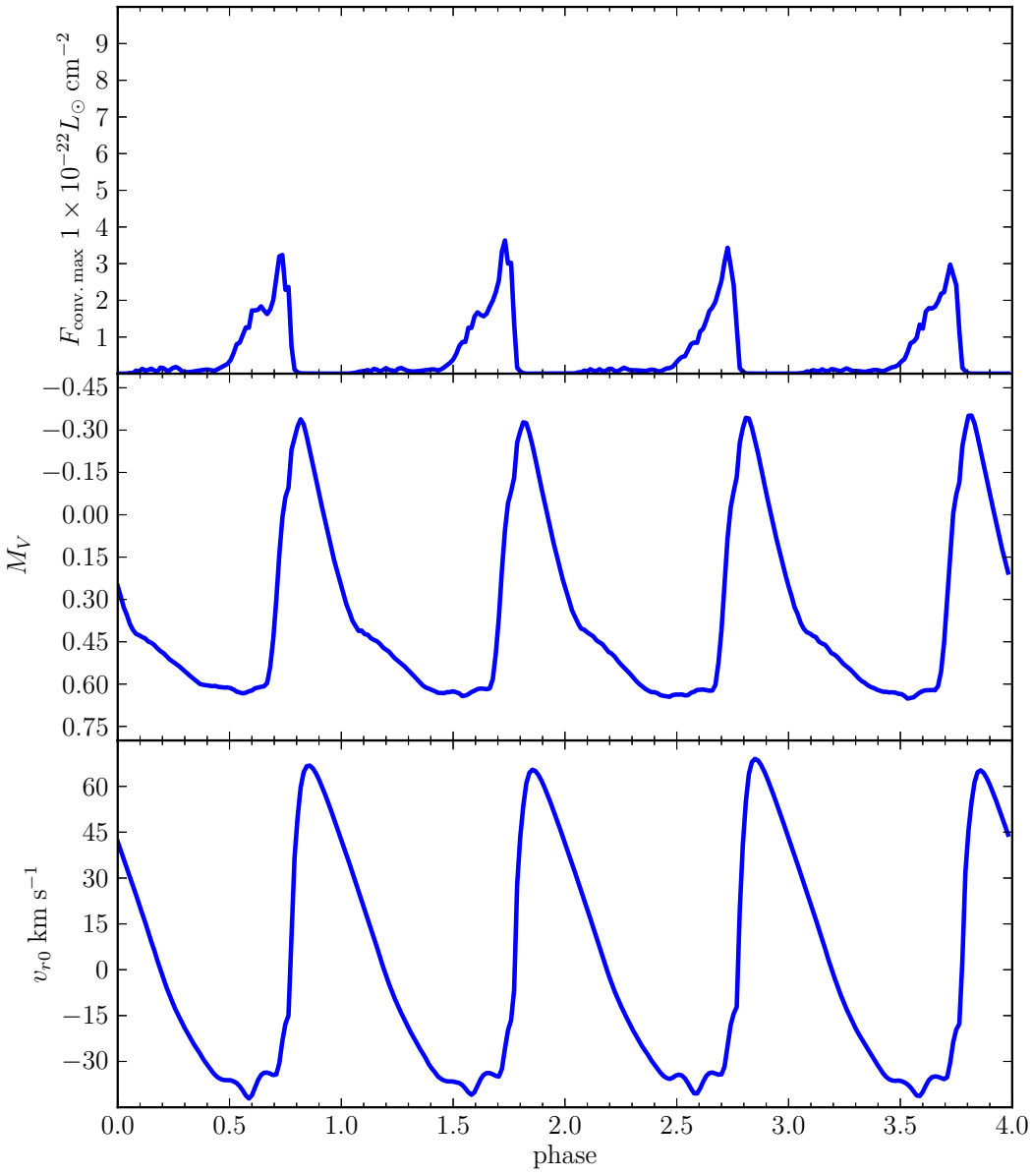

Figure 5.2: Similar to figure 5.1 except for the 6700 K effective temperature model.

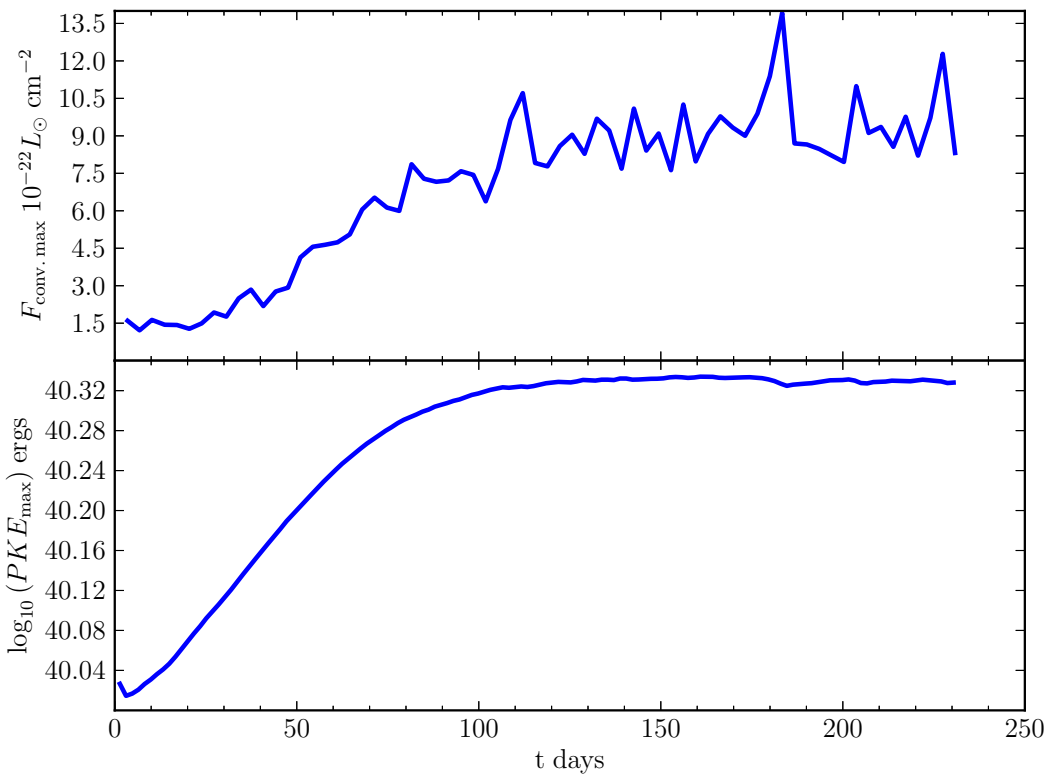

Figure 5.3: Top panel shows the six period average of the peak convective flux for 6500 K model. The bottom panel shows the growth of the log of the peak kinetic energy averaged over three periods.

flux in the mesh, then we find the highest value of this maximum convective flux over a single pulsation period, and finally we compute one point in figure 5.3 by taking the average of the highest values for six consecutive periods. The average in the convective flux is mainly to remove contamination from the first overtone mode, as done in the calculation of the average peak kinetic energies. From Figure 5.3 it is obvious that as the pulsation amplitude increases, so too does the strength of convection. This is possibly a result of the hydrogen ionization zone sweeping through more of the star as the pulsation amplitude increases. Convection can then penetrate deeper and

$T_{\rm eff}$ K	$\eta_{\rm 1D}$	$\eta_{\rm 2D}$	$(\eta_{\rm 1D} - \eta_{\rm 2D})$
6200	2.43	1.27	1.16
6300	2.23	1.15	1.08
6400	1.98	0.98	1.00
6500	1.67	0.74	0.93
6600	0.79	0.30	0.49
6700	0.93	0.32	0.61
6800	0.24	0.04	0.20

Table 5.1: Peak kinetic energy growth rates in % increase per period for 1D fully radiative models, $\eta_{\rm 1D}$, and 2D convective models, $\eta_{\rm 2D}$, and the their difference.

include more mass and thus convection is able to carry more energy. However, the interaction of convection and pulsation is complex and this relationship may be more complex than this simple explanation. The maximum convective flux displayed in figure 5.3 is the maximum throughout the model, occurring in only one radial zone, which is maintained for only a small part of the pulsation cycle (see figure 5.1 or 5.2) and remains very low through the rest of the pulsation cycle.

Growth rates of the peak kinetic energy of pulsation were calculated for all 2D and 1D models and compared in table 5.1. Models used to calculate growth rates were all initiated at the same surface radial velocity of 10 km s^{-1}. The 1D models given in this table were computed to match the 2D models in all respects except the 1D models are fully radiative while the 2D models allow hydrodynamic convection. As the effective temperature becomes cooler the difference in growth rates between the fully radiative 1D models and the 2D convective models becomes larger.

We had hoped to clearly show that convection quenches pulsation at the red edge of the instability strip by noting a decrease in the peak kinetic energy (negative

growth rate) of models cooler than some temperature. However, as the models became cooler convection became stronger, and eventually the convectively unstable region penetrated well below the hydrogen and helium ionization regions. Once this happened there was a net change in the global model structure and hence in the potential energy of the model. This change in potential energy would require a large amount of time (at least relative to the times covered by these simulations) to return the model to some sort of equilibrium underlying the pulsation. This adjustment significantly affects the use of the peak kinetic energy as a measurement of the growth or decay of a pulsation mode. The 6200 K model did not reach full amplitude before the convectively unstable region penetrated below the ionization zones. The 6300 K model appeared to be at nearly full amplitude just before the convection penetrated below the ionization zones, as the growth of the peak kinetic energy of the pulsation mode had slowed considerably. Models with effective temperatures 6400 K and hotter reached full amplitude modes.

5.2 Full amplitude Solutions

One of the major goals of this work is to be able to compute full amplitude radial pulsations of RR Lyrae stars. Previous work by Deupree was unable to reach full amplitude because his choice for moving the radial grid coordinate. We have removed this difficulty by using a radial grid velocity defined to maintain shells of constant mass (see section 2.2.3 for details of this algorithm). Most of the models mentioned in

Model	$T_{\rm teff}$ K	L $L_\odot$	M $M_\odot$	P hr	A_V	Mode
T6300	6300	50	0.7	15.09	0.56	RRab
T6400	6400	50	0.7	14.32	0.64	RRab
T6500	6500	50	0.7	13.57	0.75	RRab
T6600	6600	50	0.7	12.89	0.83	RRab
T6700	6700	50	0.7	12.24	1.01	RRab
T6800	6800	50	0.7	11.63	0.79*	RRab
T6900	6900	50	0.7	8.26	0.51	RRc

Table 5.2: Parameters of 2D models. *This is a lower bound for A_V as the 6800 K model has not yet reached full amplitude.

the previous section have reached full amplitude fundamental mode pulsations after being initiated with the linear eigenfunction mode scaled to have surface velocities of either 10 km s^{-1} or 20 km s^{-1}. Models that reached full amplitude are given in table 5.2.

Models hotter than 6400 K were initiated with the 20 km s^{-1} surface pulsation velocity while models at temperatures of 6400 K and cooler were initiated at the 10 km s^{-1} surface velocity. The higher initial radial pulsation velocity was chosen because it shortened the time required to reach full amplitude, and was required by hotter models to remain pulsating in the fundamental mode. If hotter models, closer to the fundamental blue edge (6600 K and hotter), are initiated at the lower velocity their pulsation amplitude decays and eventually the pulsation mode switches into the first overtone pulsation mode. If they are instead initiated with a higher radial velocity amplitude the pulsation amplitude grows until full amplitude is reached in the fundamental mode. This was illustrated in the 1D models in chapter 4 and is also seen in the 2D simulations.

Even when initiated with a surface pulsation velocity of 20 km s^{-1} the pulsation

amplitude of the 6900 K model decayed, and presumably it would eventually switch to the first overtone mode. At 10 km s^{-1} the pulsation amplitude also decayed and the pulsation mode switched to the first overtone mode and remained at full amplitude. The 6900 K model referenced in table 5.2 was initialized with the linear fundamental eigenfunction mode scaled to a surface velocity of 5km s^{-1}. The mode slowly switched from the fundamental mode to the first overtone as the pulsation amplitude grew until it reached full amplitude in the first overtone mode.

Models cooler than 6500 K were initiated at the lower velocity to ensure that their pulsation amplitude would grow to the full amplitude rather than decay from higher amplitude to their equilibrium pulsation amplitude or full amplitude. If started at a pulsation amplitude higher than the equilibrium pulsation amplitude the assumption of a linear eigenfunction for the mode is less valid, and contamination from other modes is more of a concern. An example of the growth of $\log_{10}$(PKE) with time is shown in figure 5.4 for a 2D convective model along with a 1D fully radiative model with otherwise similar model parameters, both with an effective temperature of 6500 K. It is clear that convection limits the amplitude of pulsation as compared to the fully radiative models.

The main reason for computing full amplitude radial pulsations is to compare computed model results with observations. To this end we have computed visual light curves from model absolute bolometric magnitude light curves using a table of bolometric corrections as functions of $\log_{10} g$ and $T_{\rm eff}$ from Bessell et al. (1998)

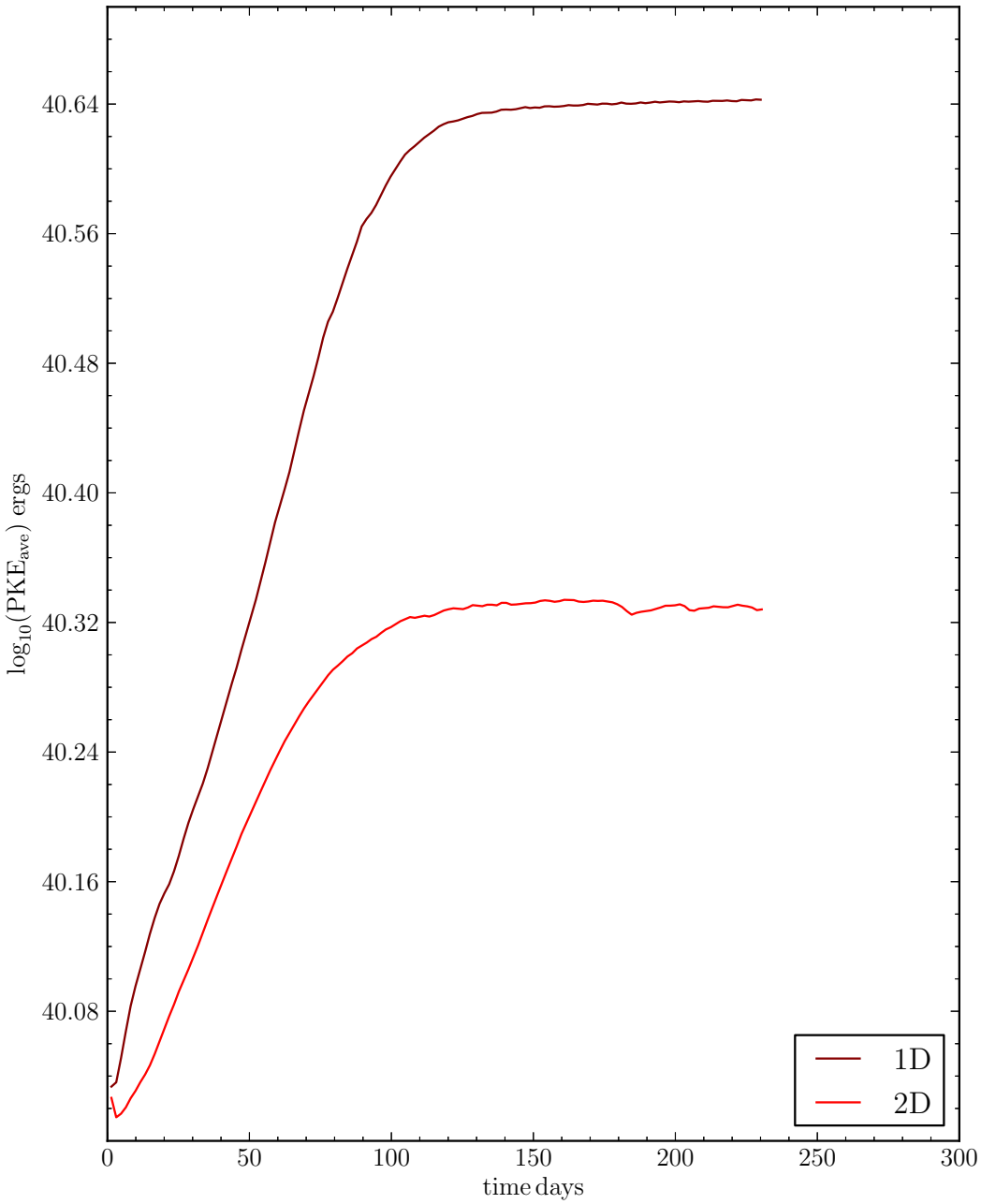

Figure 5.4: A comparison of 1D fully radiative and 2D convective model peak kinetic energies for 6500 K models.

model atmospheres. The model's absolute bolometric magnitudes are converted to the absolute visual magnitude at each individual point in the light curve by linearly interpolating in the table of bolometric corrections to the effective temperature and gravity of the model at that point in the light curve. This effectively assumes that the bolometric correction in the pulsating model is the same as in a static model at the same effective temperature and gravity. Applying the bolometric correction acts to increase the amplitude of the visual light curve over the bolometric light curve, as the bolometric correction is largest at maximum light, and smallest at minimum light, which was also found by Kovacs & Kanbur (1998) (see their figure 3). We have not included the acceleration from the surface velocity, as it occasionally leads to unrealistic values of the effective gravity. We have checked the difference between including and not including this acceleration in cases where it does not result in unrealistic effective gravities, and omitting it does not substantially affect the results. Kovacs & Kanbur have shown that the error introduced by neglecting even the variation of the effective gravity with pulsation phase is negligible as the effective temperature plays the largest role in determining the variation of the bolometric correction over a pulsation cycle.

We have computed a number of synthetic visual light curves. The 2D models provide absolute bolometric magnitudes at regularly spaced time intervals of 600 seconds, as this is when we take model dumps. We then applied bolometric corrections to these absolute bolometric magnitudes over approximately seven pulsation cycles

Star	$T_{\rm eff}$ K	L $L_\odot$	M $M_\odot$	P hr	A_V	Mode	Model Matched
v120	6300	49.9	0.68	15.36	0.44	RRab	T6300
v19	6266	49.3	0.70	15.17	0.45	RRab	T6300
v48	6283	58.7	0.67	15.07	0.61	RRab	T6400
v93	6446	50.2	0.67	14.46	0.73	RRab	T6500
v10	6469	51.4	0.73	13.67	0.88	RRab	T6600
v92	6712	49.9	0.71	12.07	1.14	RRab	T6700
v125	6829	49.4	0.71	8.40	0.41	RRc	T6900

Table 5.3: Parameters of choice M 3 variables as given in Cacciari et al. (2005) and the models for which they are the best match.

at full amplitude. We have then phased these regularly spaced absolute bolometric magnitudes in a manner similar to that done for observed light curves. This produces a number of points from the seven different cycles of pulsation all overlaid on the same cycle of pulsation. The vertical spread of light curve points indicates the extent of variation of the light curve over the selected cycles. Figures 5.5-5.11 show these synthetic light curves as compared to observational light curves of selected RR Lyrae variables from M 3 listed in table 5.3. Also shown are the magnitude differences between the averaged observed light curves and the simulated curves. The horizontal lines denote difference of 0 and ± 0.05 magnitudes. This range was chosen to match the best fits by Marconi & Degl'Innocenti (2007). The other range they used was ± 0.08 magnitudes, also shown has horizontal lines in the figures. The estimated observational errors are ± 0.02 magnitudes (Cacciari et al., 2005). A first glance at these figures reveals that the cooler rmodels, in which convection is more pronounced, actually match the observed light curves better than the hotter models. The 2D hotter models match the light curves approximately as well as do those of Marconi & Degl'Innocenti (2007), while cooler models match the observed light curves much

more closely than do the 1D light curves.

The variables in table 5.3 were selected from 89 observed light curves provided by Cacciari et al. (2005) of both RRab and RRc variables and phased. The phased light curves were then duplicated for a second cycle for easier visual comparison with the model light curves. These variables were selected by comparing the individual model light curves directly to all the observed variable light curves and selecting the best match as determined from a Bayesian analysis conducted by Michael Gruberbaurer considering only the light curve shapes and no model parameters (see Gruberbauer et al. (2012) for a discussion of this technique with application to fitting solar oscillation modes and Gregory (2005) for a general introduction to Bayesian analysis). To accomplish the fits only two free parameters were allowed, the distance modulus, and a phase shift, and the parameter space was sampled using nested sampling (e.g., Feroz et al., 2009). All variables in table 5.3 were chosen as best matches to the models except v120, which was chosen to compare with a fit by Marconi & Degl'Innocenti (2007) to the same observed light curve with their 1D convective models. We selected only the best matches in order to help compensate for the fact that we are not adjusting any model free parameters. In comparing their figure 17 to our figure 5.5, one can see that our approach to modeling convection produces a significantly better reproduction of the observed light curve for v120. We have not adjusted any of the free parameters (luminosity, mass or effective temperature) and merely chose representative values of the variable stars in M 3 as a whole. While covering this

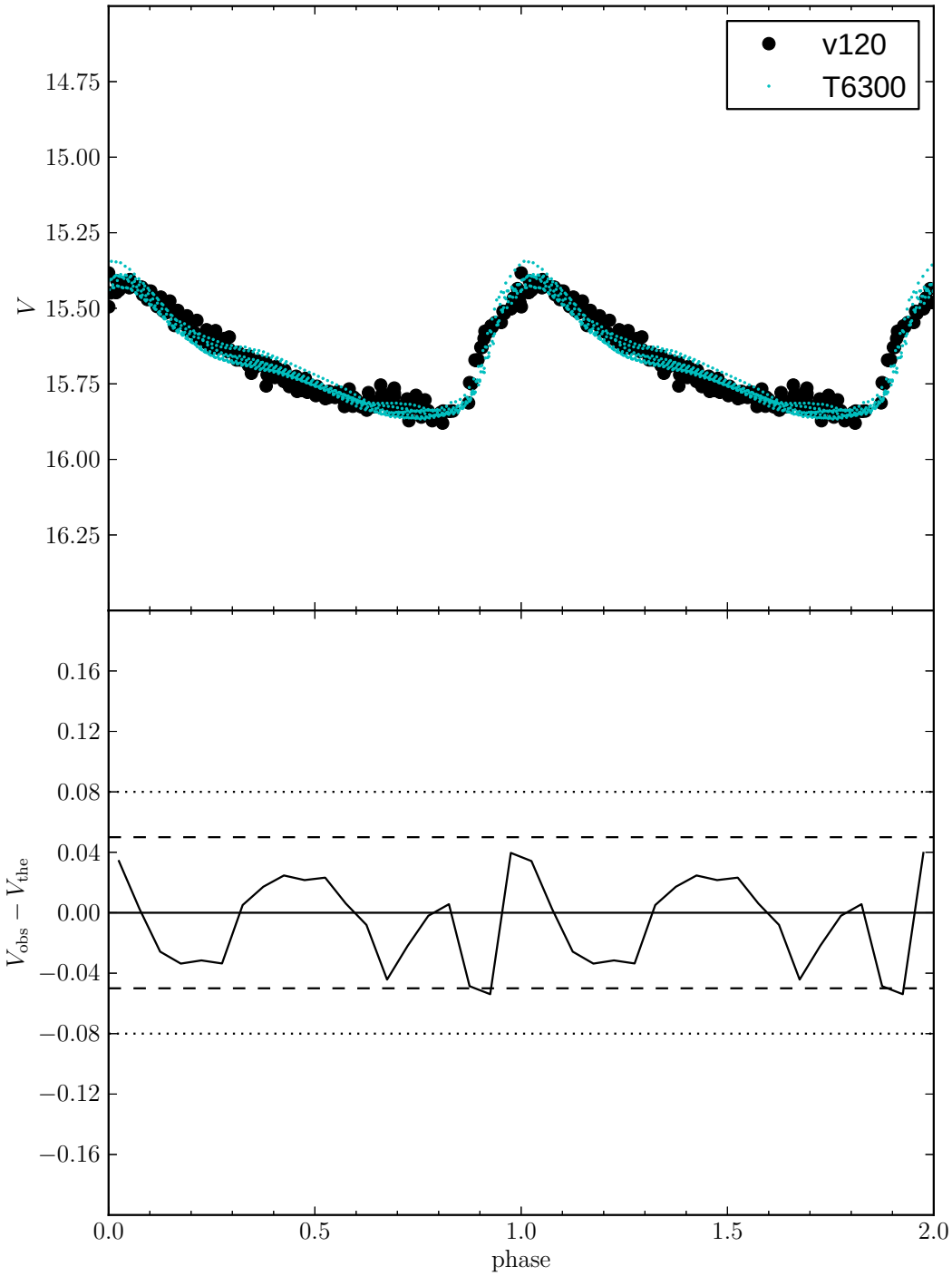

Figure 5.5: 6300 K effective temperature model's light curve compared to variable star v120's light curve using a distance modulus of 15.34.

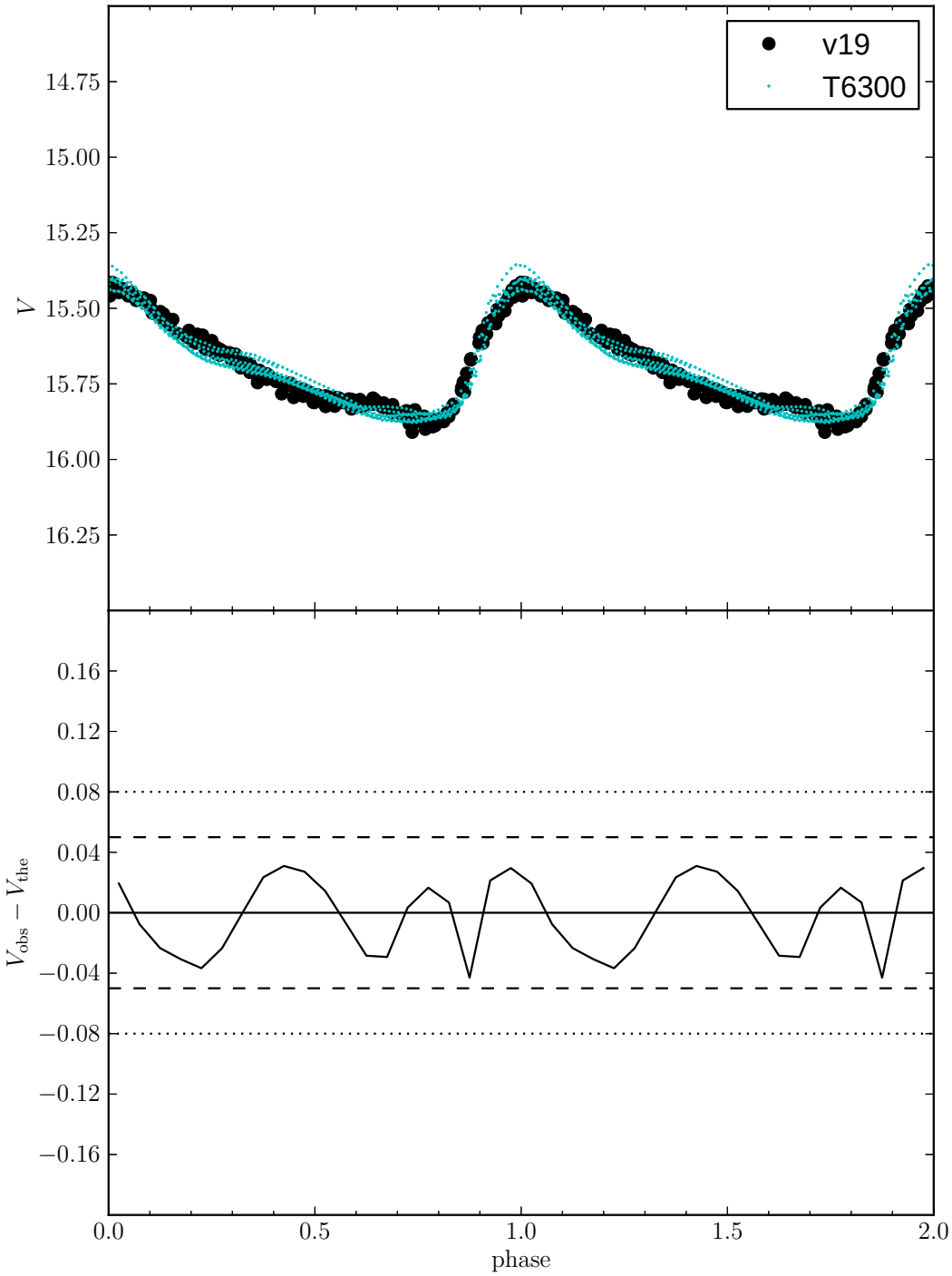

Figure 5.6: 6300 K effective temperature model's light curve compared to variable star v19's light curve using a distance modulus of 15.35.

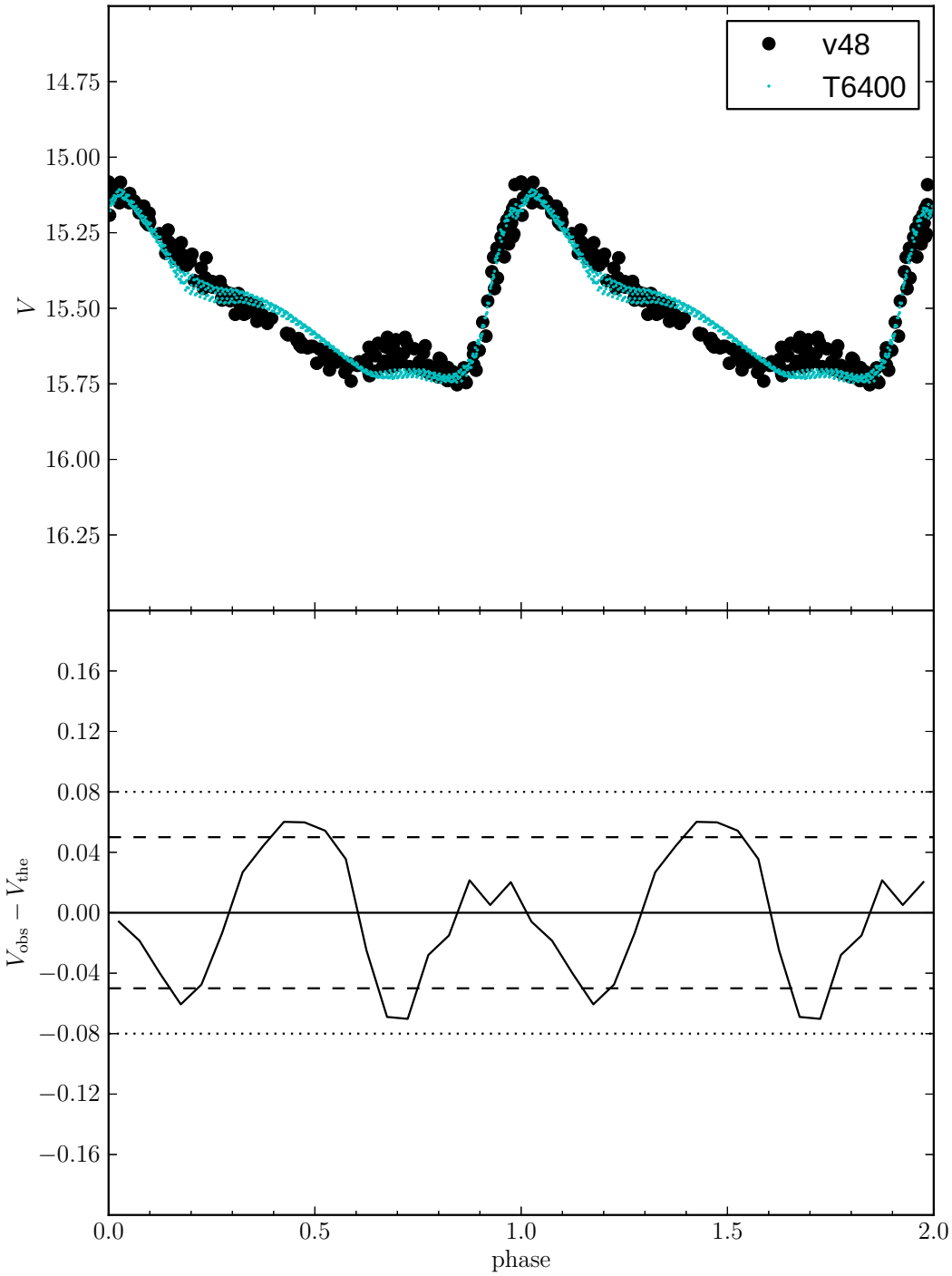

Figure 5.7: 6400 K effective temperature model's light curve compared to variable star v48's light curve using a distance modulus of 15.16.

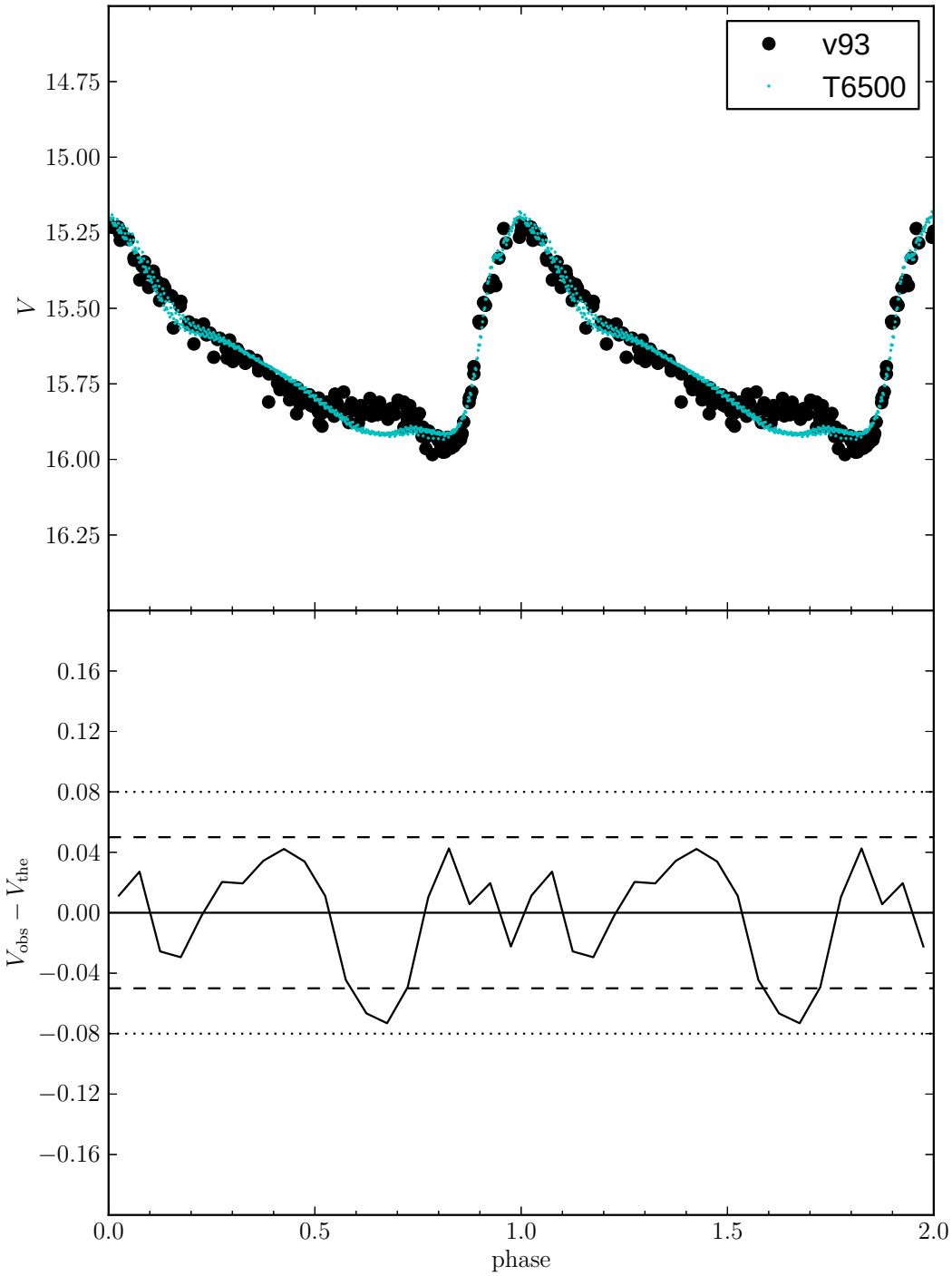

Figure 5.8: 6500 K effective temperature model's light curve compared to variable star v93's light curve using a distance modulus of 15.32.

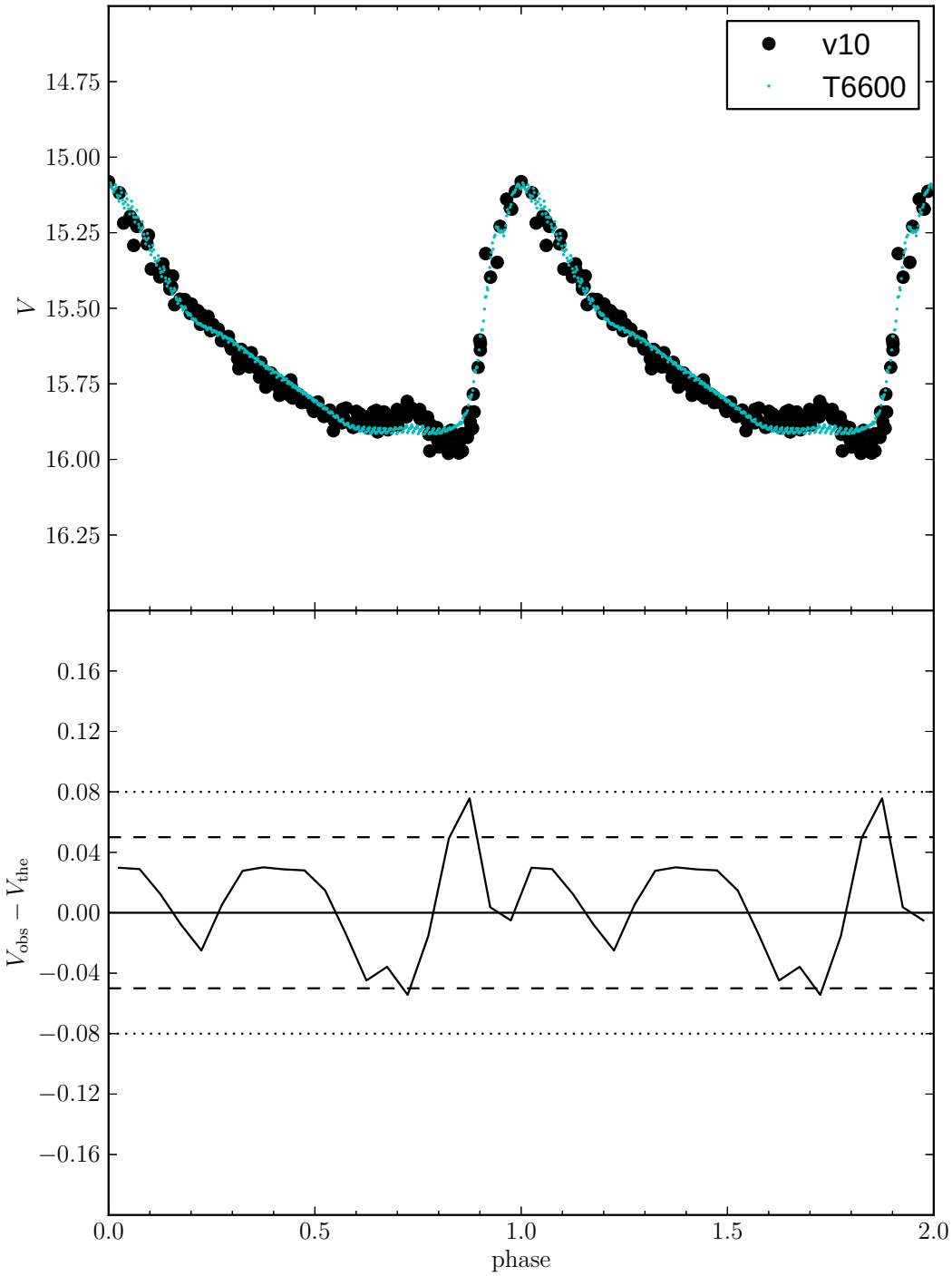

Figure 5.9: 6600 K effective temperature model's light curve compared to variable star v10's light curve using a distance modulus of 15.27.

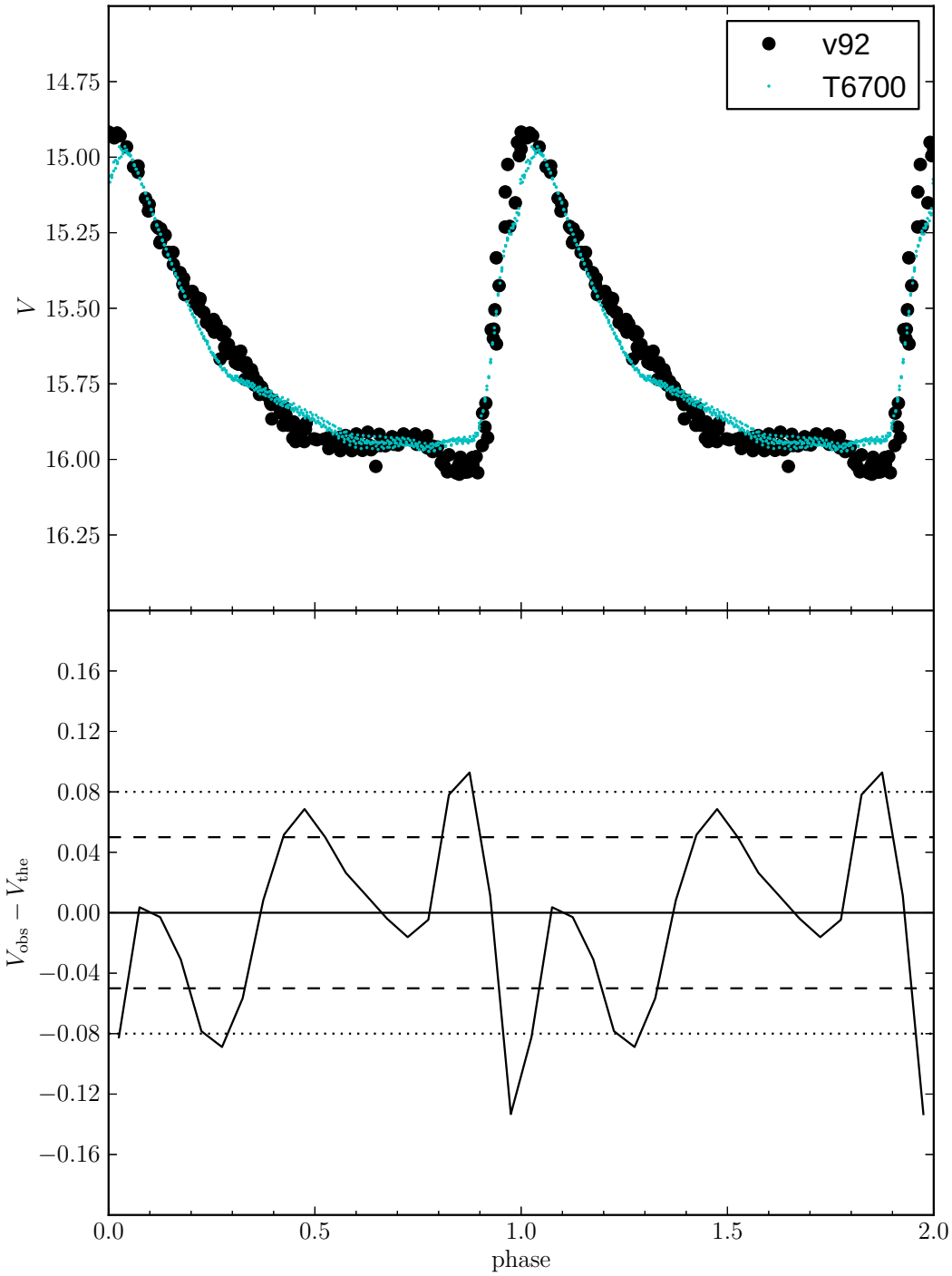

Figure 5.10: 6700 K effective temperature model's light curve compared to variable star v92's light curve using a distance modulus of 15.32.

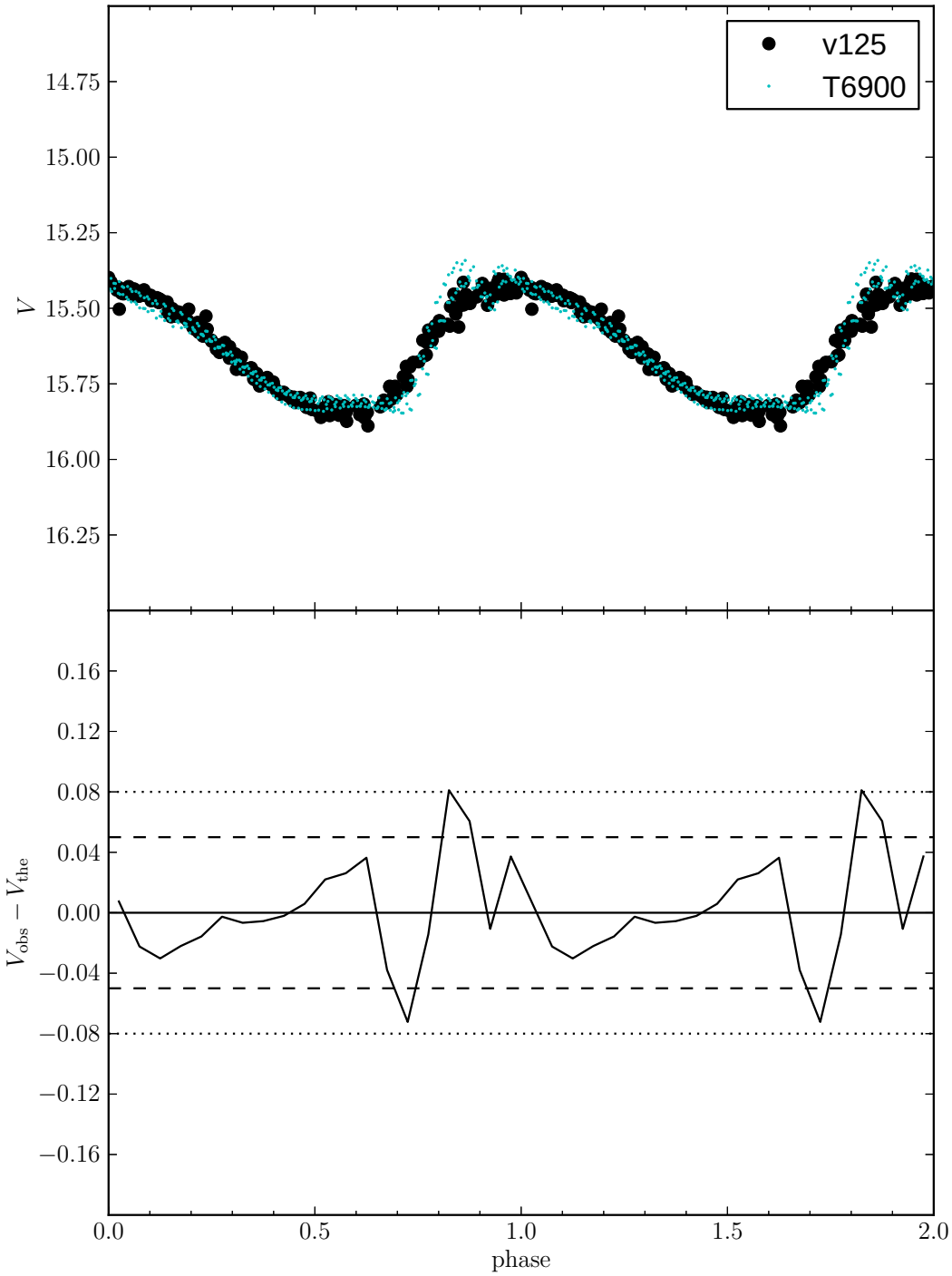

Figure 5.11: 6900 K effective temperature model's light curve compared to variable star v125's light curve using a distance modulus of 15.32.

parameter space would be desirable, the computational requirements of our method together with time constraints place this beyond the scope of the current work.

Particularly good fits are achieved for the cooler models, 6300 K and 6400 K (figures 5.6 and 5.7 respectively). Hotter models are reasonably good fits given that we have not tuned any of the model parameters to match the observed light curves. There are some features of the light curves that are not matched as well as one might like. In particular model T6700 fit to variable v92 (figure 5.10) does not reproduce the dip at minimum light, or get the slope during descending light quite correct. However, adjusting model parameters may be able to account for at least some of the discrepancy. In figure 5.11 we have compared our 6900 K first overtone model with that of v125 and find fairly good agreement. However, the model light curve shows a slightly less sinusoidal shape than the observed light curve. As one can note from the residuals of the light curve plots all models, except the T6700 model are within the larger best fit extrema of 1D light curves from Marconi & Degl'Innocenti ($\pm$0.08 mag) and the cooler models match even to within Marconi & Degl'Innocenti's best fit light curves of $\pm$0.05 mag.

In addition to comparing light curves with observations we can also compare pulsation amplitude as a function of effective temperature with that derived from observations. Figure 5.12 shows the observed visual pulsation amplitudes for fundamental pulsators (open circles) and first overtone pulsators (open squares) as compared to our model predictions for fundamental (blue filled circles and solid lines) and first

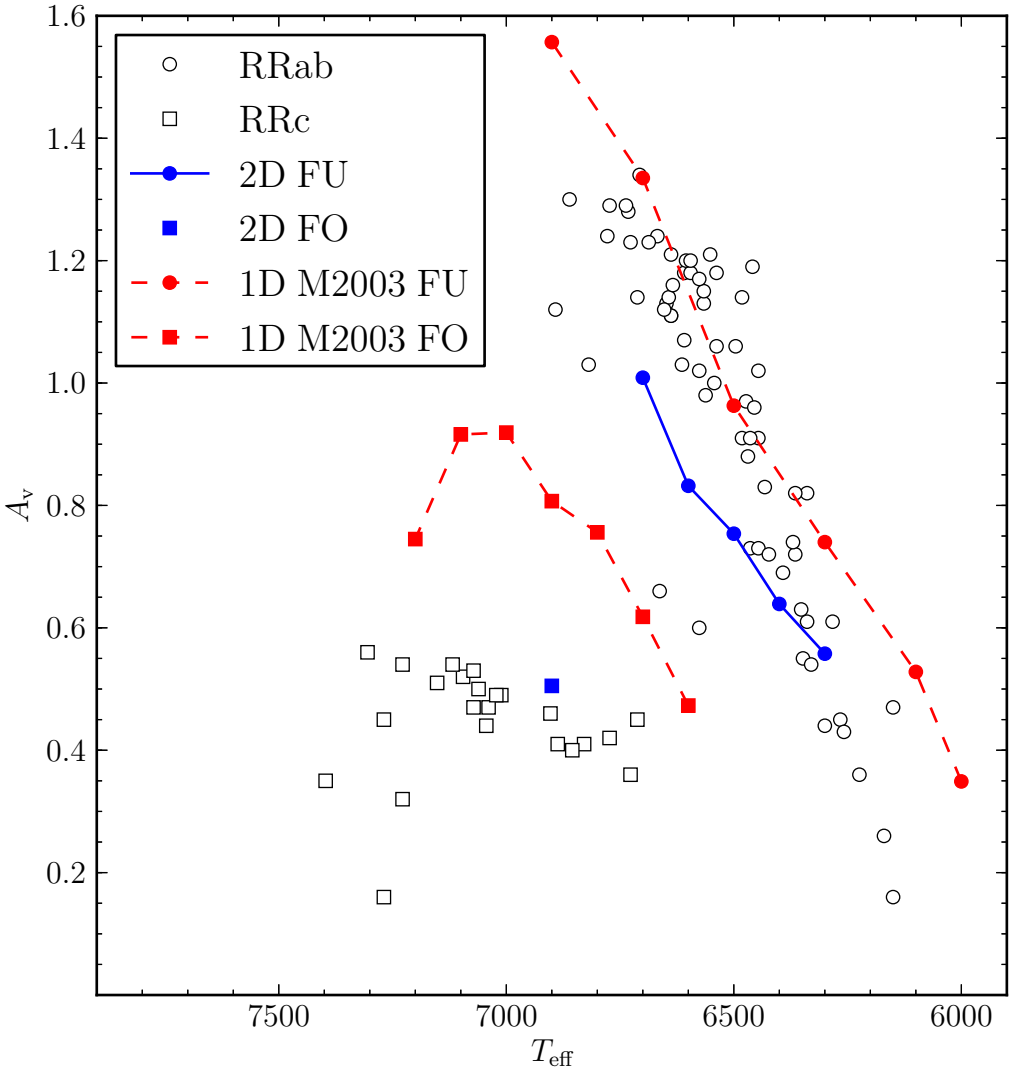

Figure 5.12: Visual pulsation amplitude, A_V across the RR Lyrae instability strip. Circles and squares denote data points for the fundamental and first overtone modes respectively. Filled symbols correspond to models, while open symbols correspond to observations. Blue symbols with solid lines are for our 2D convective calculations, and red symbols with dashed lines are for 1D convective models of Marconi et al. (2003).

overtone (filled blue squares) modes. This figure also contains results from 1D convective models by Marconi et al. (2003) for the fundamental (filled red circles with dashed line) and first overtone (filled red squares dashed line) modes. The 1D convective models were for a mass of 0.65 $M_{\odot}$, Z=0.001, and $\log_{10}(L/L_{\odot}) = 1.61$, while our models were for a mass of 0.7 $M_{\odot}$, a metallicity of Z=0.0005, and a luminosity of $\log_{10}(L/L_{\odot}) = 1.7$. At least some of the differences between our visual amplitudes and those of Marconi et al. result from the differences in mass and luminosity, and to a lesser extent metallicity. Figure 10 of Bono et al. (1997b) shows that as the mass is increased in their 1D convective models, the amplitude of the first overtone mode increases for a given effective temperature. This effect is less clear for the fundamental mode. Bono et al.'s figures 9 and 10 show that as the luminosity is increased the pulsation amplitude of the fundamental mode increases. In the case of the first overtone pulsators however, as the luminosity is increased the pulsation amplitude decreases and the characteristic "bell" shape flattens. Based on the trends mentioned for the pulsation amplitude from Bono et al. (1997b) one might expect that 1D models for the same luminosity and mass as our models would have a flatter "bell" shape for the first overtone mode models, and perhaps a slightly larger amplitude for the fundamental mode. Both our calculations and the 1D calculations of Marconi et al. produce similar slopes, for the relation between the visual amplitude of the fundamental mode as a function of effective temperature. However, to make direct comparison between the 2D and 1D calculations models would need to be calculated for the same set of

model parameters.

To complicate things further, in addition to the mass, luminosity and metallicity, the helium abundance can also play a role in determining the amplitude of the pulsation, though less substantially than the mass or luminosity (see Bono et al., 1997b, figure 9). Finally the pulsation amplitude in 1D models is also influenced by the choice for the mixing length parameter (see Marconi et al., 2003, figure 14) the correct choice of which may vary for different models based on many different variables such as the pulsation mode and the effective temperature. Given these considerations, we would argue that we have done well in matching the observed visual amplitude dependence on the effective temperature, and perhaps some adjustment of our free parameters of mass and luminosity and composition would give an even better match in individual cases.

The good agreement between the observed and model light curves as well as the good agreement between the observed and model visual amplitude dependence on the effective temperature indicate that our use of 2D convective radial pulsation models using large eddy simulations produce light curves that match those of real RR Lyrae stars reasonably well. One should note that this does not necessarily mean that we have a great model for turbulent convection. It is possible, even likely, that the time dependent behavior of the convective flux shown in figures 5.1 and 5.2 is a key component in determining the effect of convection on pulsation, and this behavior may result with an approach to convection which need not be correct in every detail.

5.3 Model Structure with Convection Only

While the emphasis of this research is on the interaction between convection and stellar pulsation, we can also compute the horizontally averaged structure of a model which is not pulsating. This structure will still retain some time dependence because it is a hydrodynamic calculation, but the variation is relatively slight over the 40 day time period between the time when convection had grown large enough to begin affecting the structure to when pulsation, as indicated by periodic variation of the stellar radius, began to affect the structure. We have performed such calculations for models with effective temperatures of 6300 K and 6700 K. The results are presented in Figure 5.13 in the form of the logarithmic derivative of the horizontally averaged temperature with respect to the horizontally averaged pressure versus the horizontally averaged temperature. We have included the structure of both the initial radiation only model and a model when the changes in the structure due to convection appear to be rather stable. The decrease in the gradient in the hydrogen and first helium ionization regions when convection is included is clear. Furthermore, there are some differences in the gradient from that of the radiation only models up to temperatures of about 3×10^4 K. The effects are larger for the cooler model, as would be expected.

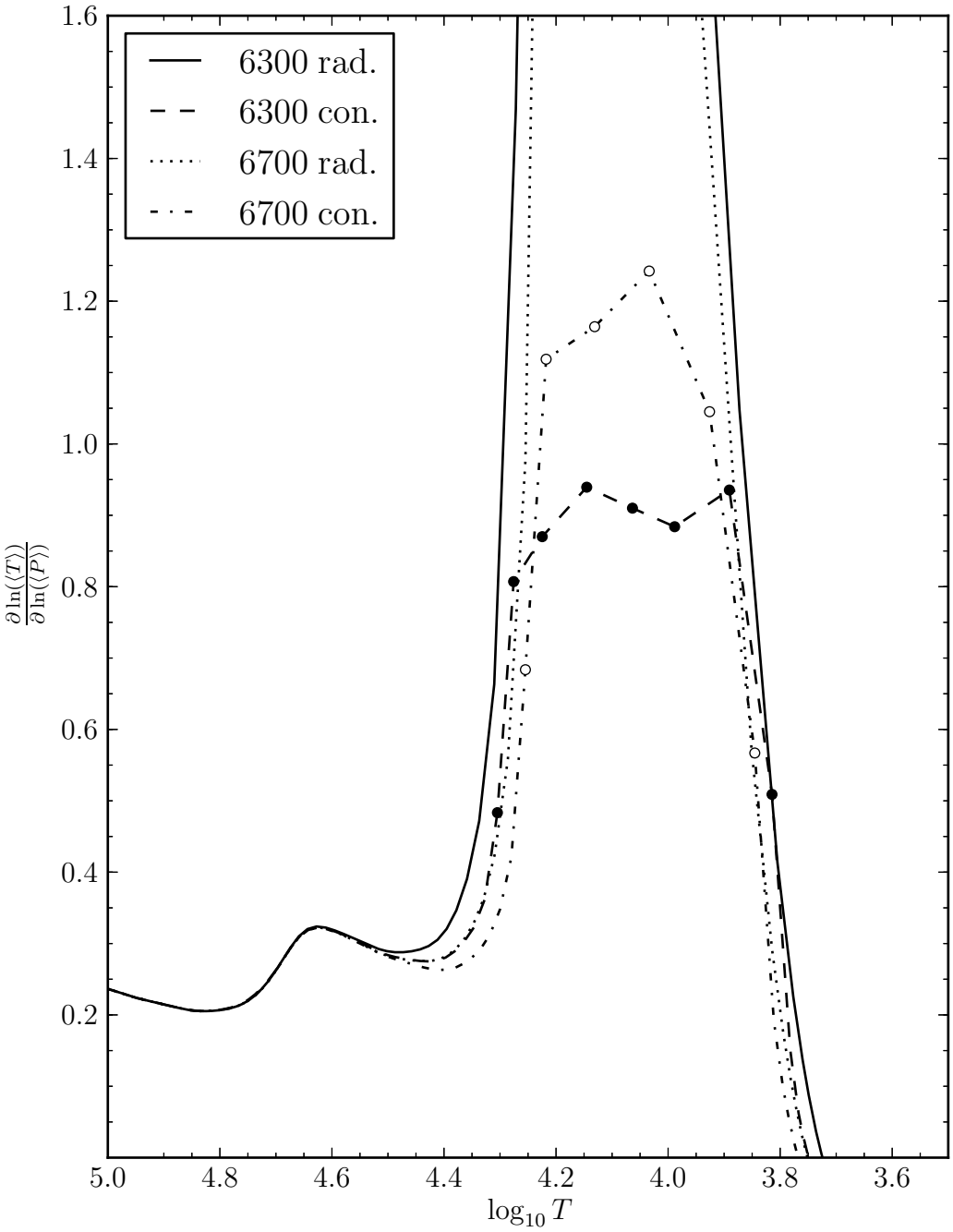

Figure 5.13: Logarithmic gradient of the horizontally averaged temperature with respect to the horizontally averaged pressure versus the horizontally temperature. Four models are represented: $T_{\rm eff} = 6300$ K, radiation only (solid), $T_{\rm eff} = 6700$ K, radiation only (dotted), $T_{\rm eff} = 6300$ K with convection (dash), and $T_{\rm eff} = 6700$ K with convection (dash-dot). The locations of some discrete points have been added for clarity.

6 3D Models

We have computed simulations of RR Lyrae pulsation with 3D convection at effective temperatures of 6200, 6300, 6400, 6500, 6700, and 6900 K. The initial parameters of these models match their 2D counterparts discussed in the previous chapter except that they have an extra dimension for fluid flow. Given the highly turbulent nature of convection in the surface ionization regions of RR Lyrae stars, the convective motion should be three dimensional. These 3D simulations have the same θ-zoning as the 2D calculations but have 20 ϕ zones also covering 6^o, producing a 3D version of a pie slice subtending 36 square degrees. The choice of 6^o coverage in each direction comes from relatively short 3D simulations with angular zoning which subtended total angles from $2^o \times 2^o$ to $10^o \times 10^o$ with both θ and ϕ stepping simultaneously in increments of 2^o between the two extremes. These short simulations were for a 5700 K effective temperature model with strong convection and were carried out until convection had finished growing from machine round off errors and at least two additional pulsation cycles had been completed. The $6^o \times 6^o$ configuration was found to be a good compromise between including multiple convective cells, and the best resolution. The 6^o simulation was the smallest angular converge for which we found more than one distinct convective cell. We have performed short 3D simulations with the number of θ and ϕ zones of 5×5 up to zonings of 40×40. Simulations with the largest number of angular zones had very large computational requirements and the amount

of computational time required to reach full amplitude would have been prohibitively long. As a compromise we chose 20 θ and 20 ϕ zones, which was still quite computationally demanding (for example, most of these calculations require several months) when considering the number of time steps required for full amplitude solutions. Currently none of the 3D simulations have reached the full amplitude solution, though the 6300 K effective temperature simulation appears to be getting close.

We also examined how the choice of radial zoning affects the growth of the peak kinetic energy, finding little difference between 140 radial zone models versus 310 zone models. Thus we have opted to use 140 radial zones for all our calculations as it reduces our computational requirements both in number of zones to compute, and from the larger timestep resulting from the larger radial zones.

6.1 Differences Between 2D and 3D Convective Flow Patterns

Figure 6.1 shows the top 16% by radius of the 6300 K effective temperature 2D simulation. The color shows the temperature of the material and the vectors show the convective velocity. The white lines show the horizontal periodic boundaries. Figure 6.2 is similar to figure 6.1 but shows a slice through the comparable 3D simulation. The convective flow pattern of the 2D simulation at first glance appears similar to a slice through a comparable 3D simulation. However, there are some differences

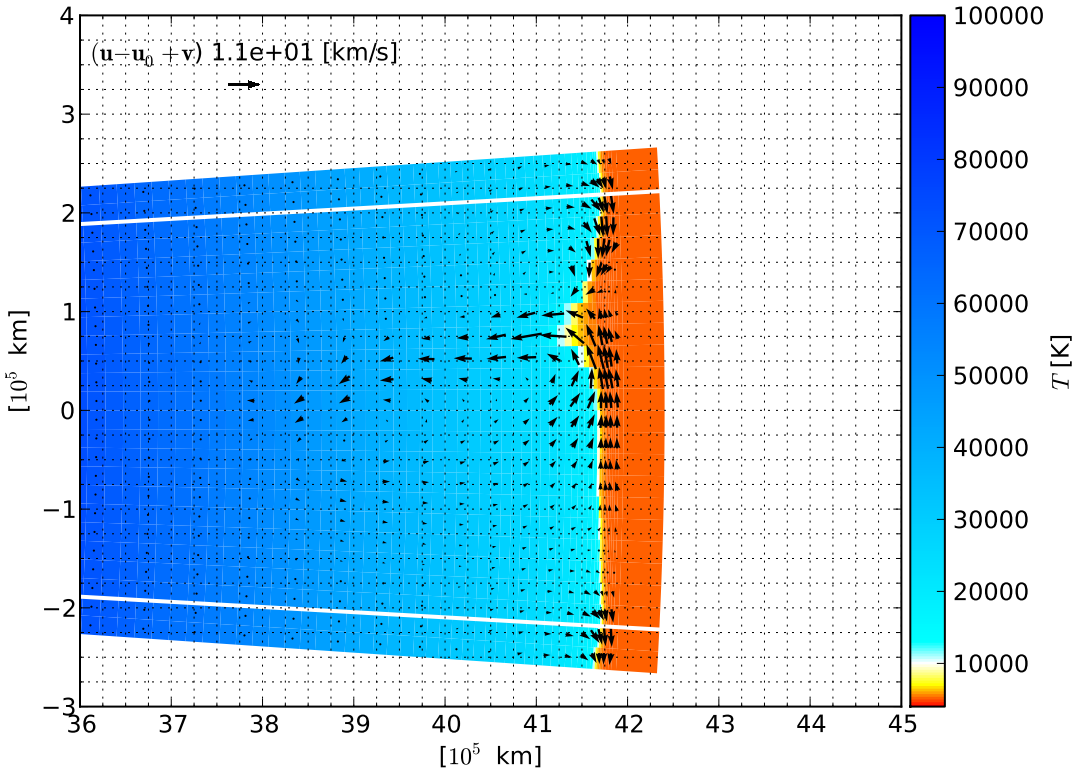

Figure 6.1: Shown is only the upper 16% by radius of the 2D simulation of a 6300 K effective temperature RR Lyrae, while 90% by radius of the star is actually simulated. Color scale shows the temperature of the material, while the vectors show the combined r and θ convective velocity components. This plot is at a phase of pulsation half way between full compression and full expansion.

in the flow pattern. In particular the circular flow pattern clearly visible in the 2D simulation is not as noticeable in the slice through the 3D simulation. This may be a result of the fact that the extra dimension allows some of the return flow to take place in a different plane.

While figure 6.2 provides information about how the 3D convective flow pattern behaves in the radial and θ directions, it is informative to see the flow pattern in the

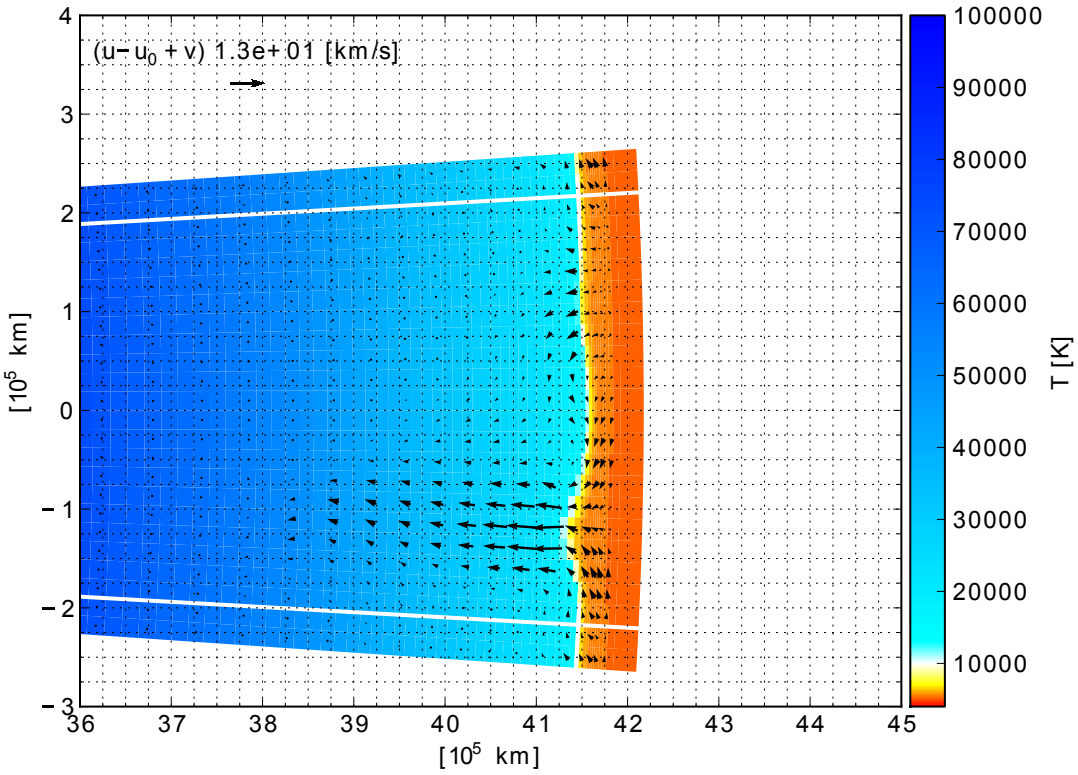

Figure 6.2: Similar to figure 6.1 except that it is an r-θ slice through the 6300 K effective temperature 3D simulation.

horizontal directions. Figures 6.3 and 6.4 show a temperature isosurface spanning the full horizontal extent of the 6300 K effective temperature 3D simulation during compression and expansion phases, respectively. One can see that the convection truly is 3D in nature. The reduction in convective strength from compression to expansion is clear, with larger velocity vectors and larger variations in the temperature isosurface showing stronger convective flows during compression and smaller velocity vectors and a flatter temperature isosurface during expansion. Figures 6.5 and 6.6 are the same as figures 6.3 and 6.4 except for the 6700 K effective temperature model. Comparing

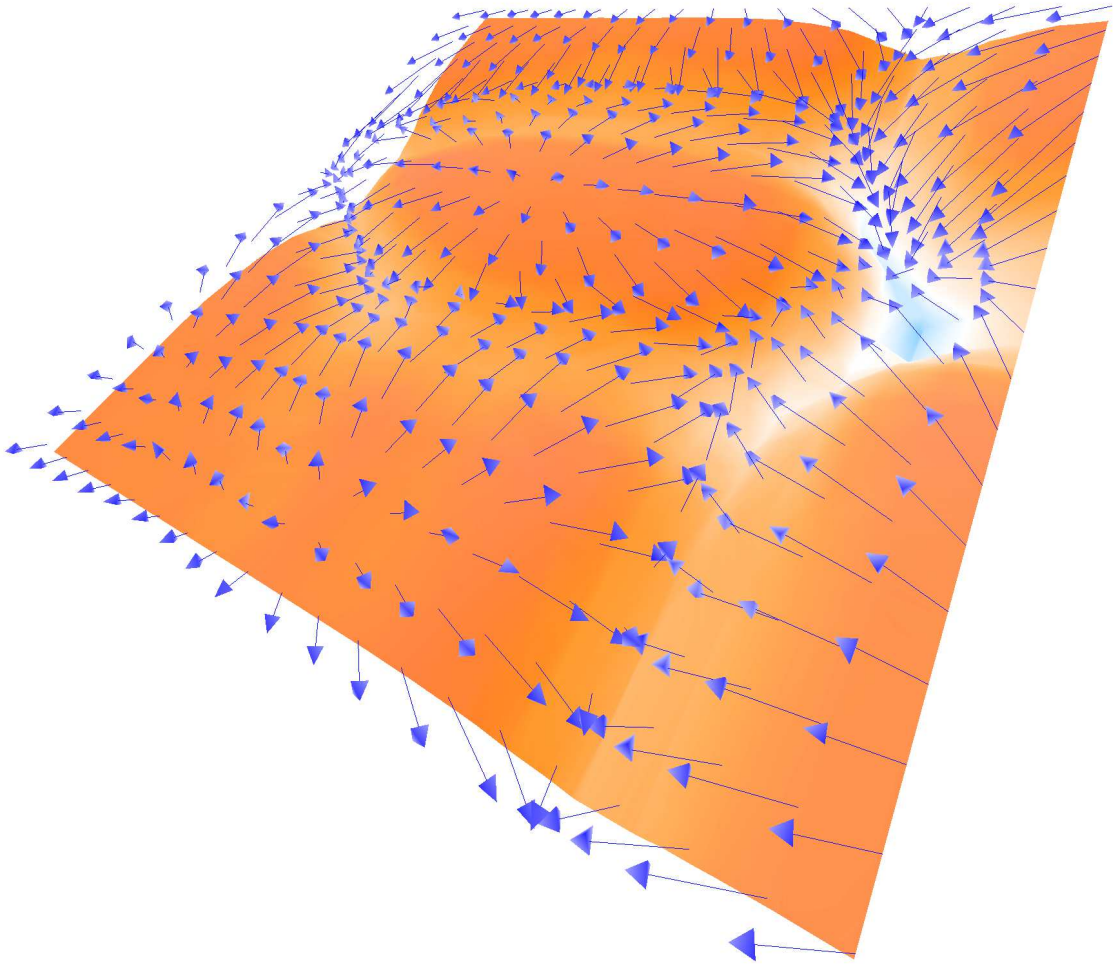

Figure 6.3: Plotted is a temperature isosurface at 1×10^4 K with the color scale indicates the radial convective velocity, with red indicating upward velocities, and blue indicating downward velocities. The vectors indicate the total convective velocity (radial and both horizontal components) in a horizontal slice above the isosurface. This is for the 6300 K effective temperature simulation during radial compression.

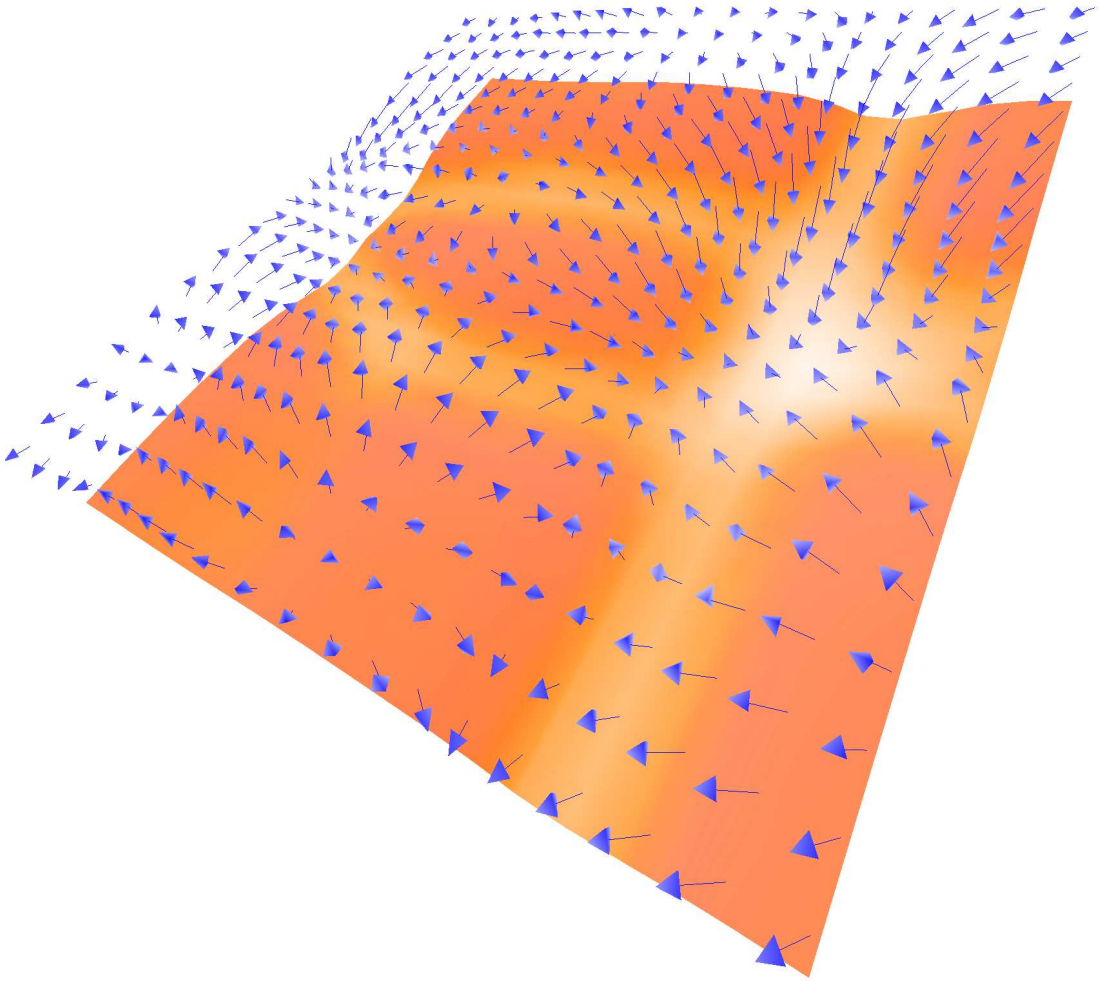

Figure 6.4: Similar to figure 6.3 except during radial expansion.

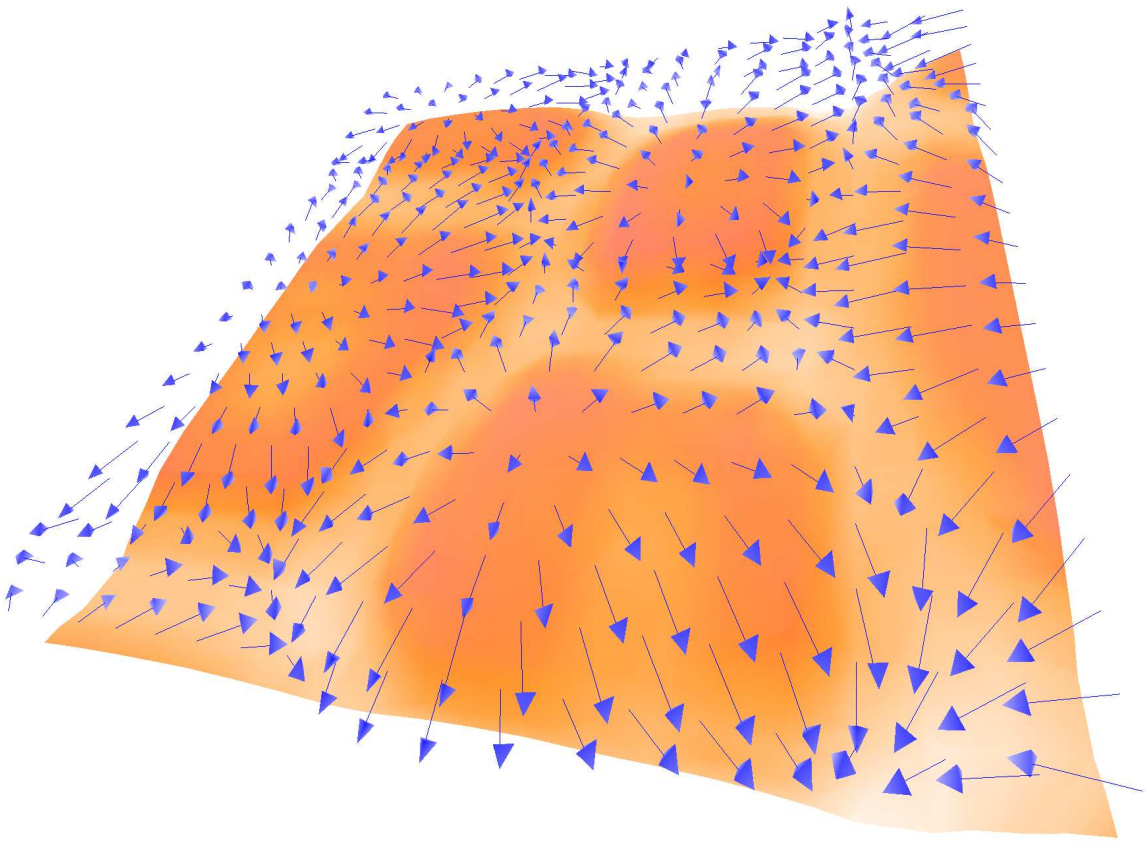

Figure 6.5: Similar to figure 6.3 except for the 6700 K effective temperature simulation during radial compression.

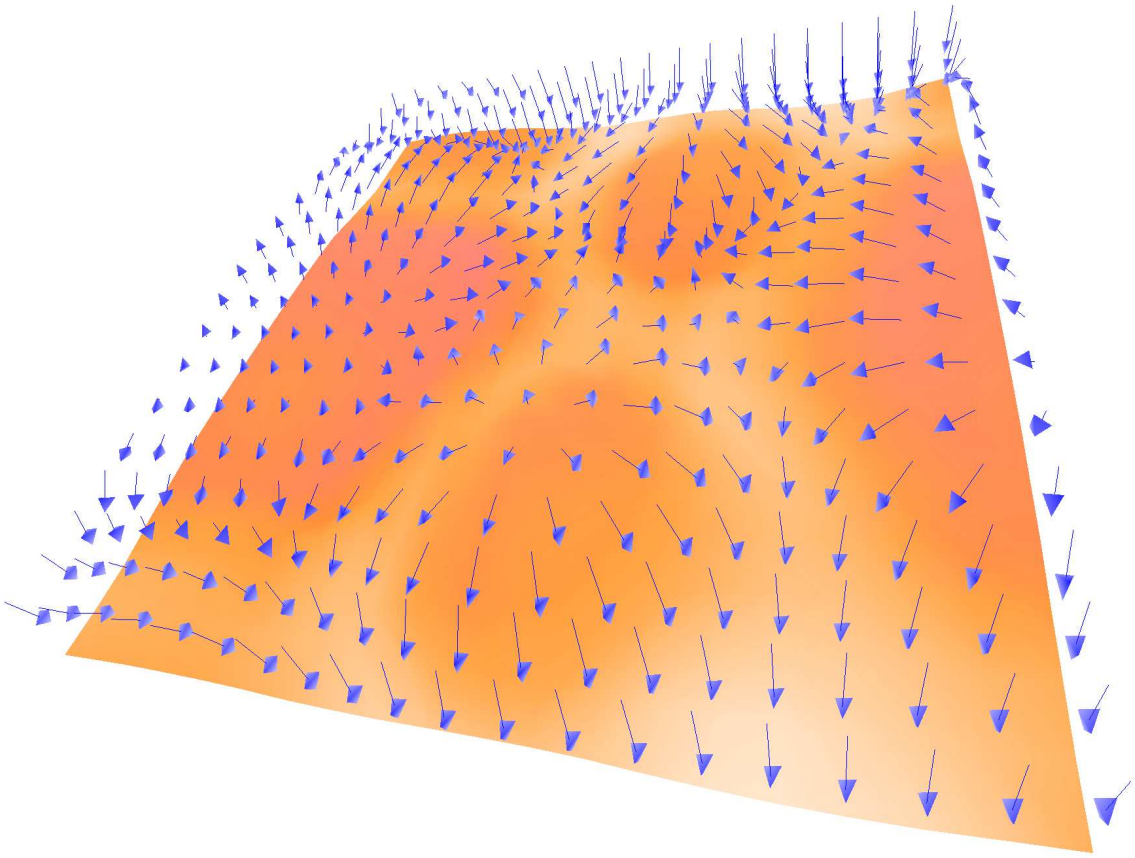

Figure 6.6: Similar to figure 6.5 for the 6700 K effective temperature simulation except this figure is during radial expansion.

the figures for the 6300 K effective temperature model to the figures for the 6700 K effective temperature model, it is clear that the change in convective strength from compression to expansion is smaller. It is interesting to note that the convective patterns show some similarity to the solar granulation pattern, in that they have large slow moving hot up flows, surrounded by fast narrow cool down flows.

We attempted to compare the convective luminosities that one obtains from multiplying the convective flux calculated using equation 5.1 by the cell areas and summing over the radial shell for the 2D and 3D cases and found large discrepancies between the two. The reason for this becomes apparent if one considers a typical 2D flow pattern, shown in figure 6.1 and compares this to a 3D flow pattern, for example figure 6.3. The largest contributers to the convective luminosity tend to be focused in relatively high speed down flows of cool material, which can be seen in both the 2D and 3D figures. If one takes a simple area weighted average of the convective fluxes in the horizontal zones in the 2D simulation and uses that to calculate the total convective luminosity of a 3D spherical shell of a star with area $4\pi r^2$, then the 2D flow pattern shown in figure 6.1 stretches into the 3^{rd} direction to obtain an area. This results in a long down flow "trench" in the unsimulated ϕ-direction. Comparing this to the 3D simulation produces a great overestimate of the convective luminosity because the trench takes up a fairly large fraction of the area. In the 3D case one can correctly take into account the 3D nature of the flow. The down flow is localized not only in the θ-direction as is the case in the 2D calculations, but also localized in the

ϕ-direction. Thus the area weighted average in the 2D case greatly overestimates the convective luminosity, while the 3D case predicts a much lower convective luminosity. When comparing 2D and 3D convective flows one really should compare the convective flux rather than the convective luminosity. An alternative would be to assume a similar distribution of convective fluxes in the ϕ-direction as in the θ-direction for the 2D simulations, but constructing a 3D distribution of convective fluxes from a 2D simulation is not straightforward. Comparing the peak convective flux over all zones in 2D and 3D models is a better indicator of how convection behaves in 2D versus 3D.

6.2 Comparison of 2D and 3D Convective Strength and Time Dependence

A more quantitative way to compare 2D and 3D convective behavior is to compare the maximum convective flux. Here we wish to investigate the differences in time dependent "strength" of convection in 2D and 3D throughout the pulsation phase. The top panel of Figure 6.7 shows the maximum convective flux throughout the entire model as a function of pulsation phase. The solid blue curve shows the results for the 3D simulation, while the dashed red curve shows the results for the 2D simulation. Both 2D and 3D curves are at a time in the calculation when the 2D and 3D have the same pulsation amplitude. From examining figure 6.7 one can see that the

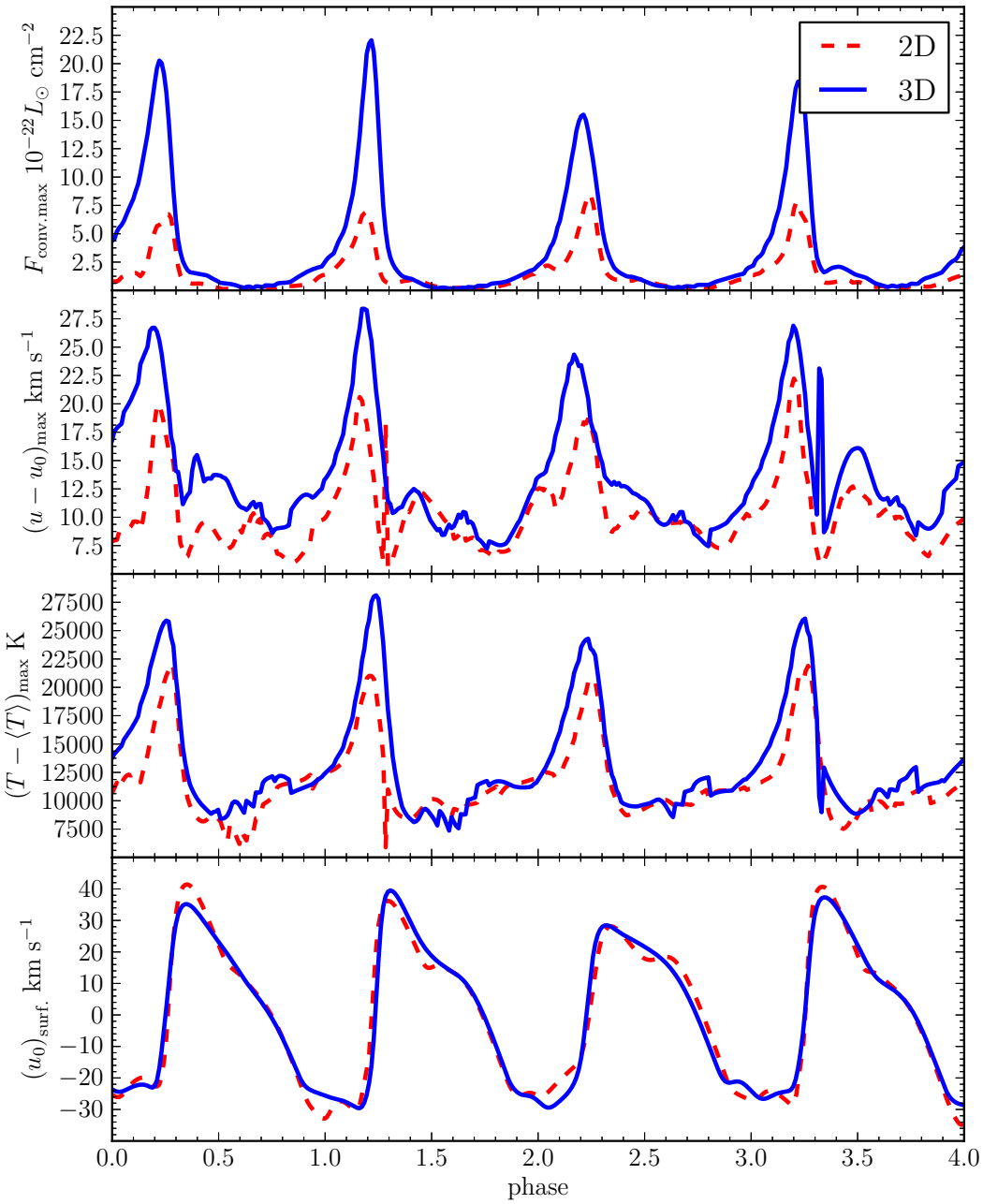

Figure 6.7: From top to bottom panel are the maximum convective flux, the maximum radial convective velocity, maximum temperature departure from the horizontal average temperature, and the surface grid velocity as functions of phase over four periods. The solid blue curve is for the 3D simulation, while the red dashed curve is for the 2D 6300 K effective temperature simulation.

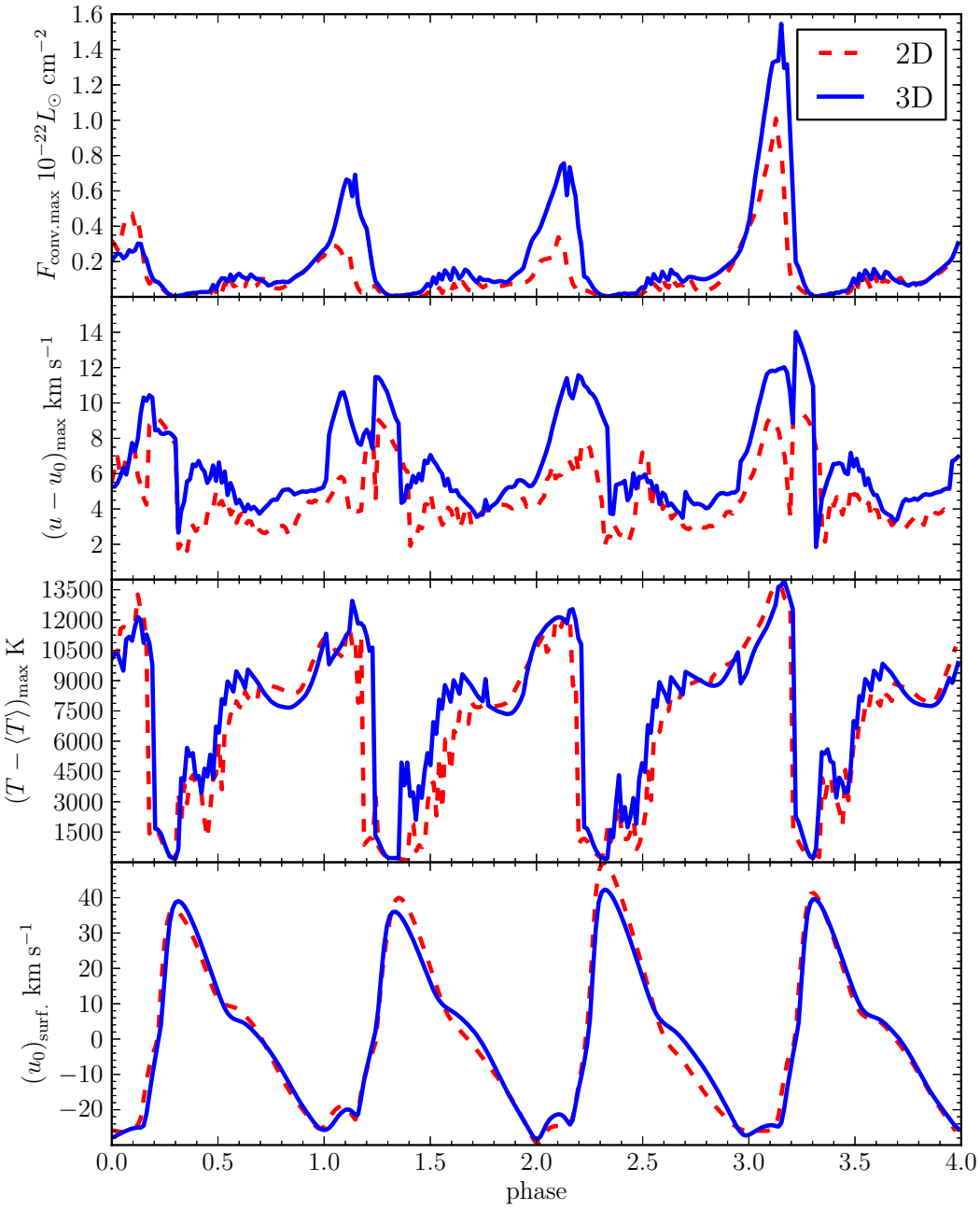

Figure 6.8: Similar to figure 6.7 except for the 6700 K effective temperature simulation.

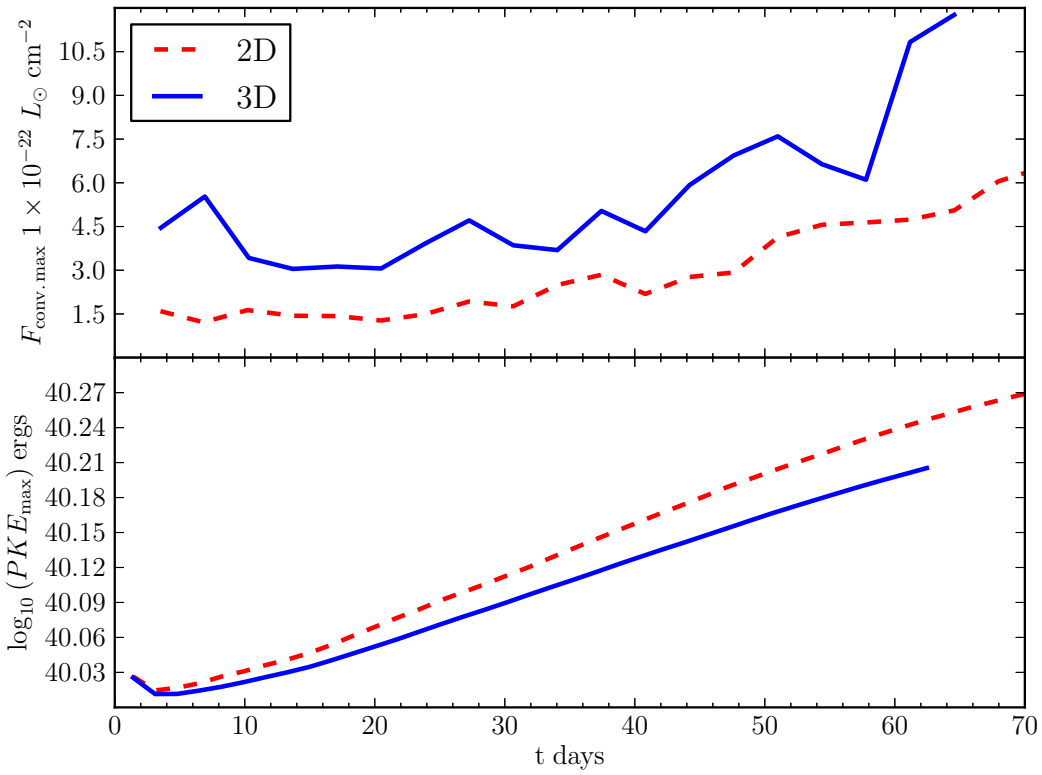

Figure 6.9: Top panel shows the six period average of the peak convective flux for 6500 K model. The bottom panel shows the growth of the log of the peak kinetic energy averaged over 3 periods of the same model.

maximum convective flux is larger at the peaks in the 3D convective simulation in comparison with those of the 2D convective simulation. The same time dependence of the maximum convective flux is seen in both the 2D and 3D models. The larger maximum convective flux is a result of larger radial convective velocities, and larger horizontal temperature variations shown in the second and third panels from the top respectively. The bottom panel of figure 6.7 shows the surface radial grid velocity in the reference frame of the star, so that negative velocities are toward the center of the star, and positive velocities are away from the center of the star. The 2D and 3D

surface radial velocities match quite well.

Figure 6.8 is the same as figure 6.7 except for the 6700 K effective temperature model. When comparing figures 6.7 and 6.8 the most obvious difference is that the maximum convective flux is substantially lower in the hotter simulations both in 2D and 3D as a result of lower convective velocities and horizontal temperature variations. Again the 2D and 3D surface radial grid velocities match quite well.

Figure 6.9 shows how the six period average of peak convective flux per period, as defined for figure 5.3, varies with pulsation amplitude. The peak convective flux averaged over the six periods clearly increases as the peak kinetic energy of the radial pulsation increases. The 3D simulation has a larger peak maximum convective flux for a given peak kinetic energy than for the 2D simulation.

Figure 6.9 indicates that the 3D pulsational growth rate is less than the 2D growth rate. We have calculated the growth rates for the 2D and 3D simulations and present the comparisons in table 6.1. The 2D and 3D growth rates are much closer than the 1D and 2D growth rates emphasizing that convection in either its 2D or 3D framework helps to slow the pulsational growth. The difference between 2D and 3D is rather small, with the 3D growth rates lower than the 2D growth rates by 0.09% for cool effective temperature models, and by 0.07% for hotter effective temperature models. This suggests that the relative behavior of convection in 2D and 3D, in terms of its interaction with pulsation, does not vary much across the fundamental mode region of the instability strip.

$T_{\rm eff}$ K	$\eta_{\rm 2D}$	$\eta_{\rm 3D}$	$(\eta_{\rm 2D} - \eta_{\rm 3D})$
6200	1.27	1.18	0.09
6300	1.15	1.06	0.09
6400	0.98	0.90	0.08
6500	0.74	0.67	0.07
6700	0.32	0.25	0.07

Table 6.1: Peak kinetic energy growth rates in % increase per period for 2D, $\eta_{\rm 2D}$, and 3D convective models, $\eta_{\rm 3D}$, and the their difference.

Although the 3D calculations have not reached full amplitude, we have performed a preliminary comparison of 2D and 3D light curves for the 6300 K model shown in figure 6.10. The 6300 K 3D simulation is the closest to full amplitude of all the 3D models. To make the comparison more consistent the light curves were produced from simulation times when both the 2D and 3D models had similar pulsation amplitudes. The light curves are noisier than the full amplitude light curves as they have not had as much time to damp out higher order modes. The comparison of these two curves suggests that the 3D curve may actually fit the complex observed light curve structure near minimum light better than the 2D light curves (see figure 5.5). However, a true comparison of the 3D light curve to observations is not possible until the pulsation amplitude of the 3D simulations cease to grow. We expect most of the cooler temperature 3D simulations to reach full amplitude in the next few months, while the higher temperature simulations may take longer.

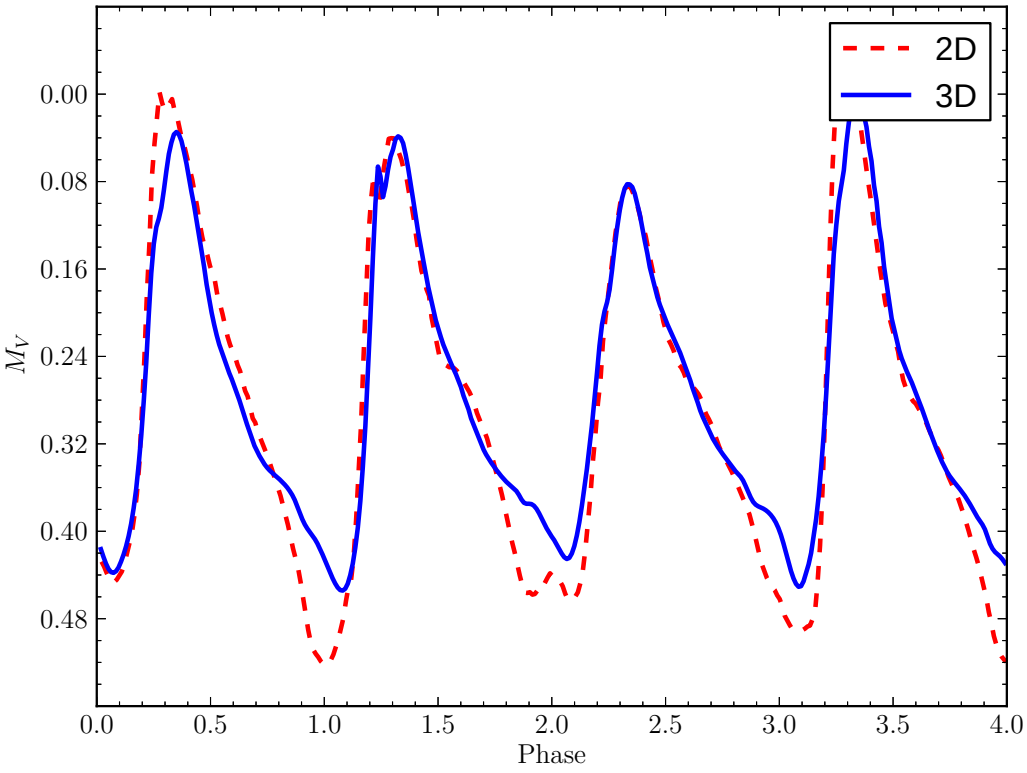

Figure 6.10: Comparison of 3D (red dashed curve) and 2D (blue solid curve) absolute visual light curves for the 6300 K effective temperature models.

7 Conclusions

While the detailed aspects of turbulent convection may not be necessarily correct because of the horizontal extent, the resolution of the problem, and the use of a specific subgrid scale model for convective effects on scales we do not resolve, we believe these calculations represent a reasonable compromise between numerical resolution and the ability to perform the calculations for the length of time required on present day computers. The goal is not so much to present a detailed model of convection as to produce a reasonable model of the interaction of convection and large amplitude radial pulsation. A key ingredient appears to be that the pulsation phase dependence of convection carry the right amount of flux in the right place at the right phase. This phase dependence appears to be independent of the strength of convection in our simulations. The amount of flux carried can depend on the physical extent of the simulation, the parameters of the subgrid-scale turbulence model, and the structure of the initial model, while the location of convection is dictated by the steepness of the temperature gradient which depends on the equation of state and opacities.

Both the 2D and 3D simulations have the same general time dependence of convective flux, growing during contraction and terminating suddenly during early phases of expansion, similar to what was found by Deupree (1977a). However, some of the details between 2D and 3D convection are different. The maximum convective velocities tend to be larger in 3D than in 2D. Also the departures of the temperature from

the horizontal mean of the temperature in 3D tend to be similar to or larger than in the 2D simulations, with the cooler models having larger temperature departures in 3D than in 2D (see figure 6.7), and hotter models have more similar temperature departures (see figure 6.8). Note that the differences on convective flux, and also those of velocity and departures of temperature from the horizontl mean, depend on the pulsation amplitude as demonstrated in figures 5.3 and 6.9. Therefore one must be careful to compare differences in radial convective velocities, and temperature departures at the same pulsation amplitude. The combination of these two effects result in larger maximum convective flux in the 3D simulations. This larger convective flux does slightly reduce the growth rates of peak kinetic energy the 3D pulsations with respect to the 2D growth rates by about 0.07 to 0.09% per period. We are awaiting completion of the 3D simulations to full amplitude in order to examine the effects of the difference of the convective flux on the pulsation amplitude and light curve shapes. An early comparison of 6300 K effective temperature 3D and 2D calculations at nearly full amplitude suggests that light curve shapes at minimum light may be better matched by 3D simulations than 2D, but we await completion of full amplitude 3D simulations for confirmation.

A comparison of 2D full amplitude light curves to observed light curves in M 3 indicates that 2D convective simulations agree as well as 1D time dependent mixing length convective models at higher effective temperatures, while they appear to be better at lower effective temperatures near (but not at) the red edge. We note that

neither our 2D nor 3D models have produced a red edge because the convection zone penetrates sufficiently deep to change the potential energy of the stellar model, thus interfering with the growth of the peak kinetic energy as a pulsational stability discriminant.

The new 2D and 3D calculations presented here have been made possible by two key advances, first faster computers in larger clusters, and second the use of a "Lagrangian" coordinate in the radial direction made possible by introducing a radial grid velocity that maintains a constant net mass in a given radial shell while allowing natural convective flow through the inner and outer boundaries of the radial shells. We look forward to the time when computational resources become powerful enough for this kind of 3D calculation to become routine.

References

Alexander, D. R., & Ferguson, J. W. 1994, ApJ, 437, 879

Baker, N., & Kippenhahn, R. 1962, Zeitschrift fur Astrophysik, 54, 114

—. 1965, ApJ, 142, 868

Balay, S., Brown, J., Buschelman, K., Gropp, W. D., Kaushik, D., Knepley, M. G., McInnes, L. C., Smith, B. F., & Zhang, H. 2012, PETSc Web page, http://www.mcs.anl.gov/petsc

Bendt, J. E., & Davis, Jr., C. G. 1971, ApJ, 169, 333

Bessell, M. S., Castelli, F., & Plez, B. 1998, A&A, 333, 231

Bingham, E. A., Cacciari, C., Dickens, R. J., & Pecci, F. F. 1984, MNRAS, 209, 765

Bono, G., Caputo, F., Cassisi, S., Incerpi, R., & Marconi, M. 1997a, ApJ, 483, 811

Bono, G., Caputo, F., Castellani, V., & Marconi, M. 1997b, A&AS, 121, 327

Bono, G., Caputo, F., & Stellingwerf, R. F. 1995, ApJS, 99, 263

Bono, G., & Stellingwerf, R. F. 1994, ApJS, 93, 233

Bruenn, S. W., Mezzacappa, A., Hix, W. R., Blondin, J. M., Marronetti, P., Messer, O. E. B., Dirk, C. J., & Yoshida, S. 2010, ArXiv e-prints

Buchler, J. R. 2009, in American Institute of Physics Conference Series, Vol. 1170, American Institute of Physics Conference Series, ed. J. A. Guzik & P. A. Bradley, 51–58

Buchler, J. R., & Kolláth, Z. 2011, ApJ, 731, 24

Cacciari, C., Corwin, T. M., & Carney, B. W. 2005, AJ, 129, 267

Carney, B. W., Storm, J., & Jones, R. V. 1992, ApJ, 386, 663

Castor, J. I. 1971, ApJ, 166, 109

Christy, R. F. 1964, Reviews of Modern Physics, 36, 555

—. 1966a, ApJ, 144, 108

—. 1966b, ARA&A, 4, 353

Cloutman, L. D. 1991, Lawrence Livermore National Laboratory Report, UCRL-ID-107128

Corwin, T. M., & Carney, B. W. 2001, AJ, 122, 3183

Cox, A. N., Brownlee, R. R., & Eilers, D. D. 1966a, ApJ, 144, 1024

Cox, A. N., & Tabor, J. E. 1976, ApJS, 31, 271

Cox, J. P. 1955, ApJ, 122, 286

Cox, J. P., Cox, A. N., Olsen, K. H., King, D. S., & Eilers, D. D. 1966b, ApJ, 144, 1038

Cox, J. P., & Whitney, C. 1958, ApJ, 127, 561

Deardorff, J. W. 1971, Journal of Computational Physics, 7, 120

Deupree, R. G. 1977a, ApJ, 211, 509

—. 1977b, ApJ, 214, 502

—. 1977c, ApJ, 215, 232

—. 1980, ApJ, 236, 225

—. 1985, ApJ, 296, 160

—. 1990, ApJ, 357, 175

—. 1996, ApJ, 471, 377

Di Criscienzo, M., Caputo, F., Marconi, M., & Musella, I. 2006, MNRAS, 365, 1357

Dorfi, E. A., & Feuchtinger, M. U. 1991, A&A, 249, 417

Eddington, A. S. 1917, The Observatory, 40, 290

Eddington, Sir, A. S. 1941a, MNRAS, 101, 177

—. 1941b, MNRAS, 101, 182

Feroz, F., Hobson, M. P., & Bridges, M. 2009, MNRAS, 398, 1601

Feuchtinger, M., Buchler, J. R., & Kolláth, Z. 2000, ApJ, 544, 1056

Feuchtinger, M. U., & Dorfi, E. A. 1996, A&A, 306, 837

Gastine, T., & Dintrans, B. 2011, A&A, 528, A6

Gehmeyr, M. 1992a, ApJ, 399, 265

—. 1992b, ApJ, 399, 272

—. 1993, ApJ, 412, 341

Gough, D. O. 1977, ApJ, 214, 196

Gregory, P. C. 2005, Bayesian Logical Data Analysis for the Physical Sciences: A Comparative Approach with 'Mathematica' Support (Cambridge University Press)

Gruberbauer, M., Guenther, D. B., & Kallinger, T. 2012, ApJ, 749, 109

Iglesias, C. A., & Rogers, F. J. 1996, ApJ, 464, 943

Kolláth, Z., Buchler, J. R., & Feuchtinger, M. 2000, ApJ, 540, 468

Kovacs, G., & Kanbur, S. M. 1998, MNRAS, 295, 834

Kuhfuss, R. 1986, A&A, 160, 116

Lee, J.-W., & Carney, B. W. 1999, AJ, 118, 1373

Marconi, M. 2009, in American Institute of Physics Conference Series, Vol. 1170, American Institute of Physics Conference Series, ed. J. A. Guzik & P. A. Bradley, 223–234

Marconi, M., Caputo, F., Di Criscienzo, M., & Castellani, M. 2003, ApJ, 596, 299

Marconi, M., & Degl'Innocenti, S. 2007, A&A, 474, 557

Meakin, C. A., & Arnett, D. 2007, ApJ, 667, 448

Mundprecht, E. 2009, Communications in Asteroseismology, 159, 51

Muthsam, H. J., Kupka, F., Mundprecht, E., Zaussinger, F., Grimm-Strele, H., & Happenhofer, N. 2011, in IAU Symposium, Vol. 271, IAU Symposium, ed. N. H. Brummell, A. S. Brun, M. S. Miesch, & Y. Ponty, 179–186

Nordlund, Å., Stein, R. F., & Asplund, M. 2009, Living Reviews in Solar Physics, 6, 2

Olivier, E. A., & Wood, P. R. 2005, MNRAS, 362, 1396

Oosterhoff, P. T. 1939, The Observatory, 62, 104

Pickering, E. C. 1901, Harvard College Observatory Circular, 54, 1

Pritchet, C. J., & van den Bergh, S. 1987, ApJ, 316, 517

Richtmyer, R. D., & Morton, K. W. 1967, Interscience tracts in pure and applied mathematics, Vol. 4, Difference Methods for Initial Value Problems, 2nd edn., ed. L. Bers, R. Courant, & J. Stoker, J (New York: Wiley Interscience)

Rogers, F. J., Swenson, F. J., & Iglesias, C. A. 1996, ApJ, 456, 902

Sandage, A. 1982, ApJ, 252, 553

—. 1990, ApJ, 350, 603

Scannapieco, E., & Brüggen, M. 2008, ApJ, 686, 927

Sedov, L. I. 1959, Similarity and Dimensional Methods in Mechanics, ed. Sedov, L. I.

Shapley, H. 1914, ApJ, 40, 448

—. 1916, ApJ, 43, 217

Smagorinsky, J. 1963, Mon. Weather Rev., 91, 99

Smolec, R., & Moskalik, P. 2007, MNRAS, 377, 645

—. 2008, Acta Astronomica, 58, 193

Stein, R. F., & Nordlund, A. 1998, ApJ, 499, 914

Stellingwerf, R. F. 1975, ApJ, 195, 441

—. 1982a, ApJ, 262, 330

—. 1982b, ApJ, 262, 339

—. 1984a, ApJ, 277, 322

—. 1984b, ApJ, 277, 327

—. 1984c, ApJ, 284, 712

Stökl, A. 2008, A&A, 490, 1181

Storm, J. 2006, Memorie della Societa Astronomica Italiana, 77, 188

Szabó, R., Kolláth, Z., Molnár, L., Kolenberg, K., Kurtz, D. W., Bryson, S. T., Benkő, J. M., Christensen-Dalsgaard, J., Kjeldsen, H., Borucki, W. J., Koch, D., Twicken, J. D., Chadid, M., di Criscienzo, M., Jeon, Y.-B., Moskalik, P., Nemec, J. M., & Nuspl, J. 2010, MNRAS, 409, 1244

Tuggle, R. S., & Iben, I. J. 1973, ApJ, 186, 593

Unno, W. 1967, PASJ, 19, 140

von Neumann, J., & Richtmyer, R. D. 1950, Journal of Applied Physics, 21, 232

Xiong, D. 1989, A&A, 209, 126

Zhevakin, S. A. 1953, Russ. A. J., 30, 161

—. 1954a, Russ. A. J., 31, 141

—. 1954b, Russ. A. J., 31, 335